FRACTURE IN SINGLE AND BICRYSTALS OF ZINC: EXPERIMENTS AND COMPUTATIONAL MODELING

BY

DHIRAJ CATOOR

B. TECH., INDIAN INSTITUTE OF TECHNOLOGY MADRAS, 2002

A DISSERTATION SUBMITTED IN PARTIAL FULFILLMENT OF THE REQUIREMENTS FOR THE DEGREE OF DOCTOR OF PHILOSOPHY IN THE DIVISION OF ENGINEERING AT BROWN UNIVERSITY

PROVIDENCE, RHODE ISLAND

MAY 2009

This Dissertation by Dhiraj Catoor is accepted in its present form
by the Division of Engineering as satisfying the
dissertation requirement for the degree of Doctor of Philosophy.

Date _____ _____

Prof. K.S. Kumar, Advisor

Recommended to the Graduate Council

Date _____ _____

Prof. A.F. Bower, Reader

Date _____ _____

Prof. C.L. Briant, Reader

Date _____ _____

Prof. W.A. Curtin, Reader

Approved by the Graduate Council

Date _____ _____

Prof. S. Bonde, Dean of the Graduate School

This work is dedicated to my parents, Srinivasan Catoor and Sugandhavalli Catoor.

Vita

Dhiraj Catoor was born to Srinivasan Catoor and Sugandhavalli Catoor on August 13th, 1981 in Cochin in the state of Kerala in India. He moved with his parents to Kakinada in the state of Andhra Pradesh in 1985 at the age of four, where he did most of this schooling. After spending two years in Kakinada, he moved to Bangalore in 1987 and lived there for a year, following which he returned to Kakinada. After finishing high school in 1998, he was granted admission into the Indian Institute of Technology Madras in Chennai in the sate of Tamilnadu where he earned the degree of Bachelor of Technology in Metallurgical Engineering in 2002.

He then pursued graduate education under the guidance of Prof. K.S. Kumar in the Division of Engineering at Brown University in Providence, RI between 2002 and 2008 with Materials Science as the primary area of study and fulfilled the requirements for the degrees of Master of Science (Sc. M.) and Doctor of Philosophy (Ph. D.). He will soon begin employment in Simulia Corporation headquartered in Providence, RI in November, 2008 as a Training Engineer.

Acknowledgements

My advisor, Prof. K.S. Kumar, has guided me throughout this long and arduous journey through graduate school, during which I found his constant encouragement, support and inexhaustible patience most helpful. He has been a great teacher, a wonderful friend, a role model and a father figure to me all at once, and I feel extremely fortunate to have been his student. It was simultaneously a great honor, a pleasure and a rewarding and a fulfilling experience to conduct research under his guidance, and I shall remain forever indebted to him. It is with great pleasure that I extend my most sincere and heartfelt gratitude to Prof. K.S. Kumar, though I know that I can never truly repay his generosity and kindness with word or deed.

I owe a great debt of gratitude to my readers, Prof. A.F. Bower, Prof. C.L. Briant and Prof. W.A. Curtin, for their time, patience and instructive and critical comments that have contributed substantially to my thesis.

Very special thanks are due to Dr. Yujie Wei for generously providing me with a VUMAT user subroutine for use with ABAQUS. His assistance in acquainting me with its use and operation is very much appreciated.

Over the past few years at Brown University, I have had the wonderful opportunity to learn various aspects of Materials Science from distinguished faculty members in the Division of Engineering. I would like to thank Professors B. Sheldon, E. Chason, D. Paine, L.B. Freund, A. Needleman, P. Guduru, and V. Shenoy for acquainting me with countless new ideas and topics that have broadened my horizons and contributed to my growth as an engineer and a scientist.

I would like to thank Christopher Bull, Brian Corkum and Reese Webb for their timely assistance with lab equipment, and Charlie Vickers and Michael Parker for help with machining items. I owe many thanks to our secretary, Diane Felber, who was always very helpful and kind.

It was a very rewarding and a wonderful experience working alongside the post-doctoral research associates and graduate students in our research group that comprised Pallavi Alur, Ping Wang, Padam Jain, Ratnesh Gupta, Badirujjaman Syed and Seong-Woong Kim. They were always there to lend me a hand and an ear whenever I needed them; I feel deeply grateful to them all in more ways than one.

Last, but not the least, are my many friends and colleagues, who, over the last few years, have enriched my experience at Brown with their generosity, kindness, friendship and camaraderie. Their constant presence in my life as a graduate student has preserved my sanity during trying times and made my stay here quite memorable. I would like to extend my deep and heartfelt gratitude to Amanda Adams, Sumit Agarwal, Pallavi Alur, Naci Arun, Tanmay Bhandakkar, Abhinav Bhandari, Eric Buchovecky, Viswanath Chinthapenta, David Cipoletti, Leanne Edwards, Vinay Gill, Rassin Grantab, Steve Grunschel, Jean Gullickson, Ramananarayan Hariharaputran, Nitin Jadhav, Vishal Jain, Lorin Jakubek, Jessica Jalbert, Sinan Karaveli, Abhishek Kothari, Mokshay Madiman, Sunil Mandowara, Nikhil Medhekar, Prateek Nath, John Raiti, Love Sarin, Christoph Sax, Narendra Singh, Maxim Shabrov, Jae-wook Shin, Laura Smith, Srikanth Srigiriraju, Bharati Srinivasan, Dhananjay Tambe, Tatiana Vasilieva, Julie Waters, Donald Ward and Pradeep Yarlagadda.

Table of Contents

List of Tables

List of Figures

Chapter 1

Introduction

Grain boundaries are one of the most common microstructural features present in crystalline solids, be it metals, ceramics or ionic solids. Being so pervasive, they have a profound effect on the properties of materials ranging from mechanical behavior to electrical conductivity. Naturally, researchers have studied the structure and properties of grain boundaries and their influence on material properties in a variety of contexts with the objective of engineering grain boundaries to produce the most beneficial effects.

In the context of mechanical behavior, grain boundaries are known to play an important role in the strength of materials. The increase in strength with a decrease in grain size is well known through the ubiquitous Hall-Petch relation. This is made possible partly due to the discontinuities in the lattice orientation across grain boundaries that create obstacles to dislocation motion. Grain boundaries are also of great importance in failure at high temperatures where creep related processes dominate. In materials of relevance to the aerospace industry such as nickel-based superalloys, they are altogether eliminated to optimize performance. With respect to fracture, grain boundaries can sometimes serve as easy paths for cracks to propagate, as is the case in materials that fail by intergranular fracture. Thus, grain boundaries can have beneficial as well as detrimental effects on mechanical properties depending on the material and context.

Transgranular cleavage, a common mechanism of failure in certain technologically relevant alloys, can be beneficially affected by grain boundaries. Cleavage fracture in metals occurs on preferred crystallographic planes, and only a few

non-parallel variants of these are normally available in any given grain. As these planes are misoriented across any given grain boundary, a crack propagating within a single grain in a polycrystalline specimen must, upon arriving at a grain boundary, alter its path accordingly to seek out these preferred planes in the next grain. This process of crack transmission across grain boundaries will naturally increase the energy required for fracture. In the case of brittle metals, the resistance to cleavage within a single crystal is usually low; but the presence of grain boundaries can augment the overall fracture resistance. While this is widely known, the role played by the crystallographic misorientation in crack-transmission across grain boundaries has not been studied in a systematic way, partly due to the difficulty in fabricating test samples that can isolate this effect so as to permit such a study. Thus the mechanism of crack transmission across grain boundaries is not fully understood. As a consequence, little has been done so far in exploiting grain boundaries as a possible source of fracture resistance in materials that undergo transgranular fracture. Given the advances made in grain boundary engineering in optimizing other properties, we feel that an in-depth understanding of the physics of the process may lead to similar improvements in fracture resistance in certain materials through grain boundary engineering.

Recently, a few articles have appeared in the literature (discussed in detail in Chapter 2) that point towards crystallographic misorientation as a significant factor in providing resistance to crack propagation [1-4]. These researchers have either observed or claimed correlations between misorientation and enhanced fracture resistance in certain technological relevant materials.

Lamellar Ti-Al, a material that is becoming increasingly relevant to the aerospace industry, is a good example where grain boundaries or colony boundaries enhance the overall resistance to fracture [1]. Within a single grain, Ti-Al tends to fracture preferentially along the lamellar planes exhibiting a very low fracture toughness value of 2-3 MPa-√m. However, polycrystalline specimens have a fracture toughness that is considerably higher, sometimes reaching values of 25 MPa-√m. A similar fracture resistance attributable to the presence of grain boundaries has been documented in Al-Li alloys subjected to cyclic loading [3]. The observed increases in toughness in these alloys have been correlated with high degrees of misorientation across the grain boundary. However, a lack of control over the most important parameter in all these studies namely, the misorientation, makes it difficult to attribute the observed resistance simply to the presence of misorientation. But the experimental evidence makes it abundantly clear that there is much to be gained by investigating this phenomenon further with a long-term goal of engineering grain boundaries and other microstructural features to optimize the fracture properties of these alloys. For instance, the grain size and texture could, in principle, be controlled to obtain the most desirable effect in terms of fracture resistance. Thus, a clear understanding of crack propagation across grain boundaries could eventually lead to the development of materials with novel microstructures.

From the perspective of misorientation, the problem of transgranular fracture can be simplified in the following way. Consider a two-grain system of the kind depicted in Figure 1.1. Here the central vertical plane that separates the two grains is the grain boundary while the shaded planes within each grain represent the preferred fracture

planes. Figures 1a and 1b represent the two simplest cases of misorientation named "pure kink" or "pure tilt" and "pure twist" respectively. For ease of representation, the

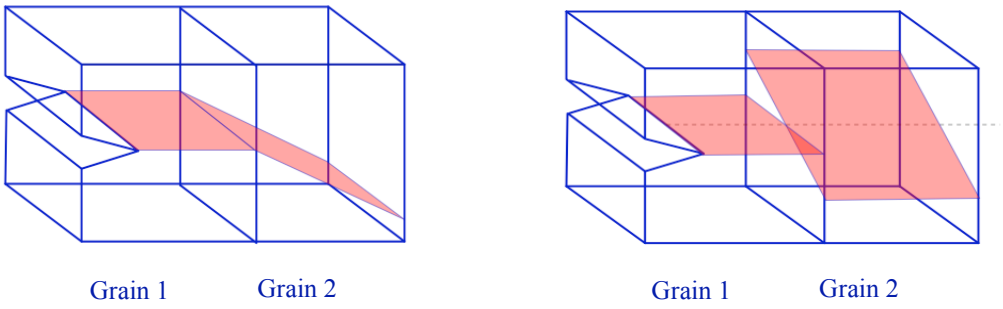

Figure 1.1. Schematic representations of misorientation. (a) Pure Kink or Tilt and (b) Pure Twist.

grain boundaries shall be referred to as kink and twist misoriented boundaries in this document and are not to be confused with low angle tilt and twist boundaries (the nomenclature here refers to the orientations of the preferred fracture planes and not the crystallographic axes). From the figures it can be discerned that in the case of kink misorientation, the fracture planes intersect in a line at the grain boundary while in the case of twist, the region of intersection is a point. Now, consider crack propagation in the case of kink misorientation: if a Mode I crack propagating through the first grain from left to right arrives at the grain boundary, the crack front, being a line, can smoothly transition onto the cleavage planes in the second grain i.e., a certain kind of continuity is maintained in crack propagation across the boundary. This is not the case, however, when one considers crack propagation across a boundary of twist misorientation. The geometry clearly forbids such a smooth transition; instead the crack would have to come to a halt at the grain boundary and the stress concentration ahead of it would cause new crack(s) to nucleate in the second grain along the preferred cleavage planes, provided

other cleavage planes have much higher cleavage strengths; and finally the cracks in the two grains would link to cause fracture across the boundary. From the above thought experiment, it becomes apparent that twist boundaries are likely to offer more resistance to crack propagation than kink boundaries.

In order to investigate the role of misorientation in a systematic manner, propagating a single crack along a preferred cleavage plane to a grain boundary of predetermined misorientation is the best way to proceed. This would require growing bicrystals of controlled misorientation, the degree of which can be varied at will. As the problem is general and not restricted to a specific metal or alloy, choosing a simple system with the necessary features is extremely important. Hence a single-phase alloy or a pure metal is an obvious choice. But the simplicity must also extend to the crystal structure. For instance, cubic systems have multiple variants of cleavage planes within a single grain that introduce an additional layer of complexity to the crack transmission process. A system with only one set of parallel cleavage planes that can be fabricated into bicrystals of predetermined orientation is ideal for an investigation of this nature. Pure zinc with a hexagonal structure fulfills all the above requirements and was therefore chosen for this study. Zinc can be grown into single crystals with a much greater ease than Ti-Al or Al-Li. In addition, there is a large body of literature describing the mechanical properties of zinc, which can eventually be used in an analytical or a numerical model.

Bicrystals of pure zinc were grown in large sizes with predetermined twist misorientation angles of 10º, 20º, 30º and 45º. *In situ* fracture tests were conducted on pre-cracked bicrystal specimens to document the interaction of sharp cleavage cracks

with grain boundaries of twist misorientation. Information pertaining to the effect of the magnitude of misorientation on the crack transmission process was also obtained.

Before one attempts to understand crack propagation across a grain boundary, it is essential to understand the micromechanisms involved in crack growth in the simplest of situations, which, in this case would be Mode I crack growth along the basal plane in single crystals. This is critical even for a model intended for bicrystals. Despite being one of the best-known examples of brittle fracture in metals, crack propagation in zinc single crystals has not been investigated in detail. Due to a tacit assumption that the mechanism is simple, experimental studies on fracture in zinc single crystals have focused primarily on the measurement of fracture toughness and energy. The current understanding of basal cleavage is based on *ex situ* fracture experiments, and the role of plastic anisotropy in crack propagation has not been given adequate consideration. Our assumptions were no different in the beginning, but our *in situ* fracture experiments have shown that cleavage in zinc single crystals is much more complex than previously thought. There is a complex interplay of dynamic and quasistatic processes that bring about interesting micromechanisms, which can sometimes lead to intragranular toughening in zinc single crystals. The crack growth response was found to depend on the crystallographic direction in which the crack is made to grow. None of these observations could be rationalized by means of linear elastic fracture mechanics.

Our *in situ* experiments on bicrystals of controlled twist misorientation have yielded a wealth of information pertaining to the microstructural aspects involved in crack transmission across a grain boundary. In particular, a high degree of fracture resistance was observed in all the bicrystal specimens, which varied with the degree of

misorientation at the boundary. The nature and the magnitude of the resistance provided by the grain boundary and its dependence on the twist angle; the competition between failure processes and plastic deformation; and the attendant effects on fracture resistance are all presented and discussed in detail.

The problem of transgranular fracture is inherently three-dimensional and only the surface can be monitored during a fracture test. Due to the complex geometry of the fracture processes encountered in crack propagation across a grain boundary, information pertaining to the stress and strain fields in the vicinity of crack tips in three dimensions is not obtainable through the documentation of load-displacement data and strain mapping on the surfaces. Three-dimensional probing through the crystals for this kind of information is currently not possible through non-destructive techniques, given the length scales involved. Thus, a full understanding of this problem necessitates a combination of experimental and theoretical techniques.

As one can expect, the three dimensional nature of the problem of transgranular cleavage makes it extremely difficult to develop an analytical model using conventional fracture mechanics. There are, however, several numerical techniques applicable in a finite element framework to simulate stationary or propagating cracks that have become available. However, none of the modeling techniques have been applied to the problem of transgranular cleavage in 3D. Of the two simple cases of misorientation discussed previously, only the kink case can be modeled in 2D. The twist misorientation, thought to be the source of greater fracture resistance, cannot be described in even the most minimal detail in 2D. Also important is the anisotropy of the system. As this feature is an integral part of the problem, any model describing transgranlular fracture must take

the anisotropic nature of fracture properties and plastic deformation into account. Hence a 3D model that includes crystal plasticity and cohesive zone formulation seems necessary, if not sufficient, in capturing the most essential details.

Again, before the more complex problem of fracture in bicrystals is modeled, numerical analyses of crack-tip stress and strain fields in single crystals must be conducted. This becomes necessary in this study for another reason: currently, there is no model that incorporates anisotropy in fracture and plastic deformation in hexagonal materials.

A 3D finite element model that incorporates crystal plasticity as a user subroutine was developed using ABAQUS, which proved highly effective in explaining several key features of basal cleavage in single crystals under quasistatic loading. Crystal plasticity accounts well for the observed differences in the response when the crack growth orientation is changed. By using this combination of *in situ* experiments and finite element modeling, a fundamentally new and comprehensive picture of basal cleavage emerges rather naturally. This model was then extended to bicrystals with a twist misorientation by including cohesive zones to allow for crack opening. As the problem is quite complex, two different strategies were employed in modeling the phenomena. Some observations qualitatively consistent with experimental results were seen.

Chapter 2
Literature Survey

It is recognized widely that in transgranular fracture, crack propagation across grain boundaries requires appropriate accommodation mechanisms to overcome the misorientation between cleavage planes. The evidence for accommodation mechanisms can be seen on the fracture surfaces of materials that undergo transgranular fracture in the form of river lines and grain boundary tearing. The presence of such mechanisms suggests an increased resistance to fracture than that can be obtained in single crystals. However, the extent to which these mechanisms contribute to fracture resistance has been significantly underestimated, possibly due to the difficulty in making precise measurements in polycrystalline metals and alloys. As a consequence, the problem of crack transmission through grain boundaries has not received enough careful attention in the past.

Nevertheless, there have been a few articles published in the literature dealing with crack propagation across grain boundaries under monotonic as well as cyclic loading conditions. In order to explain the scatter in fracture toughness values of bcc metals that undergo cleavage, especially ferritic steels, Stienstra [5] and Anderson *et al.*[6] proposed statistical models that include a grain misorientation factor to take the twist misorientation at the boundary into account. They treat cleavage as a two-fold problem that involves crack initiation and crack propagation. The former is clearly necessary, but not sufficient, and occurs when the cohesive strength of the material is exceeded locally; the latter, however, requires that the driving force required to maintain crack propagation remain high enough. Thus "crack propagation is controlled by the orientation of the

neighboring grains and the global driving force" according to Anderson [7]. The propagation problem is addressed by including a conditional probability term through an arrest toughness K_0. The crack propagates only if the applied K_I exceeds K_0, which clearly depends on grain misorientation and varies extensively in a given sample. Anderson *et al.* [6] conducted probabilistic simulations assuming {100} cleavage planes and calculating the applied K_I necessary to propagate a crack through a boundary. By varying the kink and twist angles substantially, they fit the conditional probability of propagation to an offset power law expression

$$P_{pr} = \alpha(K_I - K_0)^{\beta}$$

Where P_{pr} is the probability of failure and α and β are material constants. However, Anderson [7] concedes that incorporating the above equation into a probability analysis poses significant difficulties in applying it to experimental data. By approximating the above equation using a three-parameter Weibull distribution, Stienstra [5] arrived at reasonable fits with experimental data. Clearly, the above analysis, while being useful in estimating fracture toughness, does not include the actual micromechanisms and failure modes in operation in a non-statistical way, which is necessary from a scientific standpoint to understand crack propagation through grain boundaries.

For the case of cyclical loading, especially during short fatigue crack growth, it is well known that grain boundaries can retard crack propagation. As a consequence, several models that attribute this to incompatibilities in plastic deformation have been developed [8, 9]. The authors propose that the slip bands produced as a consequence of

crack-tip plasticity are blocked by grain boundaries due to crystallographic misorientation. They also discuss the effect of the grain boundary misorientation in constraining the overall size of the plastic zone. But the constraints on the crack path due to this misorientation are not addressed by these theories.

Experimental studies dealing with crack plane misorientation effects on crack propagation across grain boundaries are rare. A handful of articles that specifically attempt to investigate crack-growth resistance that arises as a consequence of discontinuities in the crack path due to grain boundaries have appeared recently in the literature. In the following discussion, a few such studies on Al-Li, Ti-Al, Fe-Si, Ni-Co-Cr (Ni-based superalloy) and Zn, spanning different crystal structures, are presented.

Zhai, Wilkinson and Martin [3] investigated the effect of crack plane misorientation across grain boundaries on fatigue crack growth in Al-Li alloys. They used electron back scattered diffraction to map the orientation of fracture surfaces and correlated the crack path with the local crystallographic orientation. By subjecting specimens to overload fracture that produces intergranular failure after some amount of transgranular fatigue crack growth, the authors were able to pinpoint the location of the crack front immediately prior to the onset of intergranular fracture. From this they showed that the crack front is highly heterogeneous and that it is pinned at grain boundaries of high twist misorientation. Their observations also showed that the kink angle was of little consequence in resisting fatigue crack growth. By knowing the crystallographic orientation of all the grains on the fracture surface and also the fact that cracks always propagate along slip planes, the authors argue that one can predict the crack path by finding the slip plane with the highest Schmid factor and the lowest twist

angle with respect to the previous grain. To this end, they have developed an elegant formulation for finding the relevant angles and Schmid factors at any given point on the fracture surface from orientation data obtained through EBSD. This involves the calculation of the twist and kink angles as well as the grain boundary inclination with respect to the plane of a growing crack for the entire section through which a crack grows. The resulting crystallographic crack path selection mechanism was shown to correlate well with experimental observations. The authors make a very important point regarding the numerical treatments given to the problem of crack growth involving changes in the crack plane: 2D analytical and numerical models can only explain crack tilt but are incapable of addressing the problem of crack growth across a twist boundary. While the experimental observations regarding the crack path were rationalized by relating them to the misorientation, the mechanistic aspects of crack propagation were not addressed in this study, especially the aspect of how crack growth across a twist misorientation occurs given the discontinuities in the crack planes. The fact that the crack front in these polycrystalline specimens is in contact with several grain boundaries and growing through several grains at any given time makes it difficult to attribute crack pinning only to misorientation.

Large-angle grain boundaries are known to offer resistance to cleavage crack propagation in steels and can also affect the ductile to brittle transition temperature. Argon and Qiao [2,10] and Chen and Qiao [11] have investigated crack propagation across grain boundaries using bcc Fe-3%Si bicrystals, which are known to cleave preferentially along their {100} planes. The bicrystals were oriented such that the crack grows along a <100> direction in a {100} plane oriented for Mode I fracture in the first

grain, following which it must encounter a grain boundary and propagate into a second grain across which there is a known, but not controlled, kink and twist misorientation. By welding such bicrystals to a steel testing fixture and propagating a cleavage crack to the grain boundary by means of wedge loading, the authors found significant resistance to crack growth across those boundaries with a high twist component of misorientation. The mechanism proposed by the authors is as follows. After the main crack in the first grain is arrested at the grain boundary, further loading causes several cleavage cracks on {100} planes in the second grain, which then connect by means of secondary cleavage along an orthogonal set of {100} planes to give rise to a staircase like appearance to the fracture surface. At room temperature, failure through secondary cleavage was accompanied by plastic deformation and bending, but at -20 ºC, there was hardly any observable plastic deformation. The mechanism is intuitive and novel, but the observations that led to it were made after the event by examination of the fracture surfaces, and the kink and twist were present in comparable amounts in most bicrystals. This raises doubts as to the validity of the mechanism without the aid of a systematic study where precise control of misorientation is present. The authors have discussed the relevance of the spacing between the multiple cleavage cracks in the second grain in controlling the fracture resistance. If this spacing were somehow characteristic of the misorientation or the material itself, it would play an important role in controlling the amount of resistance offered by the boundary, as the plastic work needed to connect these cracks would undoubtedly depend on this dimension. Unfortunately, the experimental and the analytical methods used here were unable to clarify what controls this characteristic dimension.

Similar observations were made by Chan and his co-workers [12] with respect to crack growth resistance in Lamellar Ti-Al, a naturally occurring composite of two intermetallic compounds, γ-TiAl and α_2-Ti_3Al. The former is an ordered fcc ($L1_0$) structure while the latter belongs to an ordered hexagonal system (DO_{19}), and the interfacial relationship between the two phases is such that the (111) planes in γ are parallel to the (0001) planes of α_2. Thus the lamellae are parallel to these crystallographic planes. A colony of such lamellae are known to fail readily by delamination along the γ/α_2 interface or by fracture through the brittle α_2 phase, and there is little resistance to fracture in both these failure modes as indicated by the very low fracture toughness values (2 MPa$\sqrt{m}$ [12]) often measured. The unique feature of this system is that there is only one set of parallel cleavage planes in a given colony, compared to three orthogonal ones in cubic systems discussed previously. Given that other modes of failure involving fracture across lamellae exhibit significantly higher toughness values and are not favored, the lack of multiple variants of cleavage planes certainly creates a greater potential for crack growth resistance due to misorientation, as compared to cubic materials.

In polycolony specimens, Chan *et al*. [12] found negligible resistance to crack propagation within a colony, but significant resistance to the same across certain colony boundaries. They showed further that the resistance was dependent on the misorientation across a given boundary. However, these conclusions drawn from surface observations raised questions about the effect of sub-surface microstructure. Wang *et al.* [1] eliminated this ambiguity by creating specimens with only one colony through the thickness by annealing their specimens to coarsen the grains. Compact tension

specimens were fabricated from the annealed specimens, which were fatigue pre-cracked and tested *in situ* in an SEM. In situ testing allowed the documentation of crack interaction with colony boundaries, and the discrete events were then related to the recorded load-extension data. The authors take into account the following crystallographic parameters in their analysis. The orientation of lamellae each colony is described by two angles with respect to the nominal crack growth direction: a kink angle α and a twist angle β; from these the kink and twist components of misorientation between the colonies is described by the differences in these angles, $\Delta\alpha$, $\Delta\beta$. The angle made by a colony boundary with the vertical plane 'θ' is also taken into account. These angles are illustrated in Figure 2.1.

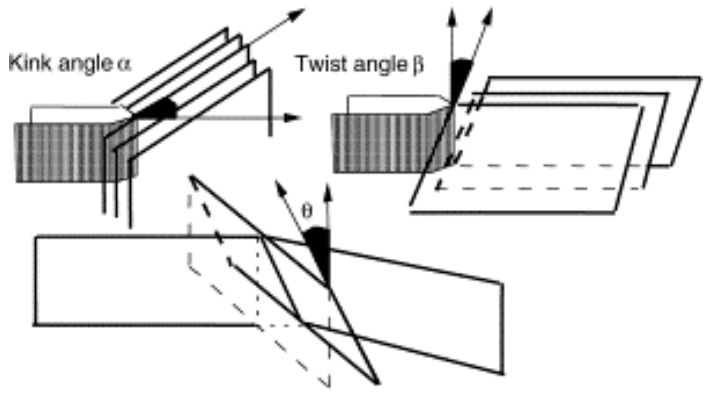

Figure 2.1. A schematic illustration of the parameters α, β and θ describing the lamellar orientation with respect to the notch and the colony boundary inclination. (Wang *et al.* [1])

In situ crack growth observations in a number of samples showed several interesting mechanisms in operation during the period when a crack attempts to grow past a boundary. Crack arrest, crack deflection, multiple microcrack nucleation in a neighboring colony, bridging ligaments between the microcracks as well as between cracks in neighboring colonies etc. were observed. In the case of a predominantly kink

misorientation, no significant resistance to crack growth was noticed, except in the case of a large θ, in which case the authors found that multiple micro-crack nucleation was observed. Resistance to crack growth is indicated by a sharp increase in the load required for crack propagation. In the absence of such an increase, one may conclude that the boundary does not offer significant resistance to crack growth. There was no noticeable damage at the colony boundary (see Figures 2.2a,c) during crack growth across a boundary with a predominantly kink misorientation, which is another indication that kink misorientation does not provide much resistance.

In cases with a high twist component (Δβ) of misorientation, significant crack growth resistance was observed, which the authors attributed to the damage processes that activate during crack growth across such boundaries. The crack comes to a brief halt at a boundary and a rise in the load is observed, following which new crack(s) nucleate in the next colony as seen in Figure 2.2d. The region at the boundary that bridges the two cracks ruptures and allows the cracks to connect as depicted in Figure 2.2e. This is indicated by the damaged appearance of the colony boundary region after the cracks connect. Cracks were sometimes found to run backwards into the first colony following arrest in some cases. One interesting observation made by the authors is that the spacing between microcracks ahead of a stalled crack at a colony boundary is at least two orders of magnitude higher than the interlamellar spacing, suggesting a characteristic spacing independent of the microstructural features and one that is perhaps controlled by stress relaxation due to microcrack nucleation.

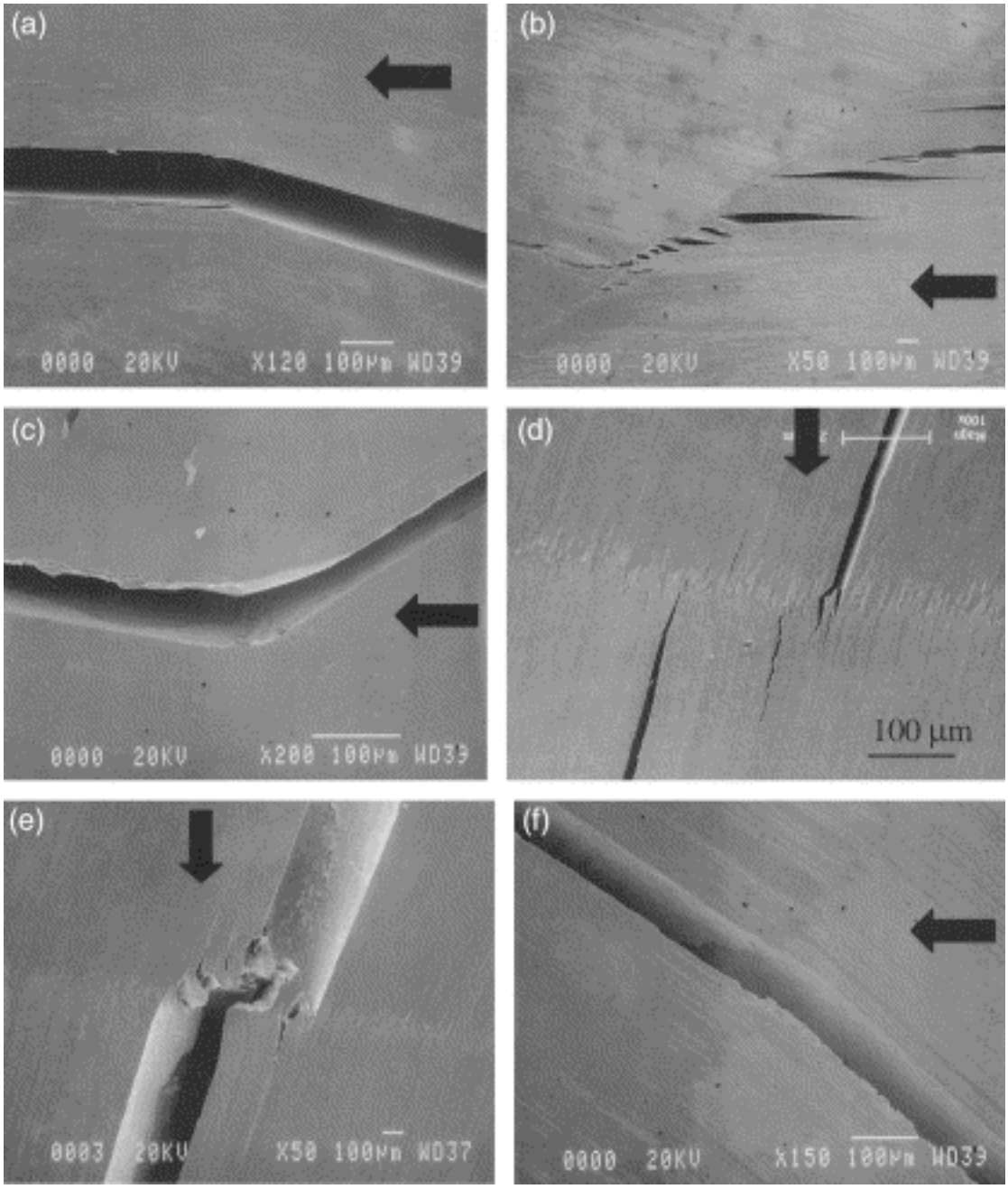

Figure 2.2. Effect of lamellar misorientation across a colony boundary and boundary inclination on damage generated in the vicinity of the boundary: (a) minimal damage when $\Delta\alpha = 14^\circ$, $\Delta\beta = 4^\circ$, $\theta = 4^\circ$, (b) multiple microcracking when $\Delta\alpha = 19^\circ$, $\Delta\beta = 44^\circ$, $\theta = 19^\circ$, (c) minimal damage when $\Delta\alpha = 43^\circ$, $\Delta\beta = 2^\circ$, $\theta = 4^\circ$, (d) and (e) bridging ligament at the boundary that subsequently fractures, accompanied by substantial plastic deformation of the ligament when $\Delta\alpha = 4^\circ$, $\Delta\beta = 52^\circ$, $\theta = 0^\circ$, and (f) minimal damage when $\Delta\alpha = 8^\circ$, $\Delta\beta = 5^\circ$, $\theta = 26^\circ$. Arrows indicate direction of crack growth. (Wang *et al*. [1])

By fabricating multiple specimens from the same block, the results were found to be reproducible. As there were no sub-surface colonies in any of the test specimens, a clear correlation between a high twist misorientation and increased fracture resistance could be established in this study. It is possible that the observed resistance is a consequence of twist misorientation, which activates several failure modes other than delamination; but the lack of precise control over the orientation and misorientation between colonies and colony boundaries, and the presence of multiple phases, interfaces and length scales in the problem make it extremely difficult to interpret the test results unambiguously as well as to model the phenomena numerically; both of these are necessary to understand the source of the observed fracture resistance. However, the above paper clearly demonstrates the importance of misorientation in the fracture process and the impediments it creates to delamination. More importantly, *in situ* observations made by these authors have provided a wealth of information pertaining to the mechanisms that activate during crack propagation across boundaries. Previously, the mechanisms discussed above were either inferred or proposed based on *ex situ* observations. Furthermore, their experimental observations point to the need for controlling the orientation of the specimens to obtain valid test results. For instance, if the first colony in which the crack is initiated has a high twist angle with respect to the notch plane, then multiple pre-cracks are generated at the notch-tip as Figure 2.3 suggests. On each of the surfaces, however, a single crack is observed at about the same location with respect to the notch-tip, leading to the misconception that the pre-crack is adequate for testing, if one does not determine or take into account the orientation of the cleavage planes in the first grain. Such situations, if not recognized, will invalidate the

fracture toughness measurements as the applied load is shared between the cracks. This clearly shows the need to control the orientation of the fracture plane in the first grain in addition to the control of misorientation across the grain boundary.

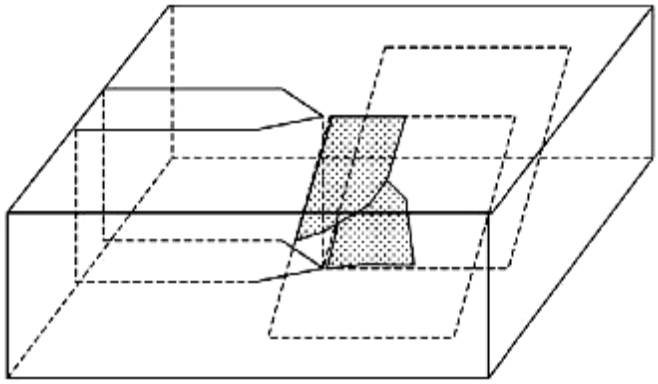

Fig. 2.3. Multiple cracking in the first grain at a notch due to twist misorientation between the notch plane and the cleavage planes. Cracks are indicated by shading.

Kumar *et al.* [13] investigated fatigue crack propagation across grain boundaries of known character in a polycrystalline Ni-based (Ni-Co-Cr) superalloy ME3 to explore the possibility of grain boundary engineering for increased fracture resistance. A combination of experimental techniques and numerical simulations incorporating crystal plasticity was used to conduct this study. By comparing fatigue crack growth behavior in the as-received and the grain boundary engineered versions of the same alloy, the authors found that grain boundary engineering produced only a marginal improvement in endurance strength, and that the crack-growth characteristics do not change due to "special" boundaries produced in greater numbers as a consequence of grain boundary engineering. However, they have observed resistance to crack propagation due to the misorientation at the boundary. Their computations suggest that as crack-tip plasticity is

significantly affected by local micrsoctructure such as the presence of grain boundaries, the crack-driving force is affected as well, which, in turn, produces perturbations in the crack-growth rates. The findings of this study add to the growing body of evidence that grain boundaries can play an important role in transgranular fracture. However, the authors did not take into account the twist angle at the boundary into consideration in their analysis and interpretation of the results, though they mention it only in passing.

A general overview of the current understanding of crack propagation across grain boundaries in various materials is presented in Kumar and Curtin [14]. The authors discuss experimental and computational methods employed in treating this problem from a broad perspective.

As is the case with experimental studies, very few numerical studies exist in the literature that deal with the problem of crack plane misorientation and its effect on crack growth resistance. Arata *et al.* [15] have developed a 2D finite element model to understand crack growth across boundaries in lamellar Ti-Al. The microstructure is simplified as a continuum reflecting the relatively plastic γ phase and a set of interfaces embedded within this continuum that represent the brittle α_2 phase. γ is modeled as an elastic-viscoplastic solid while the α_2 interfaces are modeled as cohesive zones as per the framework developed by Needleman [16] and Xu and Needleman [17]. By the use of a "cross triangle" quadrilateral mesh with cohesive zones incorporated along all the element boundaries, crack growth is allowed to occur at 0º, 45º and 90º (and other angles by changing the aspect ratio of the elements). The model is highly sophisticated, having a very fine mesh size and a high density of cohesive zones that can allow for crack

opening virtually anywhere in the specimen. Crack growth resistance is calculated and monitored evaluating the dynamic J-integral.

This model qualitatively captures many features observed experimentally in Ti-Al such as crack-arrest at colony boundaries, micro-crack nucleation and deformation of ligaments between parallel microcracks. The authors have observed an increase in the toughness due to the misalignment of lamellae across colony boundaries. Based on these calculations, they suggest that the cracking within individual colonies is less critical to the overall fracture behavior, as the ultimate failure behavior is controlled by the crack growth resistance provided by colony boundaries.

Although nucleation of multiple microcracks ahead of a macroscopic crack stalled at a colony boundary were observed in this model, the spacing between these cracks was usually of the order of the mesh size or the assumed spacing between the lamellae. In fully lamellar Ti-Al, as mentioned earlier, the spacing is of a larger length scale than the underlying microstructure [1]. Given that the toughness scales with this dimension, it is important to investigate other factors that may influence the spacing if a better understanding of the phenomenon is desired. Xuan *et al.* [18] have incorporated a heterogeneity in the prescribed fracture parameters in their model to address microstructural heterogeneities e.g. spatial variations in the interface strengths, and thus model a stochastic component of fracture.

By means of a semi-analytical linear elastic fracture mechanics study and a numerical study using cohesive zones, the authors showed that heterogeneous fracture properties could account for the observed microcrack spacing. They also concluded that

fracture occurs when the stress ahead of the crack-tip reaches a sufficiently high value over a characteristic distance.

However, both the models described above are two-dimensional and therefore take into account only the kink component of misorientation, which was seen to be of little consequence in controlling crack propagation in the experiments. The twist component at the colony boundary is clearly of greater importance and must be dealt with in a similar manner, for which, as pointed out earlier in Chapter 1, a 3D model is required. Furthermore, the material model used for this study was isotropic and thus neglects orientation dependent deformation. Given the strong anisotropy of systems that exhibit such fracture properties as observed in all the materials discussed above, in addition to the anisotropy in fracture, it is important to take the anisotropy of plastic deformation into account. This is especially necessary if there is a competition between failure modes involving plastic deformation and those that involve cleavage, which is what the experimental studies appear to suggest. Thus future studies of this kind need to incorporate crystal plasticity in a finite element framework.

From the studies discussed above, it is clear that grain boundary misorientation can play an important role in controlling the fracture resistance of certain alloys, and that the phenomenon is not restricted to a particular alloy or crystal system. They certainly hint at the potential benefits of this little understood source of fracture resistance and encourage further investigations into crack growth across grain boundaries in the larger context of developing new microstructures and alloys. Before one attempts grain boundary engineering to exploit this phenomenon, the mechanism by which it arises must be studied systematically and understood in a simple microstructure, for which zinc can

be selected as a model material as explained previously in Chapter 1. This can then be followed by similar controlled studies in technologically relevant materials. One of the problems of conducting such a systematic study in any of the above materials is that controlling the misorientation by growing bicrystals is not feasible, unlike the case of zinc, where this has been achieved by numerous workers [19-22].

Though the primary objective of our study is the understanding of crack growth resistance across grain boundaries, the study of fracture in single crystals of zinc is an important first step for the following reasons:

1. Understanding the fracture mechanisms at a microscopic level is necessary.
2. Fracture behavior in single crystals has to be compared to that in polycrystals.
3. Knowledge of fracture related parameters that can be used in a numerical model is required.

Basal cleavage in zinc single crystals has been studied extensively in a variety of contexts, perhaps due to the fact that it is one of the best-known examples of brittle fracture in metals. Early work, like that of Schmid [23], Deruyttere and Greenough [24], Gilman [20] and Stofel [25], involved the determination of the fracture stress through tensile tests. Once the importance of the differences between crack initiation and propagation were fully appreciated, Gilman [26], Maitland and Chadwick [27] and Westwood and Kamdar [28] conducted fracture tests on double-cantilever type specimens with a pre-existing macroscopic crack along the basal plane (the method is due to Gilman [26]) with the objective of measuring the surface energy of the close-packed planes. However, most of the above authors have neglected the plasticity at the crack-tip, due to the fact that the cleavage plane and the primary slip plane are identical. Burns [29]

however showed by means of Berg-Barrett X-Ray topography that basal glide occurs in substantial amounts during the cleavage process. Bilello and co-workers [30, 31] later confirmed the presence of pyramidal slip ({11-22}<11-23>) during basal cleavage at room temperature; however at 77K, pyramidal slip was insignificant [31]. In the analysis that followed, they incorporated the Irwin-Orowan correction for crack-tip plasticity in the Griffith criterion for fracture to (i) estimate the fracture energy of zinc, and (ii) understand crack-tip generated plasticity and the role of forest dislocations on crack propagation. The method used by the above authors [30, 31], referred to as the HBV method, was developed by Hull *et al.* [32] for tungsten single crystals.

The analytical treatment of this problem largely used linear elastic fracture mechanics, but a large plastic zone (of the order of 1200-1500 μm [30]) will alter the crack-tip stress fields significantly [7], rendering any estimates of fracture properties from linear elastic fracture mechanics inaccurate, even if a correction for the plastic zone is applied. In addition, high loading rates used in [30, 31] can produce uncontrolled dynamic crack growth which can invalidate quasistatic analyses. Lastly, the role of plastic anisotropy on crack-tip stress fields has not been given adequate consideration. For example, the orientation of slip and twinning systems changes substantially with respect to the crack propagation direction (say, <11-20> vs. <10-10>) and yet, there appears to be no discussion of this aspect in the published literature. Nevertheless, the choices of analytical and experimental methods used in the context of basal cleavage in zinc are quite reasonable when viewed in a historical context, as the analytical tools necessary to calculate the stress distribution and plastic strain ahead of the crack-tip in a highly anisotropic material (elastic-plastic fracture mechanics, dynamic fracture

mechanics and crystal plasticity theory) were still in development at the time of publication of most of the literature discussed above.

Rice [33] published the first analytical treatment of crack-tip stress fields in cubic single crystals using continuum crystal plasticity theory, in which he predicted the existence of angular sectors of constant stress and strain fields around a sharp crack-tip. This led to several experimental, analytical and numerical investigations into crack-tip mechanics in cubic single crystals. Cutiño and Ortiz [34] demonstrated by way of numerical analysis that local unloading to below yield levels in the near-tip regions would relieve such constant stress states while retaining discontinuities in the strain fields. Kim and Shield [35] have meticulously measured the crack-tip stress fields in *bcc* Fe-3%Si and highlighted discrepancies between analytical solutions and experimental observations and arrived at similar conclusions. Crone and Shield [36] examined the notch-tip fields in single crystals of *fcc* Cu and Cu-Be two-phase alloys, and showed that better agreement with experiments can be obtained by including anisotropic hardening in analytical and numerical treatments. These experimental studies have used a blunt notch to study the crack-tip stress fields. Kysar and Briant [37] bonded single crystals of aluminum with a thin layer of tin between them in an attempt to produce sharper cracks and showed agreement between experimental observations and Rice's solution. Despite the existence of crystal plasticity models for hexagonal crystals [38, 39], the problem of crack-tip plasticity has not been systematically addressed to the best of our knowledge; the exception is the analytical study by Gupta [40] who found no kinematically permissible solutions for basal cracks in Zn and Ti.

Given this background, it is worthwhile to reexamine crack growth on the basal planes in single crystals of zinc with the objective of understanding the micromechanism(s) of crack propagation and the effect of crystallographic orientation on it. Not only will this contribute to the existing understanding of brittle fracture in general, it is certain to provide valuable information that can contribute towards understanding crack propagation across grain boundaries in polycrystals.

The influence of grain boundaries on fracture in zinc bicrystals was investigated by Schmitz *et al*. [19, 20], where bicrystals of controlled misorientation were subjected to uniaxial tensile testing. The authors note certain differences between the deformation and fracture behavior that arise as a consequence of misorientation. However, with respect to fracture, crack initiation as well as propagation in the bicrystals was preceded by plastic deformation as the samples were subjected to uniaxial tensile testing. Under the loading conditions used in these studies, grain boundaries cause obstacles to dislocation motion, and act as crack nucleation sites.

Recently, Hughes *et al.* [4] have studied fracture in polycrystalline zinc with emphasis on misorientation and accommodation mechanisms observed at grain boundaries, and their effect on fracture resistance. Notched tensile and compression specimens of zinc were tested over a range of temperatures (77K-423K) and the fracture surfaces were characterized to estimate the relative amounts of different failure mechanisms such as basal cleavage, prism cleavage, twin boundary fracture and intergranular fracture. In their theoretical model, the authors assume that a single cleavage plane operates in each grain and the misorientation at the boundary is overcome by grain boundary failure. Though they recognize that cleavage on multiple parallel

basal planes occurs to accommodate the misorientation, their model in its current form cannot account for it. Using this model, the authors have attempted to explain and predict the relative amounts of different failure mechanisms in a given polycrystalline specimen based on knowledge of grain orientations. Since several complex mechanisms are in operation and no control over crack propagation or orientation is imposed here, the micromechanisms of crack propagation discussed by Wang *et al*. [1] and Argon and Qiao [2] were not included the model presented in [10].

In the previous studies discussed so far, several different approaches were outlined for experimentation as well as computation, which were used independently in different studies. For instance, Argon and Qiao used bicrystals of predetermined orientation but did not control the misorientation, and Wang *et al*. used in situ testing methods. Our view is that a systematic study of the kind we have undertaken here requires the use of several methods and control of important parameters in tandem, and that unambiguous conclusions cannot be drawn otherwise. Such is the case with simulations as well. The approach used here in experiments as well as computations was specially designed to bring the several methods that were used by previous researchers together to facilitate a better understanding of transgranular cleavage.

In this effort, controlled experiments of crack propagation in both single and bicrystals were conducted, and the micromechanisms were documented *in situ*. Precise control of misorientation between grains and control of orientation of the fracture plane in the first grain were implemented. Optical microscopy, scanning electron microscopy and white light interferometery were used to characterize the test specimens. Finally, finite element models that incorporate crystal plasticity were developed to calculate the

crack-tip stress and strain fields, thereby complementing the experimental observations of microstructural events and the load-displacement data. The full procedural details of experiments and computations are given in Chapters 3 and 4.

Chapter 3

Experimental Procedure

3.1 Crystal growth

Oriented single and bicrystals of zinc were grown from 99.99 % pure zinc rods obtained from Alfa Aesar, MA, using a vertical Bridgman technique in split graphite molds of rectangular cross section in a high purity argon atmosphere. Molds used for these two purposes are shown in Figures 3.1 and 3.2**;** the compartments at the lower end of the molds are used for housing oriented seed crystals, one in the case of single crystals (Figure 3.1) and two for bicrystals (Figure 3.2). The longitudinal rib in the center of the bicrystal mold assists in fixing the position of the grain boundary plane during the growth process. These molds were polished to a high degree using 800 and 1200 grit SiC paper to avoid surface nucleation and cleaned by means of acetone immediately before the growth process.

Figure 3.1. Split graphite mold for single crystal growth using the vertical Bridgman method.

Figure 3.2. Mold for growing bicrystals. Note the two compartments for housing single crystal seeds.

The reduced cross section seen in the region surrounding the seed compartment in the single crystal mold enabled an increase in the thermal gradient. At temperatures near the melting point of zinc (419.5 ºC), the thermal gradients obtained using the single crystal mold are only about 4-5º/cm. This is because the graphite mold itself is being used as a susceptor, and the greater the diameter of the mold, the larger will be the hot zone along the axis. As the temperature of the charge is maintained at 440ºC (this level of superheating is required to ensure complete melting of the hot zone), a thermal gradient of 4-5º/cm will cause the seed to melt. Reducing the mold diameter around the seed compartment reduces the suscepting capability of this region of the mold, thereby protecting the seed from melting. As the bicrystal mold was designed with a smaller cross section, the temperature gradient is steep enough to ensure that the seeds do not melt and a reduced cross section around the seed compartments was not found to be necessary.

The seed crystals with the desired orientations are cut from previously grown randomly oriented single crystals that were oriented with the aid of the Laue back reflection technique. As single crystals of zinc are extremely fragile, any mechanical means of cutting such as sawing or even electric discharge machining cause plastic deformation and cleavage on the basal planes. An example of this is shown in Figure

3.3a,b, where several basal cleavage cracks on an EDM cut surface can be seen. The plastic deformation produced during cutting can cause recrystallization at room temperature or during the growth process, both of which are detrimental to the growth of oriented single or bicrystals. Even if recrystallization did not occur at room temperature,

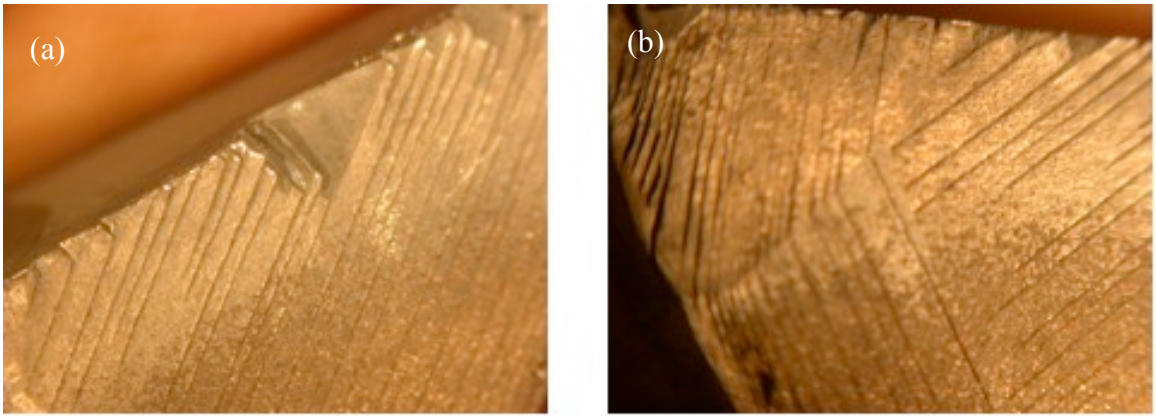

Figure 3.3. (a,b) Severe basal cracking caused by EDM cuts.

as the temperatures experienced by the seed crystals can be as high as 350 ºC during the growth process, recrystallization becomes highly likely. To avoid these difficulties, the Model 750 acid saw (shown in Figure 3.4) manufactured by South Bay Technology, which uses chemical means of cutting was used to cut the seed crystals. A stainless steel wire mounted on an eccentric system of pulleys carries nitric acid to the sample being sectioned from two reservoirs placed on either side of the specimen (see Figure 3.4b). A cut is achieved as the nitric acid slowly dissolves the material in its path. However, this process is both inaccurate and highly time intensive. A maximum cutting rate of about 0.5 mm^2/hr was achieved using 38 % nitric acid [41]. Laue back reflection images of the as-cut surfaces always showed well defined spot patterns, indicating that the cutting process does not induce strain as mechanical methods do. However, the cut surfaces

were highly non-planar, and as a consequence did not snugly fit into the seed compartments provided for in the molds. These seed crystals were then partly dissolved in a CrO_3 based solution [42] to reduce the dimensions enough allowing them to fit into the seed compartments. The same solution was also used for chemical polishing.

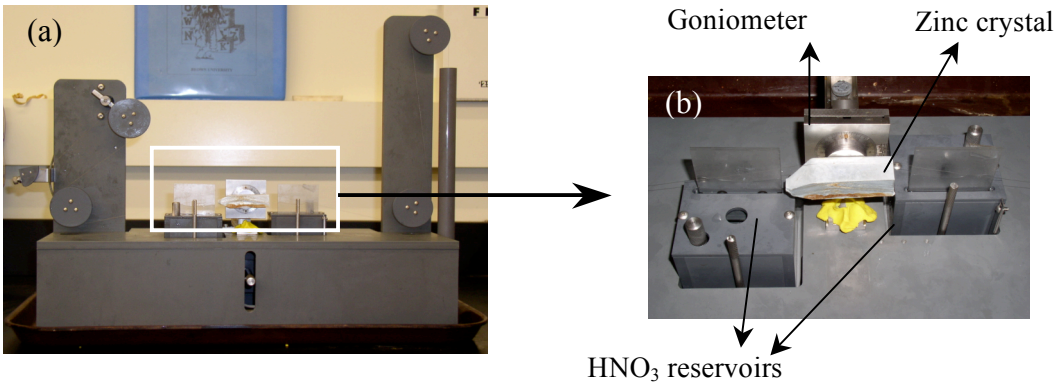

Figure 3.4. (a) The Model 750 Acid Saw manufactured by Southbay Technology. (b) Detail view showing the cutting arrangement.

The Crystalox MCG65 crystal growth furnace with an induction heating capability was used to grow single crystals of various orientations including the [0001] axis, as well as bicrystals with twist angles of 10°, 20°, 30° and 45°. One of the grains in all the bicrystals was grown along the [0001] direction to enable easy preparation of test specimens. The furnace and the assembly are shown in Figure 3.5. Zinc single crystals do not grow easily along the [0001] axis. In fact, the most favorable growth directions are all perpendicular to [0001]. Still, by ensuring proper cleanliness and mold preparation, a success rate of almost 100 % was achieved for single crystal growth. But only one in three attempts of bicrystal growth were successful. As per the findings of Cinnamon [43], who determined successful growth rates for different thermal gradients and growth axes, a growth rate of 1.3 mm/min corresponding to a thermal gradient of 5-

6°/mm present in the Crystalox furnace was employed. This was found to be effective in producing 40 mm long single crystals and bicrystals with cross section areas of 512 and 384 mm^2 respectively.

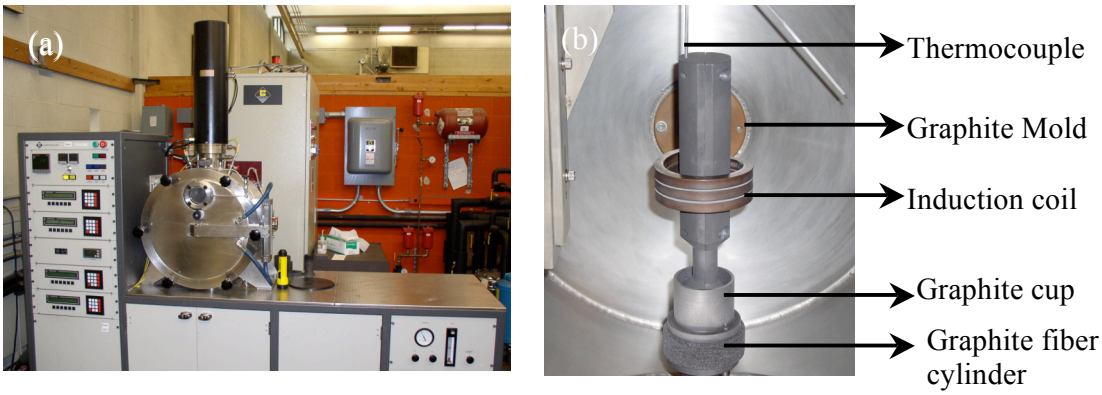

Figure 3.5. (a) The Crystalox MCGS5 crystal growth furnace. (b) View of the furnace chamber and the vertical Bridgman arrangement.

The crystals thus obtained were optically characterized for grain boundaries after etching them with a 50 % HCl solution. Due to the polished interior of the graphite mold, the surfaces of the crystals were suitable for macro-etching in the as-grown condition, eliminating the need for grinding which would introduce surface deformation. At least, two of the surfaces were checked for crystallographic orientation as an additional measure to ensure that there were no hidden boundaries that may otherwise be invisible. In some instances, there were extraneous grains near corners which were cut off or discarded during sectioning.

3.2 Sample geometry and orientation

To conserve material and to maximize the distance available for crack propagation, the double cantilever type geometry (nominally 8 mm x 8 mm x 20 mm –

see Figure 3.6) was chosen for both single and bicrystals. The nominal crack length was 7-8 mm in all cases.

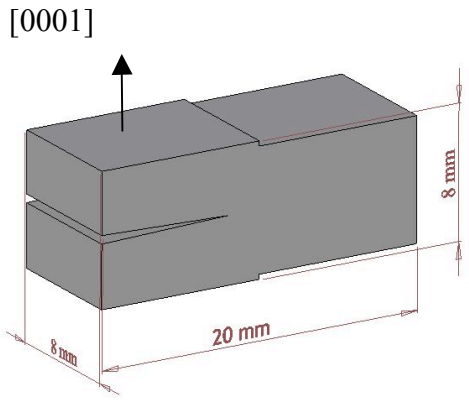

Figure 3.6. Schematic representation of the double cantilever sample geometry used for fracture testing.

The single crystals were oriented for Mode I fracture along the basal plane; i.e., the loading axis is along the [0001] direction as shown in Figure 3.6. In order to investigate the orientation dependence of crack growth response in single crystals, two crack growth directions were selected that will be referred to as orientation 1 and 2 hereafter; in orientation 1, the crack growth direction is of the <11-20> type whereas in orientation 2, it is <10-10>, both of which are displayed in Figure 3.7 as a schematic of the plan view of the fracture plane. In both cases, there is a mirror symmetry about the crack growth direction as well as the crack front. These two crack growth directions are 30º apart from one another. Given the six-fold symmetry about the [0001] direction, this is the maximum separation between any two non-equivalent crystallographic directions within the basal plane and therefore any random direction within the basal plane lies between these two extremes.

The orientation of the bicrystal test specimens is explained by the schematic in Figure 3.8, where the basal planes are indicated by the shading in red. The first grain is oriented for pure Mode I fracture along the basal plane as in the case of single crystals, and the basal plane is at a twist angle θ in the second grain with respect to the first grain. This allows us to grow a basal crack to the grain boundary in Mode I and observe its interaction with the boundary and the process of crack transmission into the second grain. Before single crystals were fracture tested in this investigation, there was no indication in the literature that the crack propagation direction on the basal plane would have an effect on the crack growth response. Hence, for bicrystals, only the crack plane, and not the crack growth direction was controlled in both the grains. However, the crystallographic orientation of all the bicrystals was characterized after growing them with the aid of the Laue back reflection technique, and is reported in table 3.1. The coordinate system adopted throughout this document is as follows: the crack propagation direction, the crack front and the loading direction are respectively along the X, Y and Z directions.

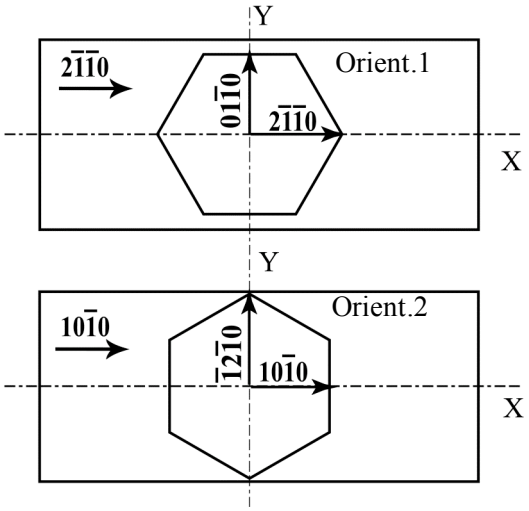

Figure 3.7. Plan view of the fracture plane in relation to the crack growth direction for orientations 1 and 2 used for fracture testing in single crystals.

3.3 Preparation of test samples

Using the acid saw, both single crystals and bicrystals were sectioned along the cross section, i.e., perpendicular to the [0001] direction, into ~ 8 mm tall sections. The top and bottom surfaces are therefore nominally parallel to the basal plane in the first grain for the bicrystals and in the entire sample for the single crystals. The length is then reduced to ~20 mm by means of the acid saw such that the grain boundary in the bicrystals is roughly midway and perpendicular to the crack plane. The top and bottom surfaces of these test specimens were made parallel by gently grinding them using 320 and 600 grit SiC paper.

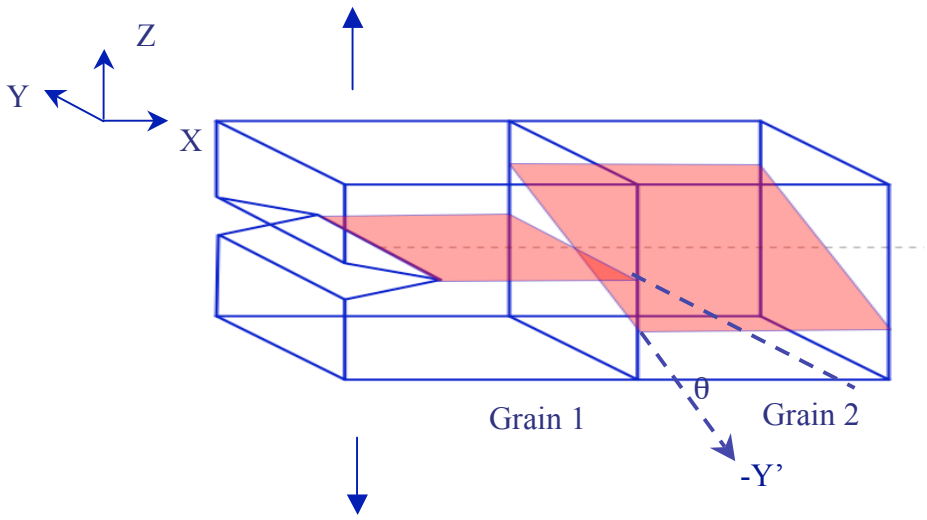

Figure 3.8. Crystallographic orientation of bicrystal test samples. 'θ' is the angle of twist misorientation.

As only the horizontal mid section of the crystal is intended for crack growth and examination, prolonged grinding on the top and the bottom surfaces of the test specimens is not expected to have adverse effects despite the tendency of zinc to sustain severe plastic deformation and recrystallization near the ground surfaces. The sides of the crystals were also obtained in the same manner, but the damage induced by grinding to

	Grain 1		Grain 2	
Twist Angle (θ)	X	Y	X	Y'
10º	[10-10]	[-12-10]	[10-10]	[-12-10]
20º	[2-1-10]	[0-110]	[10-10]	[-12-10]
30º	[2-1-10]	[0-110]	[2-1-10]	[0-110]
45º	[10-10]	[-12-10]	[2-1-10]	[0-110]

Table 3.1. Crystallographic orientation of the bicrystal specimens. Coordinate axes are shown in Figure 3.8

make them parallel was removed by means of chemical polishing. Laue back reflection X-ray photography was used as a rough indicator to ascertain the extent of damage induced during grinding,. Surfaces subjected to grinding gave rise to smeared spots with faint ring patterns indicating that grinding can cause plastic deformation and surface recrystallization at room temperature, while those that were subsequently chemically polished showed no such features demonstrating that deformation produced by grinding is confined to a depth of less than 0.25 mm and is therefore not expected to significantly affect the test results. The final errors in orientation in the test samples prepared in this manner were restricted to about 1-2º.

Though desirable, drilling holes into zinc single crystals to facilitate pin loading is impractical. This was circumvented by gluing part of the top and bottom faces of the test specimen to stainless steel grips that could themselves be pin loaded. To achieve this, a step was created on the top and bottom surfaces (see Figure 3.6) by dissolving material in the chemical polishing solution, while protecting the rest of the specimen by an acid

resistant lacquer. Initially, a screw driven Instron machine with a traveling microscope attachment was used for testing. But due to the limitations in magnification obtainable with a traveling microscope, *in situ* tests were unable to provide extensive information pertaining to the interaction of the crack-tip with grain boundaries. So, the Deben microtesting stage capable of testing samples under a metallurgical microscope as well as a scanning electron microscope was used. Due to certain differences in the construction

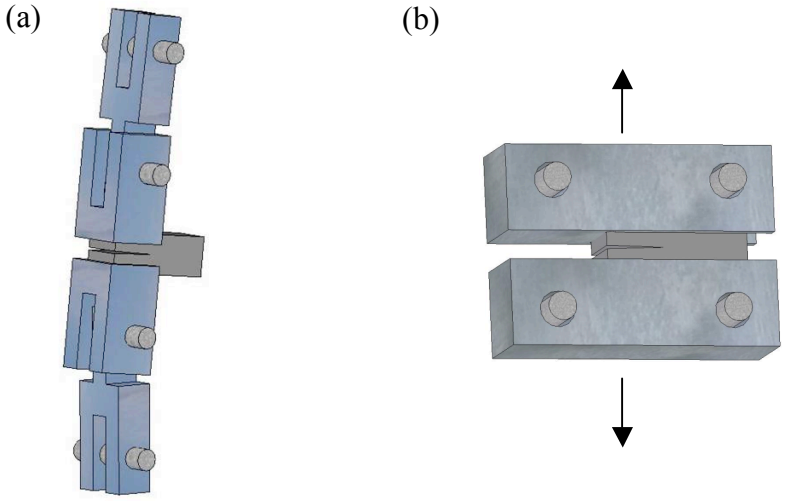

Figure 3.9. Testing configuration. (a) Schematic showing the grips used for testing in a screw-driven Instron machine. The sample (also seen in figure) is glued to the grips using superglue. The double pin joint nullifies accidental Mode II loading. (b) grips used for the Deben Microtesting stage. Sample rotation is accommodated by allowing a large clearance between the grips and the pins.

of these machines, it was not possible to use the same set of grips for both. For the Instron machine, a double joint capable of rotation about one axis to nullify Mode II components in loading was used. This is shown in Figure 3.9a, alongside the grips used for the microtesting stage (seen in Figure 3.9b), where the grips glued to the specimen were pin loaded directly. As the length available for grips and other loading fixtures in

the microtesting machine was much smaller, rotation was accommodated by increasing the clearance between the pins and the holes in the grips. For reasons that will be made clear in Chapter 6, the length of these steps was close to 8-9 mm for bicrystals.

3.4 Pre-cracking

Electric sparks have been known to induce small cracks in single crystals of brittle materials. Hull [32] conducted fracture experiments on tungsten single crystals with cracks produced by electric sparks. A similar technique was used by [28, 30, 31] to produce small cleavage cracks in Zn for fracture testing. A variation of this approach was adopted in this study to produce through-thickness pre-cracks for crack growth experiments. Using an EDM in a low power setting, a notch of length 7 mm is cut along the basal plane and this generates a sharp pre-crack along a basal plane(s) as shown in Figure 3.10. It is worth noting however, that the EDM parameters such as power and cutting speed need to be optimized to preclude large multiple pre-cracks. The other markings on the surface in Figure 3.10 are twins generated during the cutting process. The total crack length thus obtained was around 7 mm, of which the pre-crack can vary between 10 and 100 microns. In some cases, the pre-cracks obtained in this manner were through thickness at least macroscopically. However, on many occasions, multiple cracks were seen at the end of the notch. The only way of eliminating these cracks is by increasing the length of the notch further by cutting through this region. Two or more such attempts at cutting the notch may become necessary to produce a single crack. In cases where this was not achieved, two cracks were present either on one side of the

specimen or both. Crack propagation under these circumstances will be discussed in detail in Chapter 5.

3.5 Testing

Basal cleavage in zinc occurs quite readily as evident by the low fracture toughness values (< 1 MPa√m). To control crack propagation, the samples are tested in a displacement control mode with a low imposed crosshead velocity of ~2 mm/hr. The velocity was chosen such that the rate of increase in K_I is kept below 0.5 MPa√m/s as per

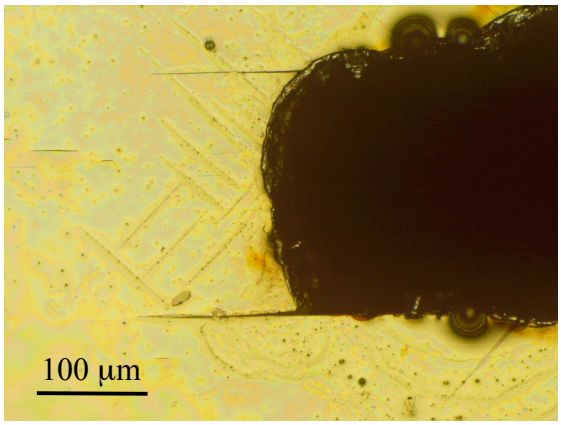

Figure 3.10. Single crystal sample with a precrack produced by cutting a notch using an EDM.

ASTM standard E-399. Crack growth was monitored and recorded using a video camera attachment to the microscope. The mechanical response of the specimens was recorded in the form of load vs. crosshead displacement data.

3.6 *In situ* observation techniques

A traveling microscope, a metallurgical microscope as well as a scanning electron microscope were used on different occasions to image the crack-tip. As mentioned

earlier, the first method was not found to be extremely useful. A metallurgical microscope was favored for most of the experiments due to its ability to yield high quality images of twins and slip traces occurring on a macroscopic scale. Polarized light microscopy and Nomarski differential interference contrast (DIC) imaging are extremely useful in this case. However, the radius of the crack-tip could not be measured due to the limitations in magnification. One test was conducted in the scanning electron microscope to obtain information about the crack-tip geometry.

3.7 Characterization of fracture surfaces

Both optical and electron microscopy were used to observe fracture surfaces; but, as mentioned earlier, optical microscopy proved to be more effective in imaging the macroscopic features on these fracture surfaces. The topography of the fracture surfaces was characterized by means of the Zygo white light interferometer, which allows quick measurements of topographical features over a wide range of magnitudes. In this particular case the macroscopic nature of these features render atomic force microscopy ineffective and even potentially detrimental to the instrument.

3.8 In situ testing in the TEM

A limited number of microtensile specimens of polycrystalline Zn were deformed in situ in the TEM to investigate dislocation activity in the vicinity of the crack-tip during crack growth and to observe the interaction of cracks with grain boundaries at the mesoscopic scale.

The specimens were machined from a rod of 99.99% polycrystalline Zn obtained from Alfa Aesar, MA (same as those used as the raw material for crystal growth). Rectangular sheets of 400μm thickness were cut using an EDM, which were sandwiched between two plates of stainless steel. Using an EDM, rectangular tensile specimens of the profile shown in Figure 3.11 were machined for testing in the Model 672 single tilt heating straining stage manufactured by Gatan. A test specimen is screwed onto the testing stage by means of the holes provided at both its ends. The EDM employed here uses a jet of water to function as a dielectric as well as to flush the residue produced during cutting. The stainless steel plates prevent the sheet from any damage that this jet may cause. The EDM cut specimens were then ground to less than 100μm thickness and twin jet polished in 12.5% Nital at -25ºC.

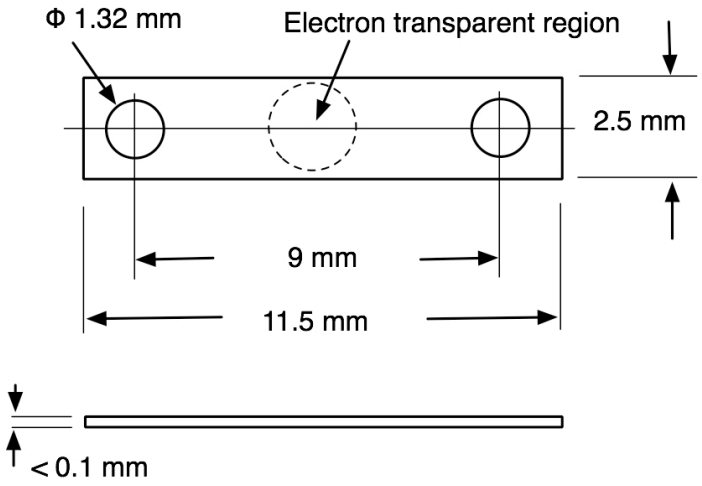

Figure 3.11. Schematic of an in situ TEM test specimen.

The specimens were loaded in pulses corresponding to 1μm elongation, or by a continuous burst of several micrometers of elongation, following which loading is stopped for documentation of the microstructural events that arise as a consequence of

this loading. The central hole created by the twin jet polishing process is also intended as a region of stress concentration from which cracks are likely to originate and grow more or less normal to the loading direction. The testing stage is not equipped with a load cell, and therefore no knowledge of the applied load can be obtained.

Chapter 4

Computational Modeling

To complement the understanding gained from the experiments, crack-tip mechanics in single crystals as well as bicrystals of zinc were investigated using the finite element method. All the computational analyses were performed using an explicit dynamics scheme with the aid of ABAQUS. Plastic anisotropy of zinc single crystals is accounted for by incorporating crystal plasticity into ABAQUS by means of a user subroutine that was developed by Anand and Kothari [44] for fcc materials, which was later extended by Staroselsky and Anand [38] for hexagonal metals. The rate independent crystal plasticity model developed by the aforementioned authors is described below.

4.1 Continuum crystal plasticity model

In a continuum crystal plasticity model, the total plastic strain is accommodated by shear strains along specific crystallographic slip systems. Each of these slip systems is activated according to Schmid's law. The following description of the model is paraphrased from that given in [38,44]

It is assumed that the total plastic strain is the sum of shear strains along all the individual slip systems which are denoted by a combination of two unit vectors, a slip plane normal m_0^i and a slip direction s_0^i, both of which are assumed to be known in the reference configuration. Then the Schmidt tensor $\mathbf{S_0}$ is given by

$$\mathbf{S}_0 = \mathbf{m}_0^i \otimes \mathbf{s}_0^i \tag{1}$$

The Schmid tensor in the current configuration at time τ is obtained from the deformation gradient according to the following equations:

$$\begin{aligned} \mathbf{m}_\tau^i &= \mathbf{m}_0^i \mathbf{F}^e(\tau)^{-T} \\ \mathbf{s}_\tau^i &= \mathbf{F}^e(\tau)\mathbf{s}_0^i \end{aligned} \tag{2}$$

4.1.1 Resolved shear stress

The stress in the structure is controlled only by the amount of elastic distortion, which is nothing but the elastic component of the deformation gradient, termed $\mathbf{F^e}$. This is calculated using the total deformation gradient $\mathbf{F}$ and its plastic component $\mathbf{F^p}$ as follows:

$$\mathbf{F}^e = \mathbf{F}.\mathbf{F}^{P\text{-}1} \tag{3}$$

The elastic strain $\mathbf{E}^e$ can then be written in terms of the elastic Cauchy-Green strain tensor

$$\mathbf{E^e} = ½ (\mathbf{C^e}\text{-I}), \text{ where } \mathbf{C^e} = [\mathbf{F^e}]^T \mathbf{F^e} \tag{4}$$

The elastic stress – strain relation is expressed as

$$\mathbf{T}^e = \mathbf{Ç}\mathbf{E}^e, \tag{5}$$

where T^e is the second Piola-Kirchoff stress or the material stress with respect to an intermediate configuration and $\mathbf{Ç}$ is the elastic stiffness tensor. Now the resolved shear stresses for each slip system τ^i can be calculated as

$$\tau^i = \mathbf{s_0^i} \cdot \left(\mathbf{C^e T^e}\right)\mathbf{m_0^i} \tag{6}$$

Note that the slip vectors appear in the reference configuration in (6). Through the tensors $\mathbf{C^e}$ and $\mathbf{T^e}$, they are in fact transformed to the current configuration by the

elastic deformation gradient $\mathbf{F^e}$. The product $\mathbf{C^eT^e}$ is being used instead of the Cauchy stress only for computational convenience.

Now, if s^i are the slip resistances, then a condition for slip on a given slip system *i* can be written as

$$\phi^i = \left|\tau^i\right| - s^i \le 0 \tag{7}$$

4.1.2 Flow rule

The plastic deformation gradient $\mathbf{F^p}$ is given by the following equation where $\mathbf{L^P}$ is the sum of the shearing rates on all the individual slip systems

$$\dot{\mathbf{F}}^{\mathbf{P}} = \mathbf{L}^{\mathbf{P}}\mathbf{F}^{\mathbf{P}}, \qquad \mathbf{L}^{\mathbf{P}} = \sum_i \dot{\gamma}\, sign(\tau^i)\mathbf{S}_{\mathbf{0}}^i \tag{8}$$

with the following conditions placed upon the shearing rates

$$\dot{\gamma}^i \ge 0, \qquad \dot{\gamma}^i \phi^i = 0 \qquad \text{if} \quad \phi^i = 0 \tag{9}$$

The above consistency conditions help determine the shearing rates γ^i on each slip system

The evolution of slip resistances are given by the following equation

$$\dot{s}^i = \sum_j h^{ij} \dot{\gamma}^j \tag{10}$$

where h^{ij} are the hardening rates for the different slip systems. The hardening rates are described as following

$$h^{ij} = [q + (1-q)\delta^{ij}]h^j \qquad \text{(no sum on } j\text{)} \tag{11}$$

where h^j*'s* are the hardening rates for individual slip systems and *q* is the latent hardening rate, set equal to 1 for coplanar slip systems and arbitrarily set at 1.4 otherwise. The individual hardening rates h^j are assumed to be of the following form.

$$h^j = h_0 \left\{ 1 - \frac{s^j}{s_s^j} \right\}^a \tag{12}$$

where s_s^j are the values at which the slip resistances saturate and h_0 is a constant, and a is the hardening exponent.

The above model is completely rate independent. The selection of slip systems is based on Taylor's principle of minimum incremental shear [45], which amounts to minimizing the internal rate of work. For a more detailed description of the model, readers are referred to Anand and Kothari [44]. Three common slip systems in zinc, the basal (0001)<11-20>, the second order pyramidal {11-22}<11-23> and the prismatic {10-10}<11-20> systems, are considered. Slip on the {10-11} planes is rarely observed and is therefore suppressed. The critical resolved shear stress values used for basal slip, pyramidal slip and prismatic slip are 0.3 MPa, 2 MPa and 4.5 MPa respectively. The first two values are consistent with those measured by Stofel [25], but somewhat lower than those used by Parisot *et al.* [39]. The ratio of critical resolved shear stress for prismatic slip to that of basal slip used here is consistent with [39, 46]. This value is of little consequence as prismatic slip is clearly unfavorable given the orientation of the crystals. Elastic constants are taken from [46]. The saturation values of slip resistances for the basal, pyramidal and the prismatic slip systems are arbitrarily set at 1 MPa, 4 MPa and 7 MPa respectively, and the h_0 and a are set at 10^3 MPa and 2 respectively.

The above rate independent scheme was employed in the form of a user subroutine in ABAQUS for modeling both single crystals and bicrystals. However, the other aspects of the methodology used are different for the single crystal case and the bicrystal case, and are described separately.

4.2 Single crystals

For the case of single crystals, the primary objective of the model was to evaluate the nature of the stress distribution and plasticity around the crack-tip region in order to explain the experimentally observed orientation dependence of fracture as well as the underlying micromechanisms. To this end, quasistatic analyses were performed for the case of a stationary crack on the basal plane with the crack growth directions corresponding to those used in the experiments dubbed orientations 1 and 2 (see Chapter 3). The crack-tip is modeled as a notch with a radius of curvature of 1 μm using ABAQUS/Explicit, consistent with *in situ* observations in the SEM.

At room temperature, zinc is known to show considerable crack-tip plasticity [30]. If the size of the plastic zone is large, then a solution obtained by using "a large strain analysis" is bound to be geometry-dependent near the crack-tip [7]. So, the geometry modeled here was chosen to mimic the actual test geometry to the best possible extent. The finite element mesh used for most of the computations is shown in Figure 4.1. The smallest element size in this particular case is approximately 0.15 μm. Reduced integration hexahedral elements with a stiffness-based hourglass control were employed. To reduce the computational time to acceptable levels, variable mass scaling was used. The algorithm employed for this purpose assigns suitable values of mass to different regions of the geometry in order to target a time increment of 0.1 ms. As an explicit dynamics scheme is being used here for a quasistatic analysis, it is imperative that the dynamic effects be restricted to a minimum, especially in the presence of mass scaling. By monitoring the energy history of the model while varying the value of the time

increment, a time increment of 0.1 ms was found to lower the kinetic energy to negligible levels when compared to the total internal energy.

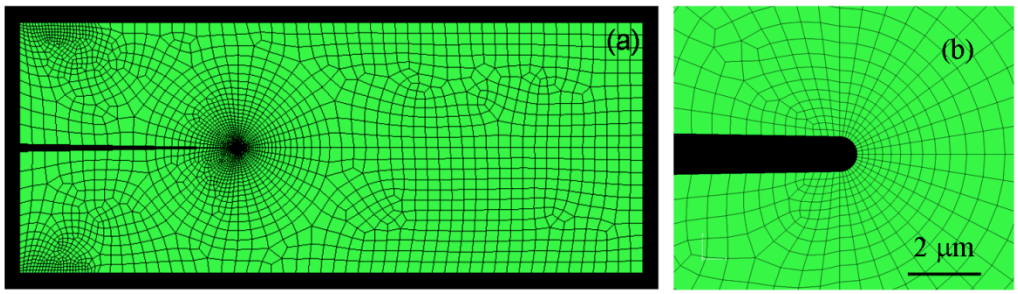

Figure 4.1. (a) Finite element mesh used for the calculations and (b) magnified view of the mesh near the crack-tip region.

Three-dimensional (3D) analyses are in general very resource intensive, and the situation is further exacerbated by the mesh refinement required at the crack-tip. For instance, with the mesh size depicted in Figure 4.1, a total of ~3 x 10^6 elements would be required to model an 8 mm thick test specimen. One may expect that the through-thickness symmetry in the case of single crystals of both orientations allows one to reduce the constitutive equations to two-dimensions; but the slip directions are not coplanar and this model is expected to be used for bicrystals where such symmetry does not exist. Therefore, the use of 3D elements is convenient. Hence a thin plate with only one element of thickness 1μm in the thickness direction was modeled here for both plane strain and plane stress conditions. The orientation of slip systems *viz. a viz*. the crack plane and crack growth direction in orientation 1 as well as orientation 2 is expected to produce plane strain deformation through most of the thickness of the specimen, with plane stress deformation on the surfaces. The results from plane strain and plane stress calculations are therefore bounding solutions for the conditions encountered in a real specimen with a finite thickness.

The boundary conditions are as follows: a length of 2.5 mm of the lower edge of the specimen is constrained in all the three directions, equivalent to gluing the specimen to a rigid grip; a similar length on the top edge is pulled at a constant velocity equal to that used in all the experiments. In the experiments, a length of nearly 4 mm was glued to the grips, but the grips were allowed to rotate slightly to eliminate any Mode-II component of loading. Since such a rotation is not included in the model, the gripping length was reduced to 2.5 mm, in an attempt to bring the stiffness of the structure closer to the experimental situation. Plane strain conditions are simulated by constraining displacements in the thickness direction for the entire geometry. In the absence of this last constraint, the specimen is approximately in a state of plane stress.

4.3 Bicrystals

The problem of bicrystals is completely different from that encountered in the single crystals and was therefore approached from a different standpoint. It is important to reiterate here that unlike the case of single crystals, the bicrystals cannot be modeled as thin sections with only one element along the thickness due to a lack of symmetry about the crack plane and the crack growth direction in the second grain. As an extension of the model used for single crystals, the problem of a stationary crack at a grain boundary was modeled with multiple elements along the thickness. The crack-tip was assumed to have a radius of curvature of 1 μm, and the mesh size in the vicinity of the crack-tip was comparable to that used for single crystals, about $1/10^{th}$ the crack-tip radius. Due to the constraints imposed on the mesh by the geometry, the crack-tip had to be located 1 μm away from the grain boundary in the first grain. This was necessary to obtain a mesh fine

enough to accurately capture the near-tip stress fields as will be shown in Chapter 5. However, two models with the crack-tip located at the boundary itself were attempted; they were different from each other only in the crack-tip radius: the radii were 1 μm and 4 μm respectively for the first and the second models. Simulations conducted on these models ran into difficulties due to the geometry, and were therefore abandoned.

This extent of mesh refinement also poses significant difficulties in modeling an 8 mm thick specimen used in experiments due to prohibitive computational costs. Therefore, the total thickness of the model for bicrystals was only 0.3 mm to keep the computational times at reasonable levels. The mesh used in our calculations is shown in Figure 4.2.

A cylindrical region of radius 0.2 mm around the crack tip was meshed with hexahedral elements and the rest was meshed using tetrahedral elements. Crystal plasticity was used to model the material behavior, and no crack extension was accounted for in this model. For different twist angles, the mesh remains the same as only the crystallographic orientation has to be changed. As the mesh size is quite similar to that used in the single crystals, no investigations into mesh sensitivity were pursued.

The idea here was to evaluate the stress state in the second grain due to the main crack in the first grain at the grain boundary in the early stages of crack-grain boundary interaction, and to understand the effect of the twist angle. The two grains of the bicrystal were joined together with a tie constraint, and variable mass scaling was used to reduce computational time. Except for the tie constraint and different crystallographic orientations specified in each grain, all the other aspects remained the same as in the case of the model for single crystals.

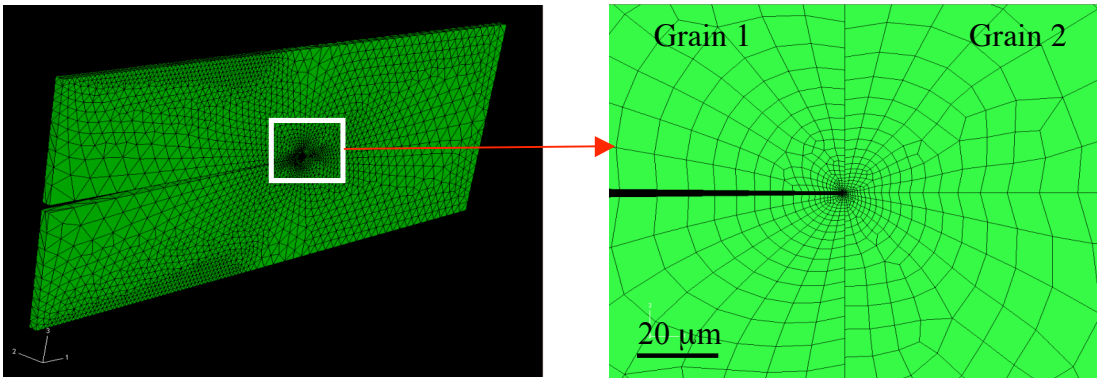

Figure 4.2. (a) Finite element mesh used to model a stationary crack at the grain boundary in bicrystals. (b) magnified view of the mesh near the crack-tip.

Clearly, such a model cannot explain the multitude of microstructural events observed such as multiple cracking in the second grain, deformation of crack ligaments and bridges etc. Crack growth must be taken into account for any of these features to be adequately captured. One of the important questions to answer is where and when cracks nucleate in the second grain once the basal crack in the first grain encounters the grain boundary, and, if possible, determine the characteristic spacing between these cracks. Also of interest is the dependence of the above-described features on the twist angle. Therefore, 3D models with multiple elements along the thickness, with the cohesive zone formulation to allow for crack extension were employed for this purpose. The geometry of the model is approximately the same as that used in the experiments.

The cohesive zone formulation was developed in analytical form by Dugdale [47] and Barenblatt [48], and was later adapted for use in finite element analyses by various researchers such as Needleman [16, 49]. The basic idea here is to include a set of thin cohesive zones or surfaces placed judiciously in a continuum. Fracture can be viewed in the simplest of terms as a separation of two atomic planes, the traction across which is

described by an interatomic potential. In response to an increasing remote load, the traction across a cohesive zone will increase to reach a maximum, following which it will decline and vanish. The point where total lack of traction occurs can be viewed as fracture or complete separation. Using this technique in a finite element framework requires some knowledge of the fracture path in advance, for only those regions of the model where cohesive zones are available are capable of separation. If such knowledge is possible to obtain, then crack growth can be simulated naturally by a finite element model with cohesive zones.

Two constitutive equations become necessary to model the behavior of the system. For the volumetric domain, rate independent crystal plasticity (already described in some detail previously) was used. The cohesive surfaces are modeled using a simple linear traction-displacement relation i.e., they are assumed to act as linear springs holding the different sections of the volumetric domain together. The linear traction-separation condition can be expressed as follows.

$$\begin{bmatrix} t_n \\ t_s \\ t_t \end{bmatrix} = \begin{bmatrix} K_n & K_{ns} & K_{nt} \\ K_{ns} & K_s & K_{st} \\ K_{nt} & K_{st} & K_t \end{bmatrix} \begin{bmatrix} \delta_n \\ \delta_s \\ \delta_t \end{bmatrix} \tag{12}$$

where the t's and δ's are tractions and displacements respectively, and the subscripts n, s and t, refer to the normal and the two shear directions respectively. The K's are the stiffness terms. For simplicity, the normal and shear tractions are assumed to be uncoupled, and so the off-diagonal terms are set to zero.

A critical opening traction criterion was used for the initiation of failure. Essentially, once the traction across the cohesive surface reaches a critical value, the load

bearing capacity of it is allowed to reduce to zero, thereby simulating the creation of free surfaces and crack extension. This necessitates a softening law, and ABAQUS allows linear and exponential laws for the softening part of the constitutive law. The exponential version proved to be more stable numerically and was used for all the calculations presented in Chapter 7. Figure 4.3 shows a schematic of a traction vs separation curve with exponential softening. An energy-based criterion was used to determine the point of complete separation i.e., when the area under the traction-separation curve exceeds the energy or work of fracture, the element is simply eliminated from the calculation. The material parameters for the cohesive zones must be selected based on actual material behavior as well as numerical considerations. From the material behavior standpoint, it must be recognized that fracture in reality is never a true separation of atomic planes, especially in the case of metals, regardless of how brittle they are. Plasticity at the crack-tip ensures that fracture occurs on multiple planes simultaneously. At a continuum level, if the material is brittle, these complexities can be ingnored if they occur at a length scale significantly smaller than that being modeled. Due to numerical considerations that will become clear shortly, the cohesive zones in a finite element model of a macroscopic specimen are not of atomic dimensions. Hence the material parameters such as work of fracture and stiffness of cohesive zones cannot be determined from interatomic potentials. One must calibrate these parameters by comparing experiments and simulations.

The stiffness constant K_n corresponds to loading in the [0001] direction and was assigned a value of 63 GPa/mm, the elastic constant along the [0001] direction. The maximum normal traction for initiation of failure was taken to be 5 MPa. As the CRSS

for basal slip is 0.2 MPa, shear tractions beyond the prescribed saturation stress, 0.4 MPa, are not accessible; given that zinc undergoes high amount of basal slip at low shear stresses along the basal plane, Mode II and Mode III type failure is unlikely. Therefore, so long as they are of the same order of magnitude as the normal stiffness and maximum normal traction, the parameters corresponding to Mode II and Mode III failure are of little consequence. K_s and K_t were set at 158 GPa/mm (corresponding to the elastic constant in the [11-20] direction which coincides with one of the orthogonal coordinate axes used for the cohesive zones) and 100 GPa/mm; and both the maximum tractions for failure initiation were assigned a value of 7.5 MPa/mm. The work of fracture was set at 0.001 N/mm as per the values cited in literature [28].

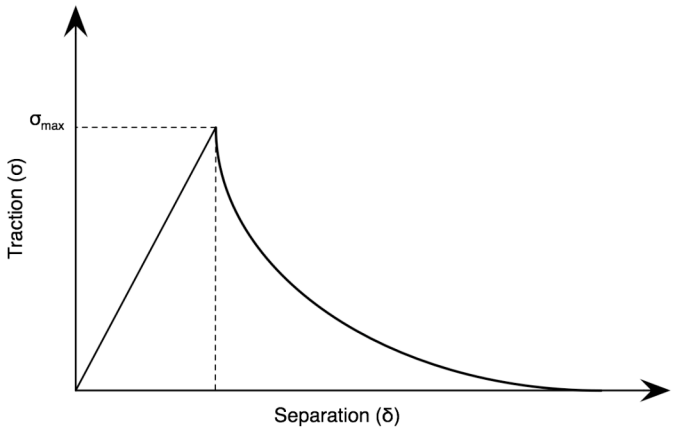

Figure 4.3. Schematic plot of constitutive relation used for cohesive zones. Area under the plot is equal to the work of separation or fracture.

3D cohesive elements with eight nodes and a finite thickness of 0.01 mm were employed, and the thickness to the element size ratio was kept below 1/50. As the analysis uses an explicit scheme that naturally accounts for wave propagation through the

system, the time step depends on the thickness of the cohesive elements, becoming smaller as the thickness reduces. Though desirable for accuracy, making the cohesive elements smaller than this would substantially increase the computational time and was therefore not attempted.

For the first grain, only one set of cohesive elements was placed along the crack plane; and in the second grain, multiple parallel and equidistant cohesive surfaces oriented according to the twist angle were included. The second grain therefore presents a difficulty in terms of meshing, given the constraints arising out of the need for slant cohesive surfaces. Only one set of 3D hexahedral elements were used between any two consecutive cohesive surfaces, which begin and end on the outer surfaces. The region thus meshed forms a parallelepiped. The remainder of the second grain, a pair of triangular prism like regions, above and below the parallelepiped region, were meshed using wedge elements. Figure 4.4 shows an example of the type of mesh used in these calculations.

It is worthwhile to note here that the geometric complexities prohibit the use of the same mesh for different twist angles and that for a given twist angle and mesh size, the arduous task of constructing a unique model becomes necessary. The spacing between the cohesive surfaces and therefore the mesh size in the second grain were arbitrarily fixed and in the cases of 10º and 20º degree twist angles, and the normal distance between any two consecutive cohesive surfaces was 0.28 mm to enable comparison. The mesh in the first grain is simply a set of hexahedral elements with a cohesive surface dividing the upper and lower half. The X-axis (crack growth direction) is assumed to be a <11-20> direction in both the grains for simplicity.

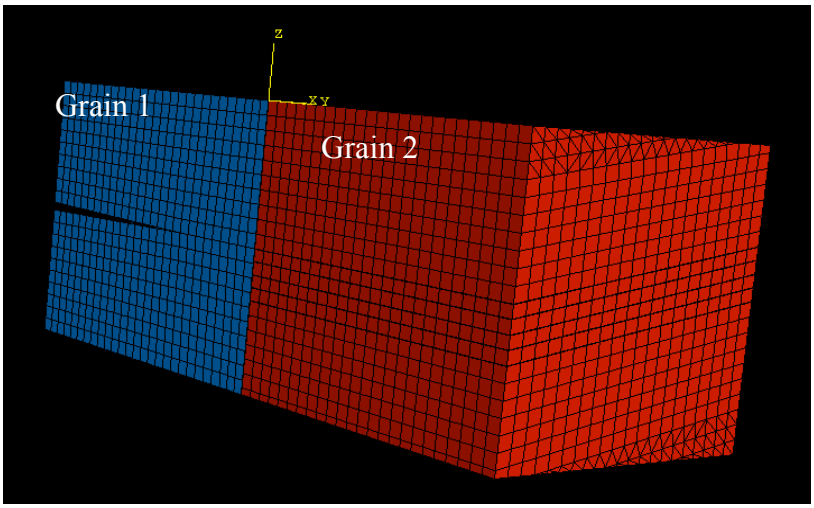

Figure 4.4. Finite element mesh used to model fracture in bicrystals. Note the mesh in grain 2 designed to allow for fracture along basal planes at a twist angle, 10º in this case.

The two grains were created as two different blocks and joined together by a tie constraint to create a discontinuity in deformation and the crack path at the grain boundary. Therefore, the grain boundary has no width and plastic or elastic deformation is not possible in it, and the tie constraint does not permit grain boundary sliding. The constraint only serves to transmit the stresses ahead of the crack-tip in the first grain into the material in the second.

The boundary conditions are similar to those applied in the case of single crystals in that a part of the bottom surface in the first grain is constrained in all three directions while the top surface is pulled at a constant velocity of 2 mm/hr in the vertical direction. The area of the surface regions to which the boundary conditions are applied is the same as that in the experiments conducted using the microtesting stage, which is 8x8 mm^2.

For reasons that will be explained later in Chapter 7, only 10º and 20º twist angle cases were modeled. The total number of degrees of freedom in each of these models is

nearly 100000. Although ABAQUS is capable of performing analyses using parallel processing, the user subroutine, written in FORTRAN 77 and FORTRAN 90, is not thread safe for MPI based parallel computation; so the analysis can be performed only on one processor. As the number of degrees of freedom is quite large, this presents a significant difficulty because of the computational times encountered in these analyses. Calculations done to reflect the total amount of remote displacement applied to the bicrystal routinely take four weeks to complete. The entire subroutine would have to be rewritten in FORTRAN 90 and tested before it can be run in parallel, and if and when this is accomplished, one may use 4 to 6 processors, beyond which the efficiency is expected to saturate. If more processors need to be used, then the entire analysis should be conducted using a program written specifically for this purpose instead of ABAQUS. Since these improvements are beyond the scope of this work, they were not attempted.

The above method clearly puts limitations on the mesh size due to the sheer number of degrees of freedom. Though multiple cracking and ligament deformation can be captured by such a model, the stress field around any of the different crack fronts is bound to be inaccurate. Nevertheless, it is a first attempt at modeling such complex phenomena in three dimensions that can provide important insights and benefit future efforts.

Chapter 5

Crack Growth along the Basal Planes in Single Crystals

5.1. Experimental observations

5.1.1 In situ crack growth observations

Observations from a total of eight specimens (designated 1-A, 1-B etc and 2-A, 2-B etc) are discussed. In all the cases, crack propagation along the basal plane was observed to be discontinuous, alternating between periods of rapid growth and arrest, the latter being accompanied by blunting. The typical length of these rapid-crack-growth-segments for specimens with orientation 1 (i.e. crack propagation in the <11-20> direction), were a few tens of micrometers; whereas, they were significantly larger at a few hundreds of micrometers for orientation 2 (i.e. crack propagation along the <10-10> direction). A sequence of still images extracted from a real time video recording is displayed in Figure 5.1 and illustrates the typical crack growth behavior within a single crystalline region. A surface aspersion (marked X) visible in all the images serves as a reference marker. In Figure 5.1a, a crack-tip can be seen at a certain distance away from X; upon loading, the crack extends forward rapidly by a distance of 150 μm and arrests as seen in Figure 5.1b. In response to further loading, the crack-tip begins to blunt as observed in Figure 5.1c, where blunting is inferred by the increase in the separation between the crack faces without crack extension. In Figure 5.1d, the crack-tip has experienced a second dynamic extension event, recreating the situation in Figure 5.1b, and this cycle repeats itself.

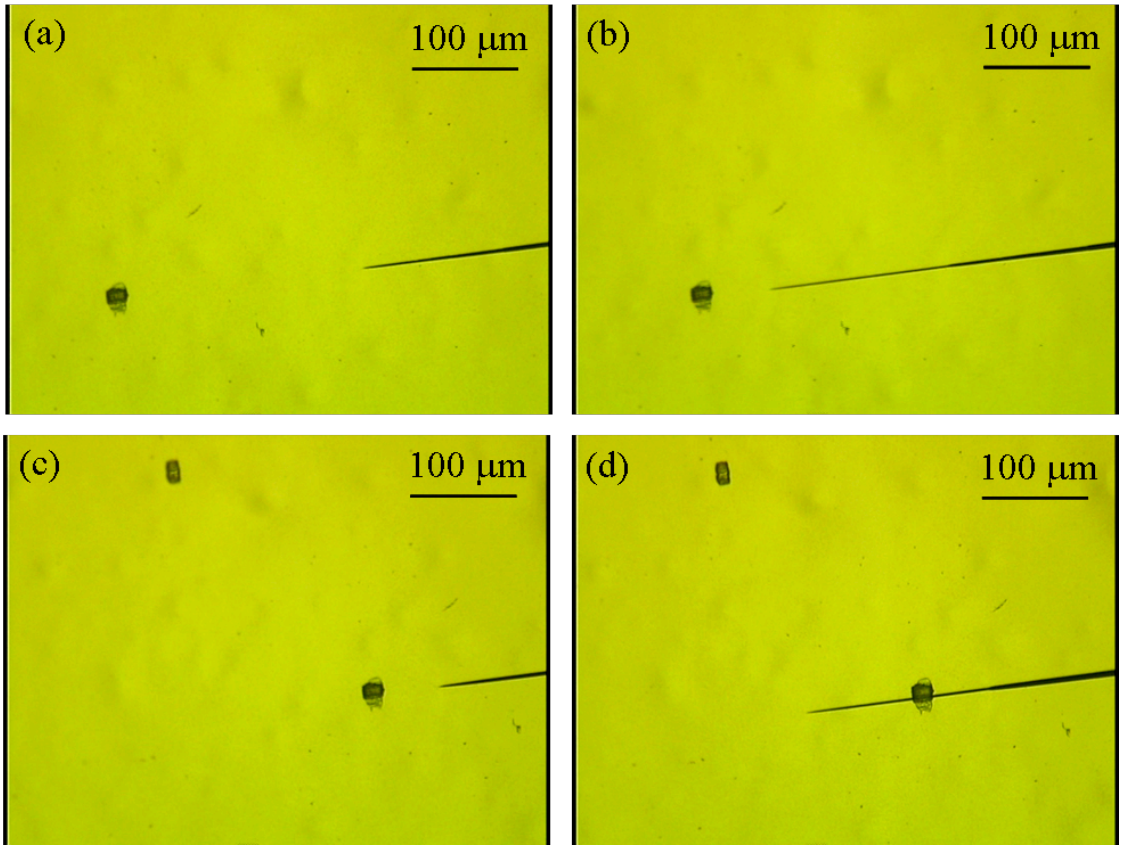

Figure 5.1. A sequence of images showing crack propagation on the basal plane: (a) micrograph of the crack-tip following a crack arrest event, (b) immediately after 150 μm of dynamic crack extension, (c) crack-tip undergoing blunting during the arrest period (note the separation between the crack faces has increased noticeably compared to (b)), and (d) after a second dynamic crack extension event.

Often, a new micro-crack nucleates a few micrometers away from the existing crack-tip on a parallel basal plane (Figure 5.2a) and propagates unstably forward and backward (Figure 5.2b; the "new" crack in Figure 5.2b propagates ~250 μm forward and by ~10 μm backward). The ligament between the two cracks experiences shear, undergoes deformation and finally ruptures either in a ductile manner (Figure 5.2c) or, at other times, by non-basal cleavage, causing the old and the new cracks to link. Crack propagation is retarded as a result of this ligament formation and the associated shielding of the crack-tip.

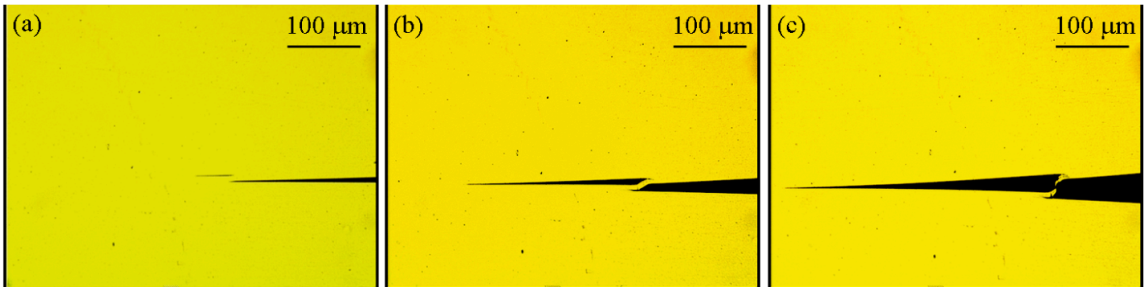

Figure 5.2. (a) Nucleation of a micro-crack on a basal plane above the existing crack plane, (b) shearing of the ligament between the old and the new cracks, and (c) ligament failure by ductile rupture.

Zinc is known to deform by twinning as well as slip. Twinning along the common {10-12}<10-11> system requires contraction along [0001] or elongation along any direction in the basal plane. This would not be possible immediately ahead of the crack-tip as Mode I crack-tip stress fields cause extension along [0001]. However, if, for some reason, the crack-tip blunts extensively thereby reducing the stress intensity, the arms of the double cantilever specimen can bend in response to the remote load, and can create favorable conditions for twinning in the crack-wake. An example from a specimen of orientation 2 (Specimen 2-C) is shown in Figure 5.3a. Two symmetric twins (marked A and A') just behind a blunt crack-tip and intersecting the free surfaces created by the crack can be seen in this figure. The twin bands far ahead of the tip, also visible in Figure 5.3a, were pre-existing, through-thickness twins and did not arise as a consequence of the crack-tip. In Figure 5.3b, a new micro-crack originating below the existing primary crack plane is seen. This crack encounters the pre-existing twin band and comes to a halt (note the presence of a small twin partway along this microcrack, presumably created by the complex stress state present between the new microcrack and the main crack).

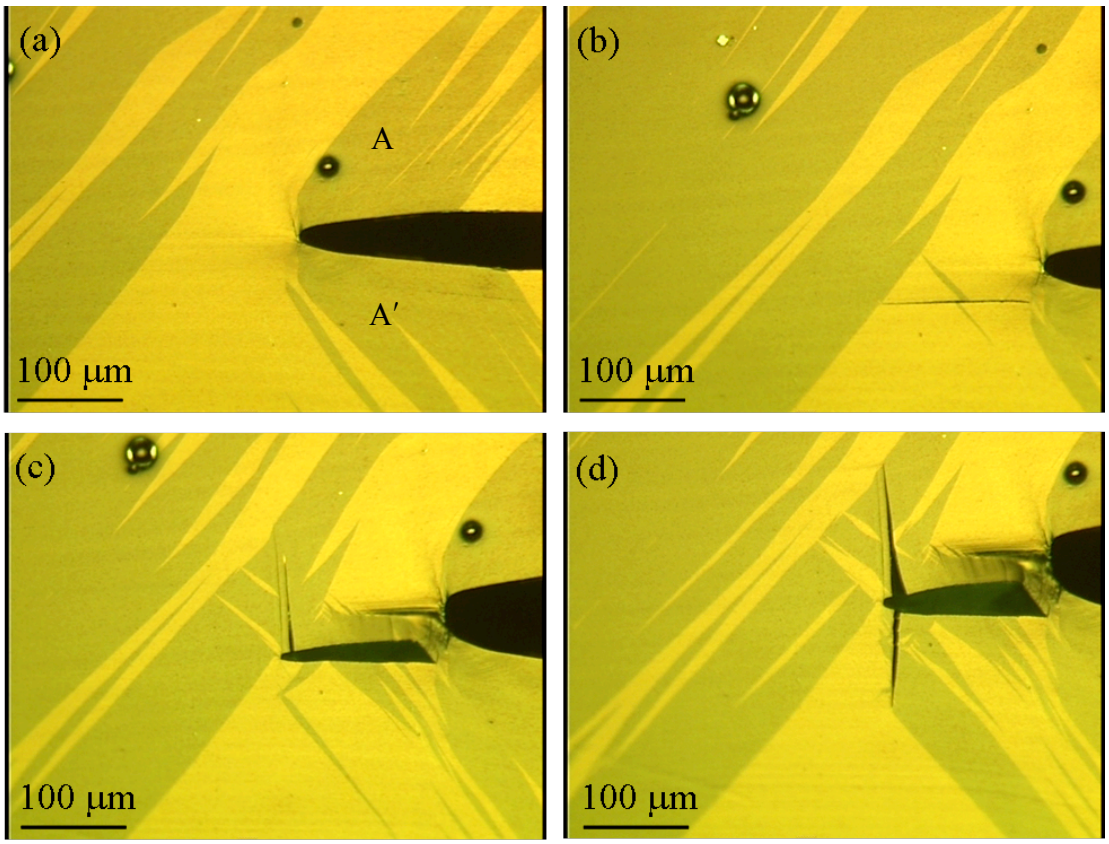

Figure 5.3. Crack-twin interaction in orientation 2: (a) twinning in the crack wake at a blunt crack-tip in orientation 2 (marked A and A'), (b) a micro-crack ~35 μm below the previous crack plane, (c) micro-crack in (b) blunted by the twin, a secondary crack forms on the basal plane within the pre-existing twin, and de-twinning in the vicinity of the micro-crack, and (d) an additional crack through a new twin resulting in a T-shaped crack-tip and further de-twinning.

Upon a significant increase in applied displacement, the micro-crack-tip observed in Figure 5.3b undergoes significant blunting and a new crack propagates into the pre-existing coarse twin almost normal to the pre-existing crack (Figure 5.3c). Further, ahead of the blunted micro-crack, and within the coarse twin, de-twinning is observed. Meanwhile, the "old" primary crack-tip experiences further blunting and finally advances forward by the re-formation of a sharp crack; the ligament in between the primary crack and the micro-crack experiences substantial deformation and twinning. The formation of

the nearly orthogonal crack in the twin can be rationalized by understanding that the basal plane within the twin is rotated by either 86° or 94° with respect to that in the parent about the crack front, which coincides with a <11-20> direction. In Figure 5.3d, additional twinning is observed, and serves as a precursor for a second crack to propagate downwards, producing a T-shaped crack-tip. Due to this unusual geometry, further loading only produced plastic deformation but no crack-extension. In passing, it is noted that de-twinning continues further in the large pre-existing twin band.

The interaction of an advancing basal crack with a pre-existing twin is quite different in orientation 1, an example of which is illustrated in Figure 5.4a-d. The basal plane within the twin in this case is rotated by the same angle, but not about the crack front. Instead, one of the <11-20> directions at a 30° angle to the crack front serves as the axis of rotation. The twin band, too, is oriented at the same angle. Thus, the entire crack front does not encounter the twin simultaneously. Only a small part of it interacts with the twin at any given time, which means that the situation in Figure 5.4a-d is limited to a small region below the surface and not representative of the entire thickness of the sample. In Figure 5.4a, the primary crack-tip is arrested at the twin interface; further loading causes the primary crack-tip to blunt while a new crack is observed on the surface on the other side of the twin, some distance away from the twin boundary, on a parallel basal plane (Figure 5.4b). Additional loading causes this new crack to run forward and backward to interact with the twin boundary (Figure 5.4c). In Figure 5.4d, the two cracks link through the twin by non-basal cleavage. In this case, the pre-existing twin is not as effective in blocking the crack as in the case where the crack propagation direction was <10-10>.

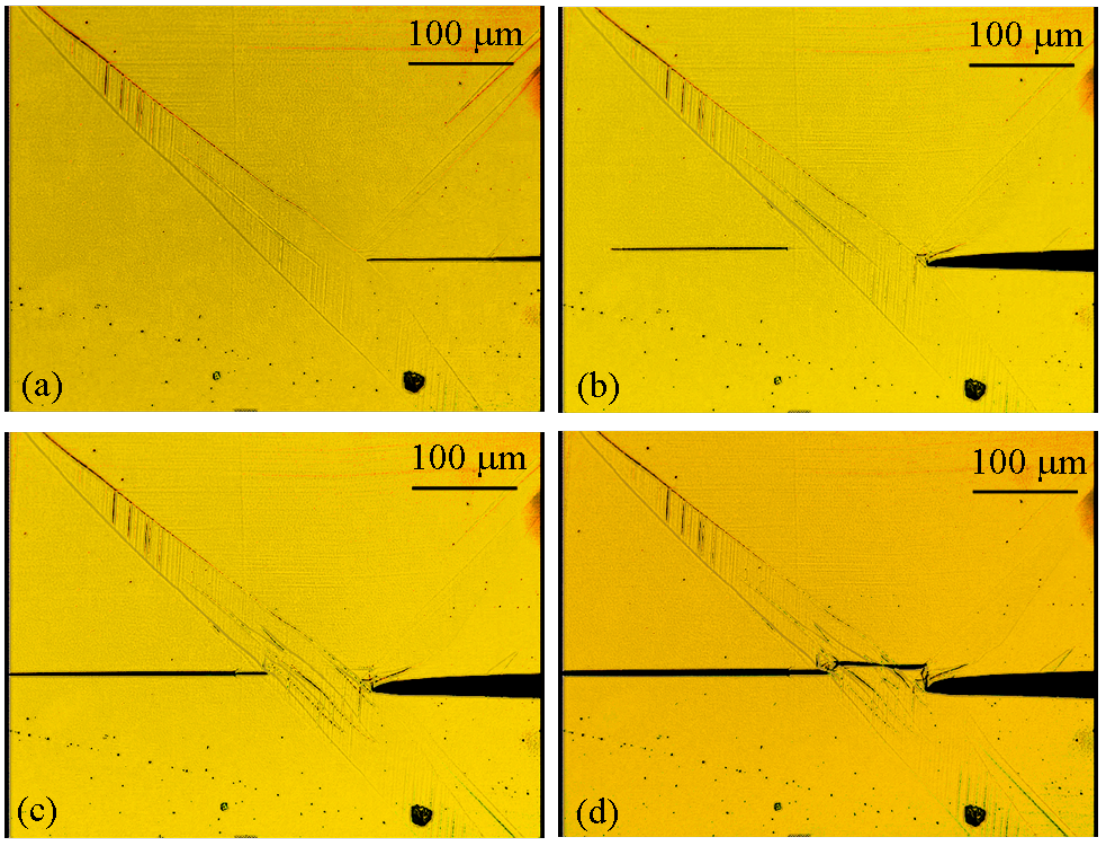

Figure 5.4. Crack-twin interaction in orientation 1: (a) crack-arrest at a pre-existing twin band, (b) a new crack in the parent region past the twin band and blunting of the original crack-tip, (c) the new crack has grown backwards in the parent to meet the twin boundary, and (d) linking of the two cracks by means of non-basal cleavage within the twin.

In this context, in hot-dip galvanized steel sheets, Parisot *et al.* [50] noted that zinc coating with pre-existing twins exhibited a significantly lower density of cleavage cracks upon loading as compared to coatings without twins. They proposed that twins could act as crack arresters due to the combination of the lattice rotation accompanying twinning and the propensity of zinc to preferentially cleave on the basal planes. Our observations confirm beyond doubt that this is indeed the case, and that the degree of resistance offered by twins depends on the disposition of the twin with respect to the crack growth direction.

5.1.2 Load-displacement curves

Load vs. extension curves for specimens 1-A, 1-B, 2-A and 2-B are compared in Figure 5.5; the ordinate is reported as Load/(Area moment of inertia) to facilitate comparison between the experimental and modeling data obtained from specimens of different thicknesses. If the test specimens are considered to be elastic double cantilever beams, then the relation between the applied load, P and the resultant vertical extension, δ can be expressed as follows:

$$P = (KEI)\delta,$$

where E and I are the elastic modulus and the area moment of inertia respectively, while K is a constant of proportionality, a polynomial function of the crack length and the length of the gripped region. Thus, the elastic part of the load-displacement curves of specimens of different dimensions must scale with their area moments of inertia.

Specimens 1-A and 2-A were tested in an Instron machine with a low magnification microscope attachment while 1-B and 2-B were tested *in situ* under an optical microscope using a micro-testing stage where a higher magnification (200x) was possible (The noise in the data corresponding to the latter specimens is due to the testing stage). The intermittent drops in load in the curves corresponding to specimens 1-A, 2-A and 2-B were correlated with the previously discussed dynamic crack extension events through *in situ* observations. Further, the magnitude of the load-drops seen in orientation 2 is significantly larger than that in orientation 1, suggesting a scaling with the size of the dynamic crack extension events. Specimens of orientation 1 were also able to sustain higher loads than those of orientation 2 (2-A and 2-B show a lower average load than that observed for specimen 1-A). Duplicate tests done in orientation 1 (specimens 1-B and 1-

C) to corroborate this last observation were hampered by the presence of multiple pre-cracks and hence macroscopic bridging ligaments that affect the load-displacement curves. However, once the intervening ligament was cut off by means of a razor blade

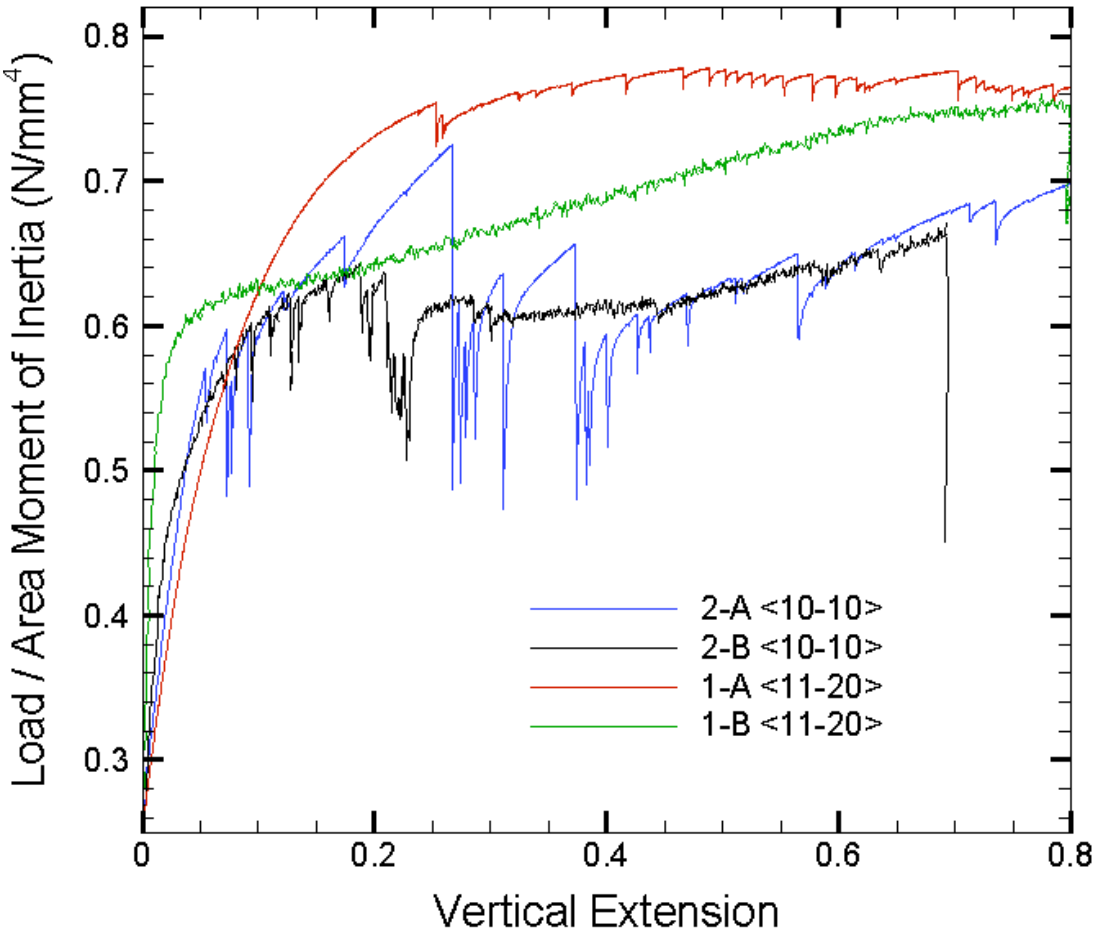

Figure 5.5. Load-vertical extension curves for the double cantilever specimens in orientations 1 and 2.

and the specimen was re-loaded, a macroscopically planar crack could be propagated (specimen 1-B) and the result is seen in Figure 5.5. The magnitude of the load-drops can still be compared with those of the other specimens and it is evident the response is dissimilar to those seen for specimens 2-A and 2-B and closer to that for 1-A.

5.1.3 Fracture surface observations

The difference in crack propagation behavior between the two orientations is further appreciated by an examination of the fracture surfaces. Representative micrographs are shown in Figures 5.6a and 5.6c. They both have a bright mirror-like

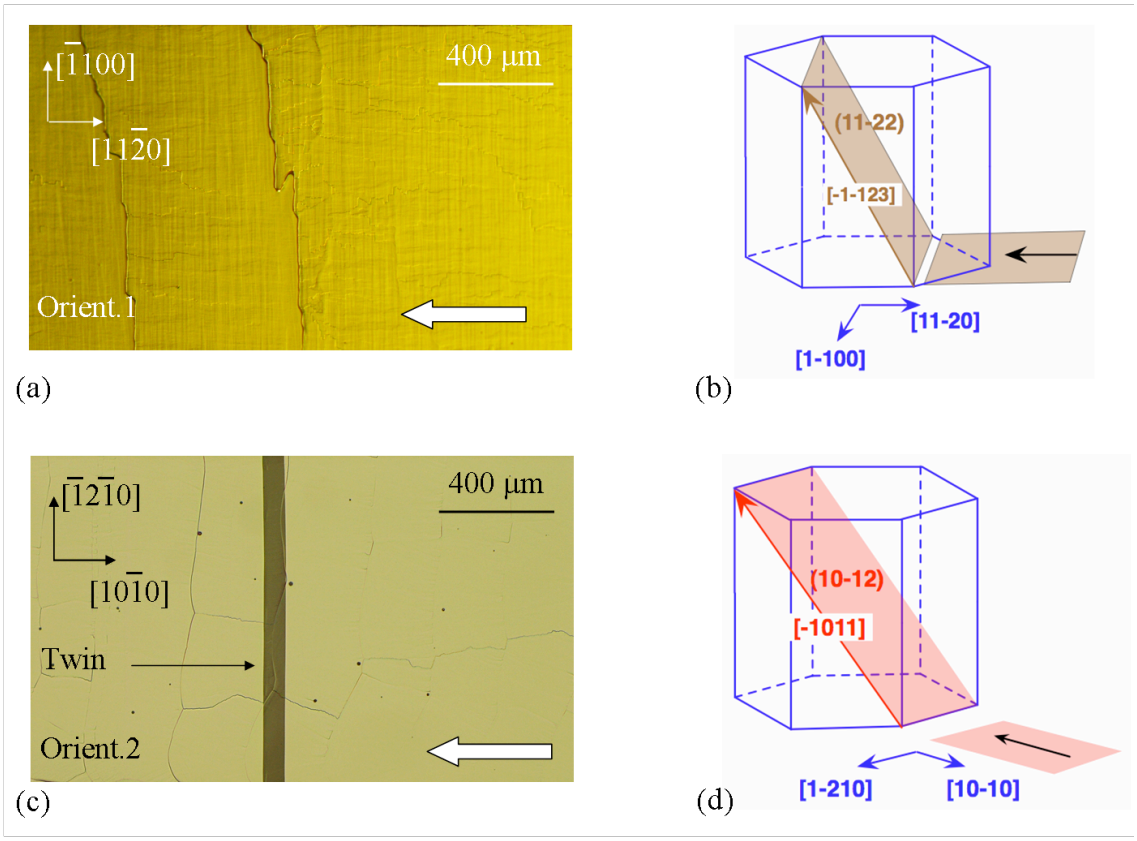

Figure 5.6. (a) Fracture surface from a specimen with orientation 1, where pyramidal slip traces are evident. (b) Schematic of a hexagonal cell showing the arrangement of the crack plane, crack propagation direction (black arrow) and a dominant pyramidal slip system. (c) Fracture surface from a specimen with orientation 2, and (d) corresponding schematic illustration of the dominant twinning system with respect to the crack geometry. The white arrow in (a) and (c) denotes the crack propagation direction.

appearance when viewed by the naked eye, but microscopic examination showed the presence of cleavage steps, slip traces and twins. In addition, there was a high incidence of slip traces perpendicular to the crack propagation direction on the fracture surfaces of

all specimens with orientation 1 whereas significantly fewer were observed in the case of orientation 2; those present were lesser in intensity making observation difficult. The few slip traces observed in specimens of orientation 2 were oriented at 30° to the crack propagation direction. In both cases, the orientation of the slip traces is suggestive of slip along the <11-22> pyramidal planes. Pyramidal slip of the type {11-22}<11-23> during basal cleavage has been documented by several authors [29-31], and is therefore not surprising. However, it is interesting to note that in orientation 1 most of the pyramidal slip traces were perpendicular to the crack propagation direction indicating that only two of the six possible pyramidal slip systems, which are mirror reflections of each other about the basal plane, were dominant (Figure 5.6b). It is noted that the slip traces on the fracture surfaces in orientation 1 formed in the wake of the crack for there would not be any topographical evidence left of these traces had they formed prior to crack propagation. Topographical evidence of basal slip cannot be obtained from fracture surfaces as these slip traces would be parallel to the basal plane. But basal slip is expected and has been observed after basal cleavage in zinc by means of Berg-Barrett X-Ray topography by Burns [29].

In one instance of fracture in orientation 2, in Specimen 2-D, the fracture surfaces showed twinning at frequent intervals along the crack propagation direction; these twins appear as 40-80 μm wide bands parallel to the crack front along a <11-20> direction often extending through the entire thickness of the specimen. An example of this can be seen in Figure 5.6c. The above-described geometry of the twins indicates that the habit plane is {10-1x} (See Figure 5.6d). As only {10-12}<10-11> twins are common in zinc, we suppose that this is the case here. Just as in the case of pyramidal slip in orientation 1,

the orientation of twins indicates that only two twinning systems oriented symmetrically about the crack plane are dominant.

If these coarse twins were generated ahead of the crack-tip during crack propagation along the <10-10> direction, the advancing crack would continue to grow along the basal plane within the twin as seen in Figure 5.3. Then, the angle between the exposed regions of the twin and the parent measured about the crack front should be either 86° or 94°. However, when the fracture surface topography was characterized using a white light interferometer, this angle was found to be ~4° in all the cases, suggesting that the twins were generated in the wake of the crack.

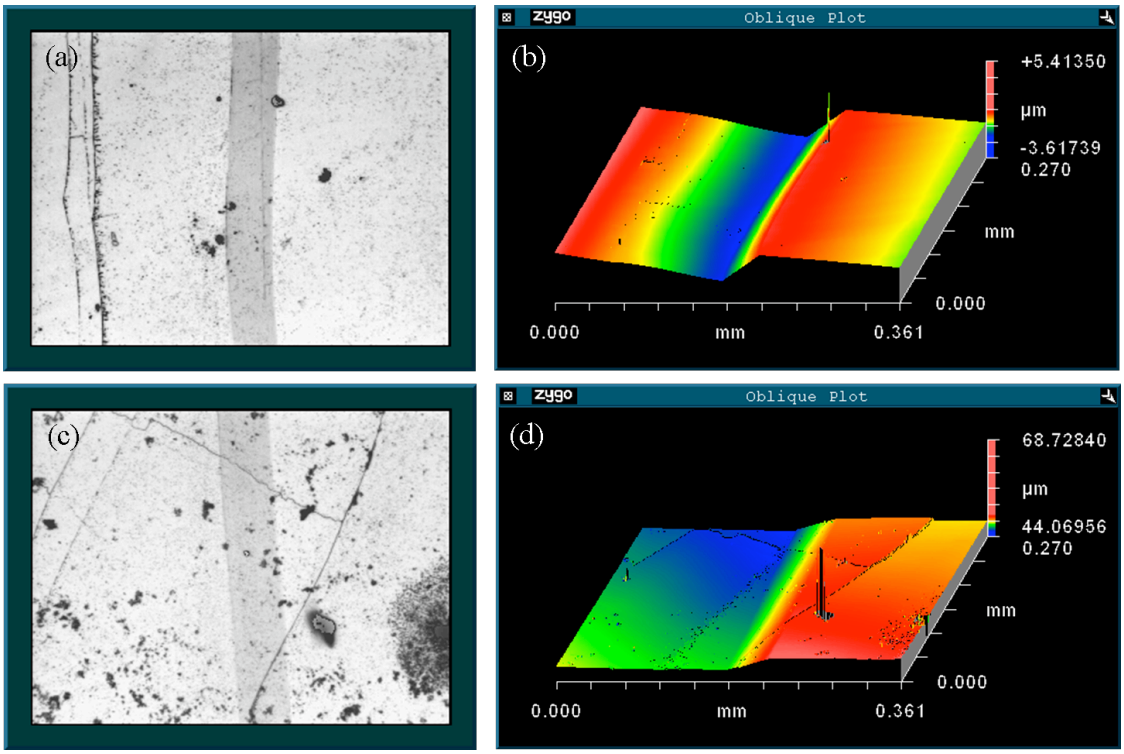

Figure 5.7. Characterization of twins on fracture surfaces: (a) A {10-12}<10-11> twin band on the fracture surface for orientation 2, (b) topology of the region shown in (a), (c) a mirror twin band on the matching fracture surface, and (d) topology of the region displayed in (c).

In Figures 5.7a and 5.7c, twins are shown from a specific location on mating fracture surfaces of specimen 2-D. Careful microscopic examination coupled with topographic analysis (Figures 5.7b and 5.7d) confirmed that the two twins are not one and the same. This is in further support of the idea that these twins emerged in the crack wake on the fracture surfaces and did not occur ahead of the crack-tip.

The "river patterns" observed on the fracture surfaces arise due to the "linking of cracks" propagating on parallel basal planes. When two such cracks approach each other, a ligament is created between them that can undergo plastic deformation and ductile rupture leaving a step in relief. These steps are significant in understanding crack branching and ligament formation. A typical topographical map of a fracture surface is shown in Figure 5.8. The height of these cleavage steps ranges from 100-800 nm for both orientations (1 and 2). While they do not occur along any particular crystallographic direction, a large number of them appear to align parallel to the crack front or perpendicular to it. Their presence throughout the fracture surfaces in both specimens

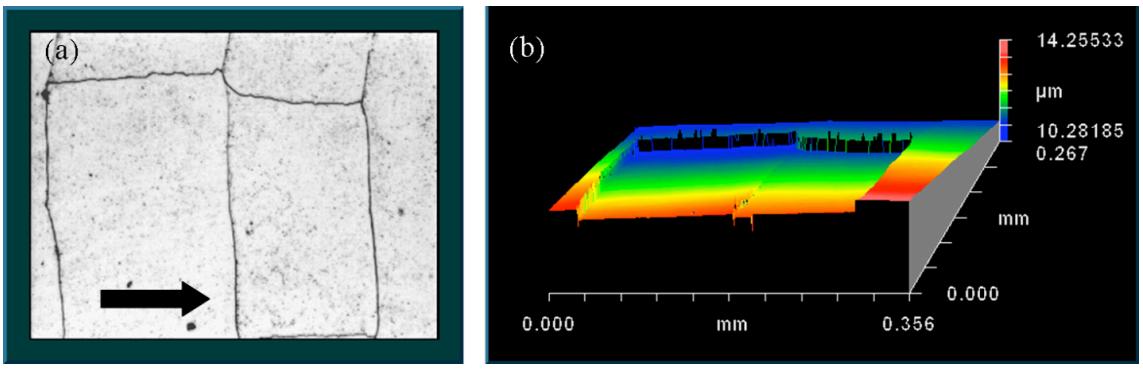

Figure 5.8. (a) Reference micrograph from a fracture surface showing cleavage steps both along the crack propagation direction (indicated by the black arrow) and perpendicular to it and (b) surface topology of the region in (a) obtained using a white light interferometer. Step heights are typically in the sub-micron range.

indicates that though cracks on different basal planes connect with each other early on, the crack front redistributes itself on multiple planes continually, in agreement with *in situ* crack growth observations (e.g. Figure 5.2).

5.1.4 Effect of macroscopic bridging ligaments

The formation of bridging ligaments between cracks on parallel basal planes and their rupture appears to be intrinsic to complete the fracture process. Therefore, it follows that the size and number of these bridging ligaments plays a central role in determining the energy that needs to be expended to propagate these basal cracks. The bridging ligaments previously discussed are of the order of sub-micrometer scale (100-800 nm). The effect of significantly larger ligaments of the order of hundreds of microns on retarding crack growth was examined using two specimens, 1-D and 2-E, containing two cracks. The two cracks in these specimens were not through-thickness cracks, but those that extended roughly halfway into the specimen thickness from opposite sides (Figure 5.9a). An additional schematic illustration and a low-magnification image of one these samples after some amount of crack extension are shown in Figures 5.9b and 5.9c, where the bridging ligament is seen. Specimens 2-E and 1-D had ligaments of approximately 150 μm and 250 μm in thickness respectively. These two samples sustained significantly larger loads for crack initiation and propagation as compared to those with single cracks (Figure 5.9d). The large drops in load from the peak indicate a large increase in crack length (~2 mm) that could be directly observed *in situ* in both the tests. The sustained lower level of load after the drop is primarily associated with plastic deformation of the ligaments, while the intermittent load-drops are indicative of small

amounts of crack extension. Specimen 2-E was unloaded during the test for a detailed examination and was reloaded. The unloading/reloading process is indicated by the loop in the load-extension curve in Figure 5.9d. Note that the load in Figure 5.9d is not normalized as in the case of Figure 5.5. The changes produced in these curves due to normalization will be on the order of a few Newtons, insignificant compared to the large differences in the load-displacement curves between the specimens with a ligament and those without. Continued loading beyond that shown in Figure 5.9d resulted in plastic bending of the arms of the double cantilever and eventual fracture of the specimen. The fracture surfaces in this case are similar to those in specimens with a single macroscopic crack. A similar situation was encountered in the case of Specimen 1-D, but the specimen could not be fractured completely and this is attributed to the greater thickness of the ligament.

The experimental observations presented here illustrate the complex nature of cleavage along the basal planes in zinc, previously thought to be one of the simplest examples of brittle fracture. Furthermore, the events that influence fracture in a perceptible way such as twinning and plastic deformation do not occur to the same extent in all the specimens suggesting a stochastic component to basal cleavage. Some of these events are potent enough to completely contain fracture. In particular, large ligaments and large twin bands ahead of the crack-tip were observed to provide significant toughening effects. Such extrinsic toughening mechanisms have been frequently documented in composites [51-53], but have only been occasionally invoked in pure metals and single phase alloys, as in the case of low-alloy ferritic steels by Iung and Pineau [54].

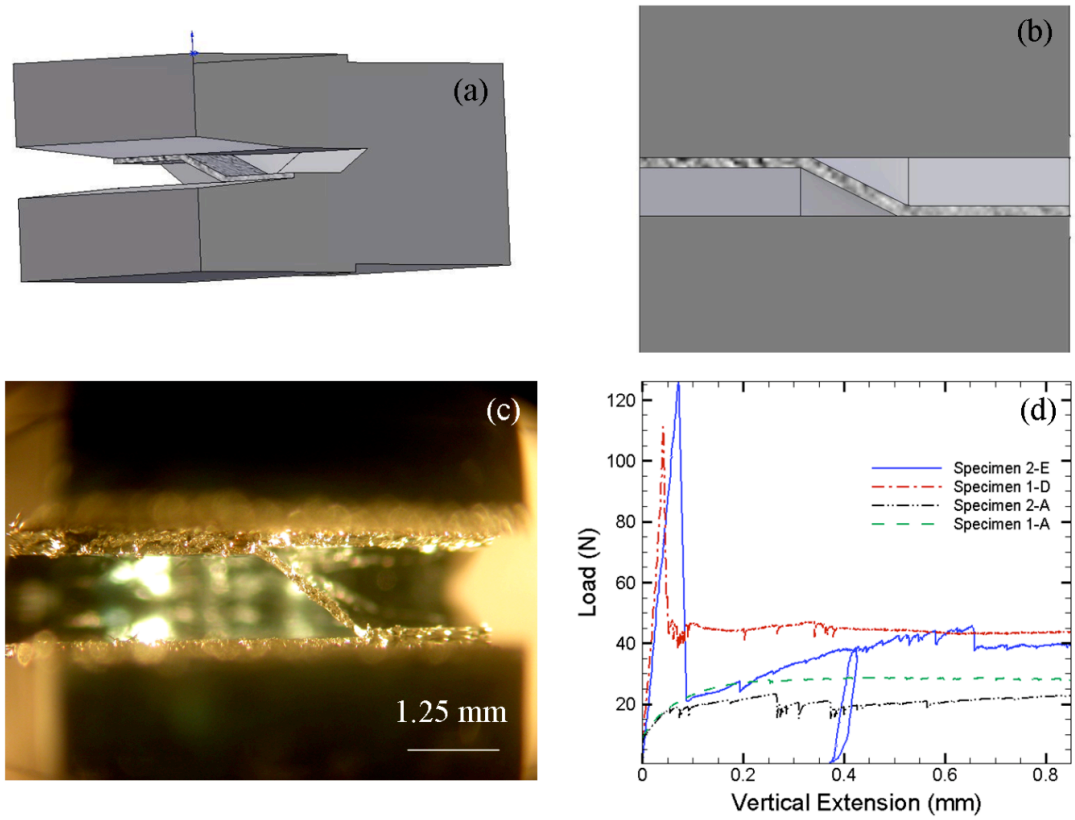

Figure 5.9. (a) Schematic illustration of a specimen with two cracks extending partway through the thickness from either side, producing a Z-shaped ligament, (b) an end-on view schematic illustrated in (a), (c) a Z-shaped ligament in a test specimen, and (d) load-vertical extension curves of double-cracked specimens compared to those with single through-thickness cracks.

5.2 Computational results

Basal cleavage in zinc, under the test conditions used in this study, consists of two steps, dynamic crack extension and arrest, the latter being accompanied by crack-tip blunting caused by plastic deformation. The arrest, being the controlling feature, was modeled using FEM and crystal plasticity to explain the experimental observations and to calculate the crack-tip stress fields and their relation to the crack growth direction on the basal plane. The total applied displacement was comparable to that observed in experiments during the crack-arrest period. The coordinate system adopted is as follows:

the crack propagation direction, thickness and the vertical are respectively the **1**, **2** and the **3** axes. Though it is customary to plot the results using dimensional groups, the results here are displayed in actual values of stress and length to enable a comparison with experiments.

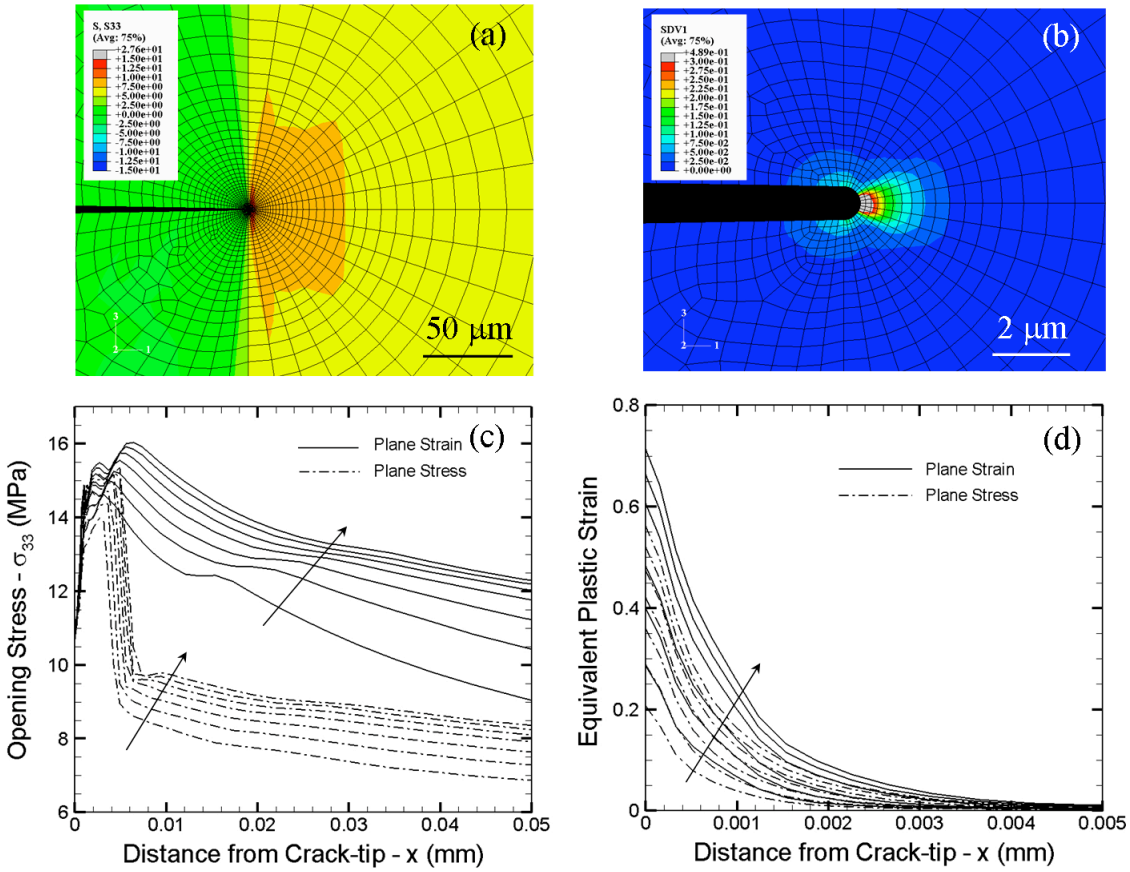

Figure 5.10. (a) Contour plot for a plane strain situation of the opening stress (σ_{33}) around a stationary crack-tip and (b) corresponding equivalent plastic strain contours (note that the image is magnified relative to (a)). The variation of σ_{33} (c) and equivalent plastic strain (d) with distance from the crack-tip for equal intervals of increasing applied displacement (as indicated by the arrows) in plane strain and plane stress.

Contour plots of opening stress in the **3** direction (σ_{33}) and strain fields for a stationary crack in a single crystal with orientation 1 are presented in Figures 5.10a and

5.10b; the evolution of the opening stress as well as the plastic strain near the crack-tip with increasing applied displacement for plane stress and plane strain is illustrated in Figures 5.10c and 5.10d. In all the cases, the stress first increases with distance reaching a peak at a location three to four times that of the notch diameter, following which it declines. This behavior is expected when large strain analysis is employed [55].

The differences between plane stress and plane strain are in line with what is expected and are better visualized with the help of Figures 5.11a and 5.11b, where the stresses and strains are plotted at the same value of applied displacement. In addition, the crystal plasticity solution is also compared against the one obtained for an isotropic material with a yield strength of 3 MPa and a strain hardening exponent of 0.1. This is done to demonstrate that the crystal plasticity solution follows the same trends exhibited by the isotropic case. The yield strength used for the isotropic case is equal to the critical resolved shear stress for pyramidal slip, which is about 10 times that of basal slip [29].

In order to investigate "mesh sensitivity", the mesh size was changed by increasing the number of elements while keeping the ratio between the largest and the smallest elements constant. In this analysis, the area of the smallest element was reduced from 0.05 μm^2 to 0.005 μm^2. These calculations were performed for plane strain, and for the same orientation discussed above. The variation of the opening stress and the equivalent plastic strain with distance for four different mesh sizes at the same value of applied displacement are shown in Figures 5.11c and 5.11d respectively. In the vicinity of the crack-tip, the solution is only marginally sensitive to the mesh size. Specifically, the solutions for the two finest meshes are much closer, suggesting the possibility of convergence upon further reduction of the mesh size. As only one layer of 3D elements

was used, a further reduction in the mesh size without changing the thickness would render the aspect ratio of the smaller elements too large and therefore unsuitable for computations.

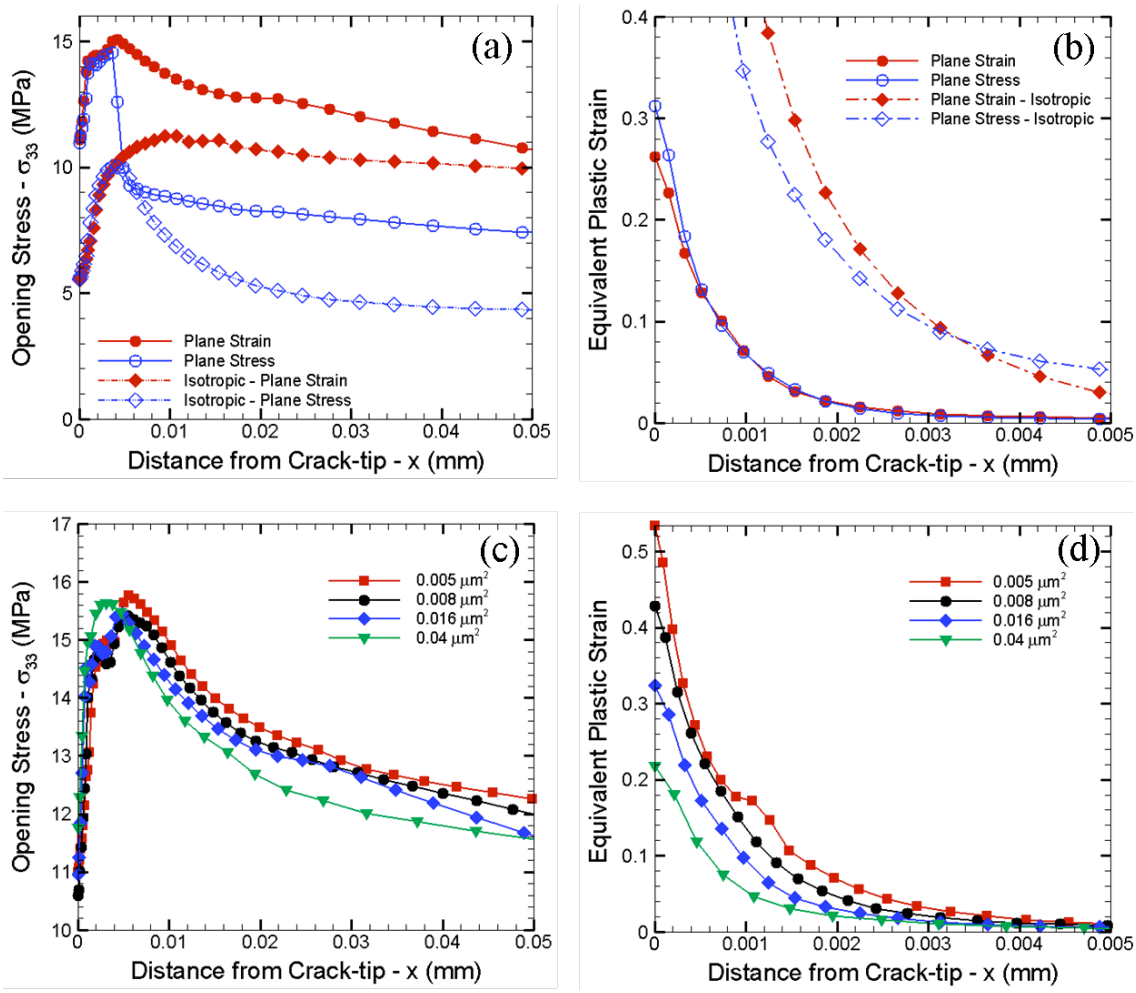

Figure 5.11. A comparison of (a) the stress distribution, and (b) the equivalent plastic strain ahead of the crack-tip for both crystal plasticity and isotropic plasticity calculations. Mesh dependence of (c) the opening stress, and (d) the equivalent plastic strain (the numbers in the legend indicate the area of the smallest elements). All the above plots are for orientation 1 and for an applied displacement of 34 μm.

The effect of crack growth direction (i.e. orientation 1 versus orientation 2) on the opening stress (σ_{33}) is shown in Figures 5.12a for the same applied displacement, and in Figure 5.12b for the same reaction force (load). These plots show that under similar

imposed conditions, the crack-tip region in the case of orientation 2 experiences a higher peak stress (by ~33%) than in the case of orientation 1, regardless of how the comparison is made. This difference is clearly borne out in Figure 5.12c, where the angular variation of σ_{33} is shown at a distance of ~4 μm from the crack-tip for orientations 1 and 2. For

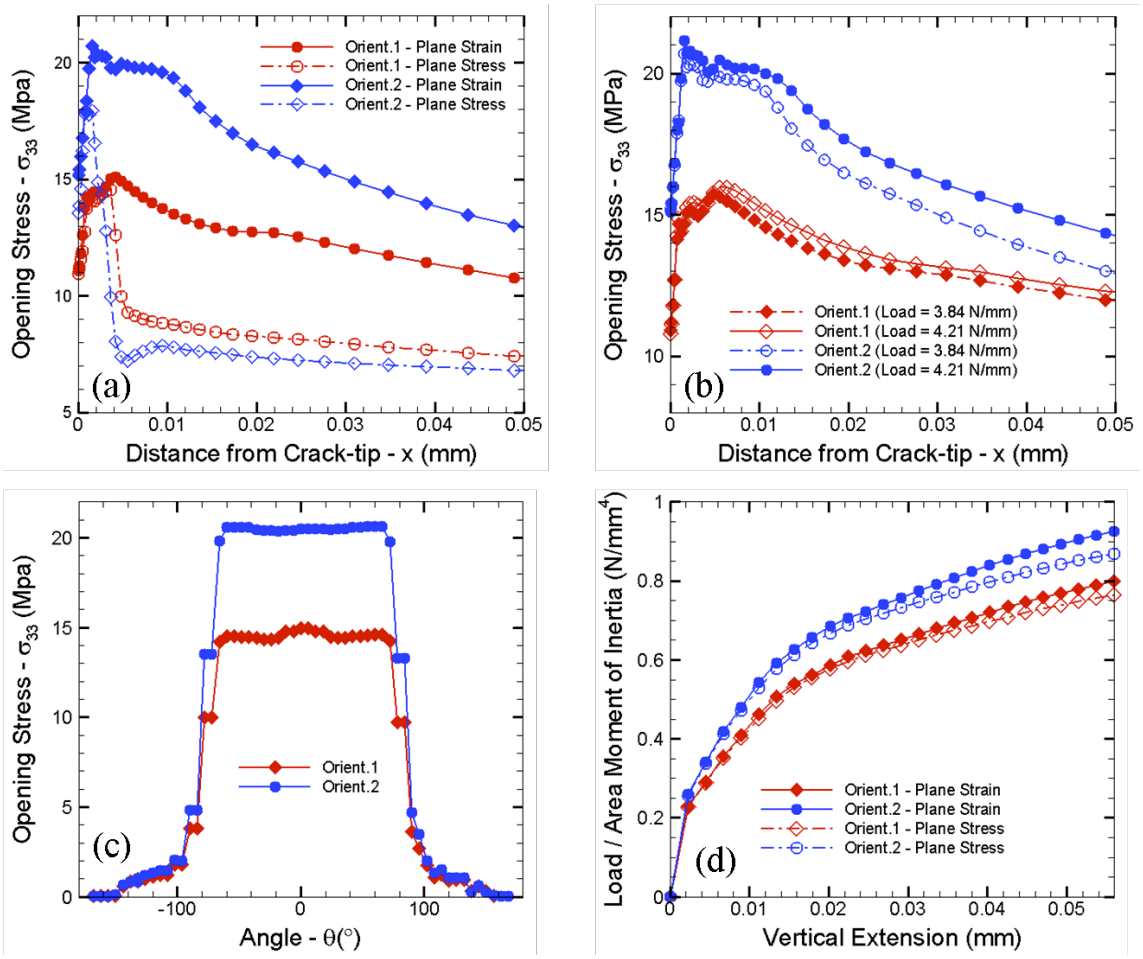

Figure 5.12. A comparison of the σ_{33} variation ahead of the crack-tip for the two orientations for (a) applied displacement and (b) for two different values of reaction force (load). (c) The angular variation of σ_{33} around the crack-tip for orientations 1 and 2 in plane strain, and (d) load-vertical extension curves for orientations 1 and 2 for both plane strain and plane stress.

both orientations, a constant stress sector between -66° and +66° is visible beyond which the opening stress drops rapidly. Lastly, in Figure 5.12d, the total reaction force is

plotted against applied displacement for both plane strain and plane stress for the two orientations. The magnitude of the load is comparable to that observed in the experiments (Figure 5.5); however, the orientation effect on the response is reversed in the computations relative to the experimental observations. The origin of this difference is discussed later.

These calculations reveal that in both plane strain and plane stress, and for both orientations, basal and pyramidal slip systems are active. A summary of the activity of the individual slip systems is presented in Table 5.1. The pyramidal slip systems are sub-divided into three pairs, each pair consisting of systems with mirror symmetry about the basal plane.

	Basal			Pyramidal					
				Set 1		Set 2		Set 3	
Slip Plane	(0001)	(0001)	(0001)	(2-1-12)	(-2112)	(11-22)	(-2112)	(1-212)	(-12-12)
Slip direction	[2-1-10]	[-1-120]	[-12-10]	[-2113]	[2-1-13]	[-1-123]	[11-23]	[-12-13]	[1-213]
Orient. 1 [2-1-10]	A	N	N	A	A	N	N	N	N
Orient.2 [10-10]	A	A	N	A	A	A	A	N	N

A – Active; N – Not Active

Table 5.1. Activities of individual slip systems in both orientations. Each pair of pyramidal slip systems are mirror reflections of one another about the basal plane.

Contours of accumulated plastic strain accommodated by the active basal slip system for orientation 1 are shown in Figure 5.13a, and the angular variation of the same at a distance of 4 μm from the crack-tip for both orientations is shown in Figure 5.13b.

The path along which the data are plotted is indicated by a circle around the crack-tip in Figure 5.13a. Contour plots for orientation 2 are similar to those seen in orientation 1, except for the magnitude, and are shown in Figures 5.13c and 5.13d. Figures 5.13e,f schematically illustrate the slip directions for the active basal slip systems observed in orientation 1 and 2 respectively.

In orientation 1, only one basal slip system with the slip direction along the direction of crack propagation dominates while the other two basal slip systems that are 60° away from the primary slip system are dormant (Table 5.1). This behavior is expected in the case of plane strain as the primary slip system in question has a significantly greater resolved shear stress and therefore dominates. In passing, we note that despite the absence of a displacement constraint in the third direction in plane stress, most of the basal slip is still confined to the same primary slip system.

Calculations in orientation 2 show that the two basal slip systems that are at 30° to the crack propagation direction are active, while the third system lying perpendicular to it, is dormant. As in the case of orientation 1, the two symmetrically oriented basal slip systems would produce an out-of-plane displacement if they operated individually; however, if both were active to the same degree as confirmed by Figure 5.13b, the displacements along the thickness direction cancel each other due to symmetry and can therefore be active in Mode I. The results in Figure 5.13b also show that for the same amount of applied displacement, the magnitude of strain along the active basal slip systems is considerably smaller in orientation 2 than in orientation 1.

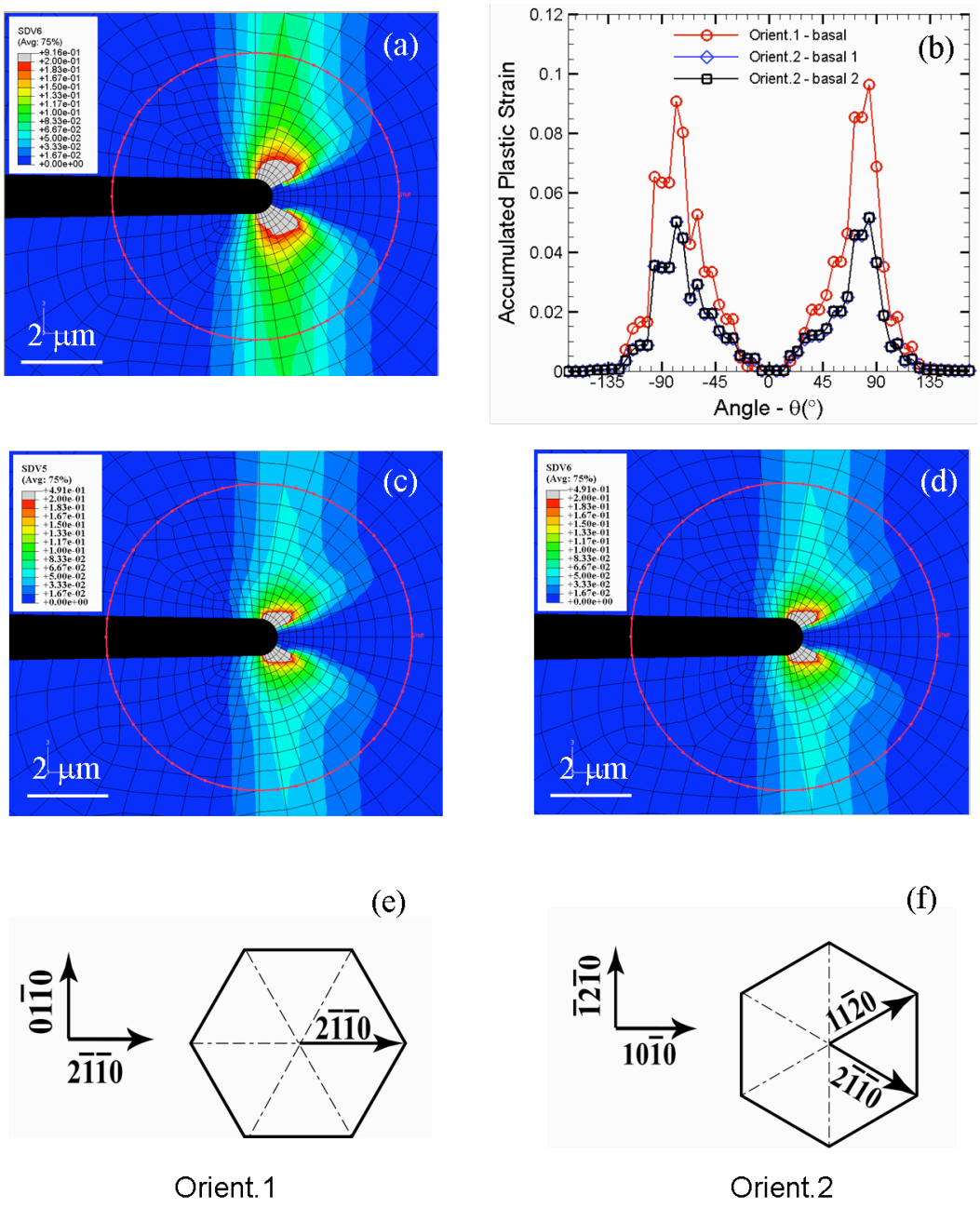

Figure 5.13. (a) Contour plot of accumulated plastic strain in the crack-tip vicinity for orientation 1 in the active basal slip system and (b) angular variation of accumulated plastic strain for both orientations at a distance of 4 μm from the crack-tip. (c,d) Contour plots of plastic strain accommodated by the two active basal slip systems in orientation 2. (e,f) Schematic illustrations of active basal slip directions for orientations 1 and 2 (indicated by arrows).

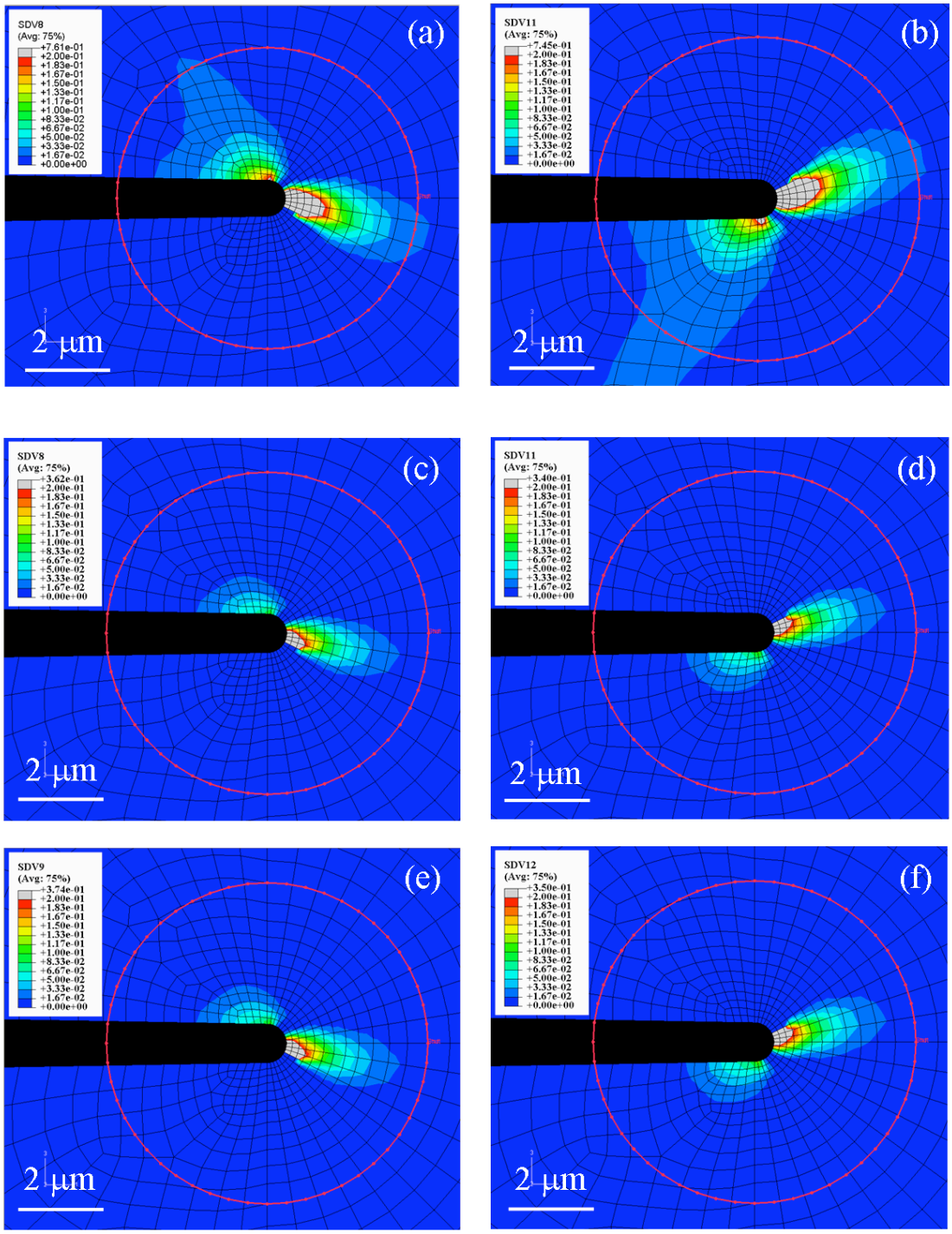

Figure 5.14. (a,b) Contour plots of accumulated plastic strain in the two active pyramidal slip systems for orientation 1. (c,d,e and f) Contour plots of strain in pyramidal slip systems in orientation 2. Note that (d) and (f) are pyramidal slip systems that are mirror reflections of (c) and (e) respectively.

There are two pyramidal slip systems oriented symmetrically about the crack plane that do not require an out-of-plane displacement and are the only active pair (Table 1). Figure 5.14a,b show the accumulated shear strain in these two active pyramidal slip systems in orientation 1. For orientation 2, four pyramidal slip systems are active, two of which are mirror reflections of the others about the crack plane. Contour plots of plastic strain accommodated by all the four slip systems are displayed in Figures 5.14 (c-f). The orientations of the active slip planes (one plane per symmetric pair (see Table 5.1)) in both orientations with respect to the crack plane and crack growth direction are schematically illustrated in Figures 5.15(a,b). Again, any of these slip systems in orient-

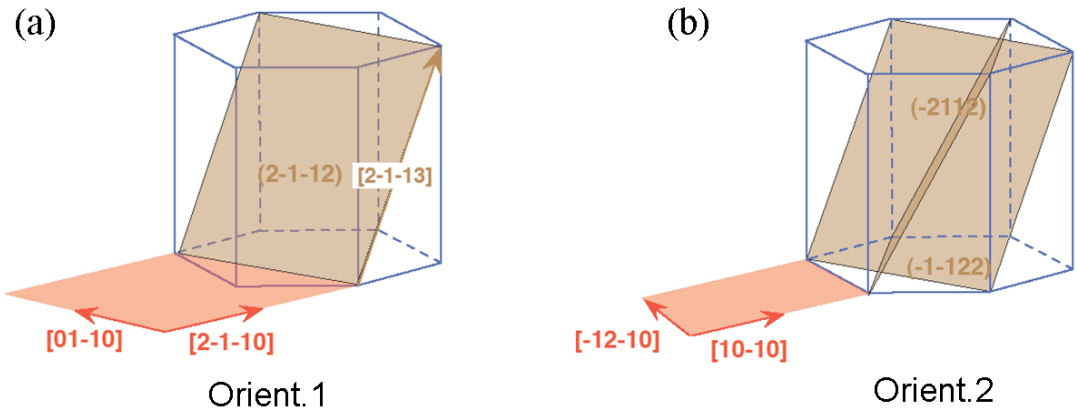

Figure 5.15. (a,b) Schematic illustrations of active pyramidal slip systems for orientations 1 and 2 with reference to the crack plane and direction (note: due to mirror symmetry about the crack plane, only half the active planes are shown).

-ation 2 would require an out-of-plane displacement if they were to activate individually, but due to their symmetric arrangement about the crack propagation direction, the displacements along the thickness directions cancel each other. The angular variation of strain in the pyramidal slip systems at a distance of 4 μm from the crack-tip is displayed

in Figure 5.16 for both orientations. The dashed curves are for the pyramidal planes that are symmetric counterparts of the ones shown in the solid curves. We can see from Figure 5.16 that the magnitudes of plastic strain are much smaller in the case of orientation 2 compared to orientation 1 (as was the case for basal slip) and is consistent with experimental observations of pyramidal slip traces (presence or absence) on the corresponding fracture surfaces.

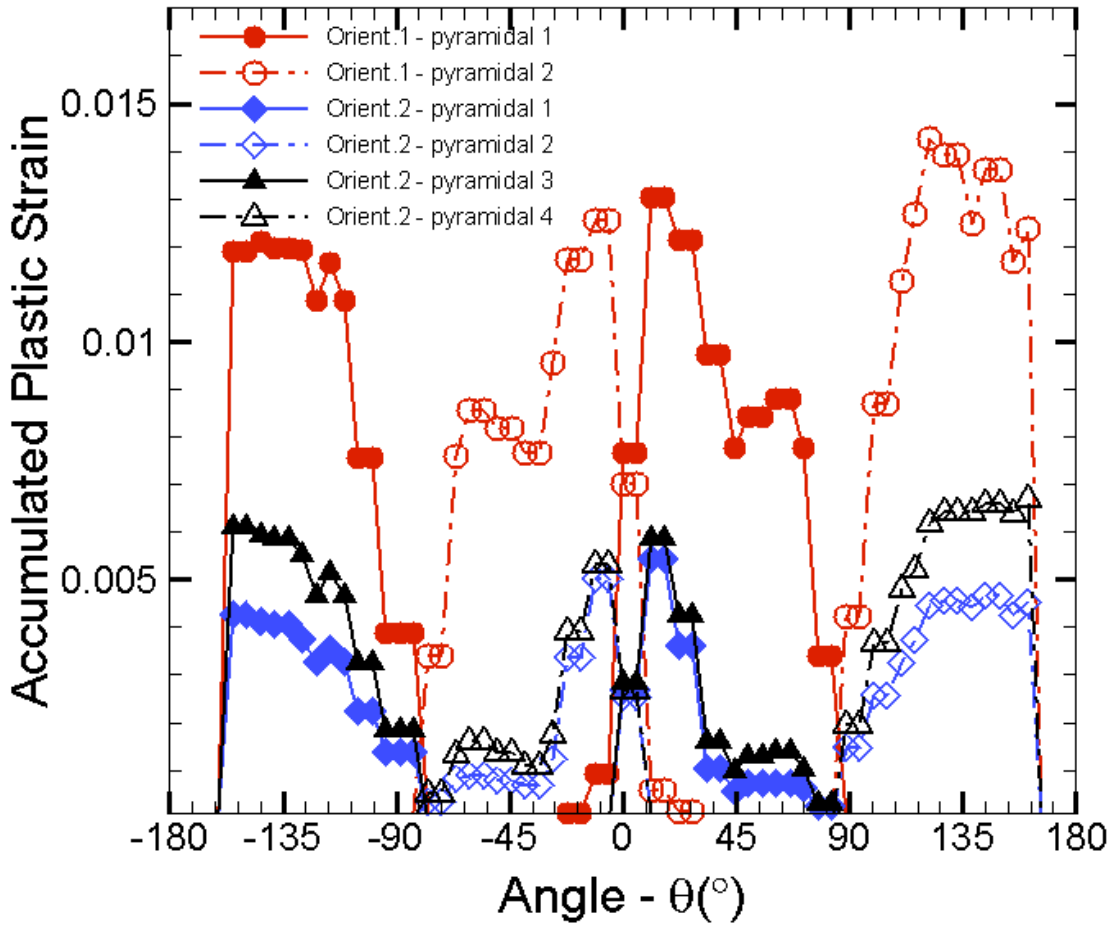

Figure 5.16. Angular variation of accumulated plastic strain for both orientations at a distance of 4 μm from the crack-tip (The dashed curves indicate strain in slip systems that are mirror reflections of the ones represented by the solid curves).

5.3 Discussion

A combination of careful *in situ* observations coupled with finite element analysis incorporating crystal plasticity has yielded new insights into the micromechanisms of crack propagation on the basal plane in single crystals of zinc. Specifically, the study has shown that cracks experience alternate periods of dynamic crack growth and arrests. Such a response is anticipated during quasistatic loading of a stationary crack-tip in brittle materials [7]. When the loading rate is small enough, as is the case in this study, the energy available for fracture (elastic energy and kinetic energy) eventually dissipates, causing the crack to arrest. During rapid crack growth, the high strain rates in the vicinity of the crack-tip suppress plastic deformation; but upon arrest, quasistatic conditions are regained and the crack-tip experiences blunting due to plastic deformation.

For further crack growth, the blunt crack must re-sharpen, or alternately, a new crack must nucleate either on the same plane or on a parallel basal plane. Computational analysis has shown that the maximum opening stress occurs at a small distance away from the crack-tip, and that this stress remains constant between -66° and +66° about the crack-tip. If the criterion for crack nucleation is assumed to be a critical value of opening stress, then it is reasonable to expect a micro-crack to nucleate a slight distance away and not necessarily on the same basal plane as the existing crack as observed in the experiments. These microcracks can nucleate heterogeneously at dislocation networks and locks or internal defects such as voids or inclusions within the region of the highest opening stress. The connecting ligament between the old and the new cracks shields the new crack-tip and eventually fails in a ductile manner, leaving a step on the fracture surface *parallel to the crack front*. It is interesting to note that this mechanism is quite

similar to that observed in ductile materials, where void nucleation occurs a slight distance ahead of the crack-tip for similar reasons [7]. The material between the main crack and the newly nucleated void subsequently fails, causing the void to connect with the main crack to produce crack growth. Here, however, there is nucleation and dynamic propagation of a microcrack ahead of the crack-tip. The difference between void growth and coalescence and the mechanism proposed here is that the former is controlled by the hydrostatic stress while the latter occurs when the opening stress reaches a critical value.

In a thick specimen, such as the ones used in this study, multiple micro-crack nucleation events on parallel basal planes are possible along the crack front in the thickness direction. These micro-cracks subsequently grow towards one another, link, and produce steps on the fracture surface that are *normal to the crack front*. The events described above repeat many times over, leading to macroscopic failure, and account for the features observed on the fracture surface.

An interesting finding in this study is the dependence of crack-growth behavior, the associated load-displacement curves, and the fracture surface morphology on the crack propagation direction (orientation 1 versus orientation 2). Computations illustrate that for the same applied displacement, higher stresses are felt near the crack-tip in orientation 2 (~33 % - see Figure 5.12c). Then it follows that in order to reach a critical value of opening stress, a lower load is required for crack extension in case of orientation 2 in comparison with orientation 1, a prediction consistent with experimental observations (Figure 5.5). Since the model does not allow for crack growth, higher stresses, and therefore higher remote loads, are encountered in the computations for orientation 2 and this explains the apparent contradiction between computations and

experiments (compare Figures 5.12d and 5.5). We note that a simple critical opening stress criterion adopted here is different from the modified cleavage criterion used by Parisot *et al.* [50] that accounts for prior basal slip. Here, as seen in Figure 5.13b, the total strain accommodated by basal slip is the same in both orientations, although it is different for the individual slip systems, and thus should not affect the argument provided. Furthermore, any modified cleavage criterion should necessarily include the role of pyramidal dislocations and their interaction with basal dislocations, and at present, the influence of this interaction on cleavage is not known.

There is good agreement between the experiments and the computations with regard to the particular slip systems that are active. From the strain contours (Figures 5.13 a,c,d and 5.14), it is clear that the slip systems that operate ahead of the crack-tip are also active in the crack-wake. Thus, slip traces observed on the fracture surfaces resulting from slip in the crack-wake, are indicative of active slip systems ahead of the crack-tip.

The dynamic crack extension distances were also found to depend on the direction of crack growth on the basal plane (orientation 1 versus orientation 2) and affect the magnitude of the associated load-drops. There are a few possible reasons for this difference. The first is that there is a larger amount of stored energy in orientation 2 just prior to dynamic crack propagation and to determine if this is indeed the case would require a full dynamic analysis which is beyond the scope of this study. The second possibility is that the material ahead of the arrested and blunted crack-tip is modified by the associated plastic deformation to render it less resistant to fracture in orientation 2. From the computations it is seen that the number of active non-parallel slip systems in orientation 2 is greater, allowing for the possibility of formation of dislocation networks

and locks, producing local hardening. This hardening could influence the subsequent dynamic crack growth event. In this context, Messmer *et al.* [31] examined the influence of pre-strain on fracture toughness and found that the forest dislocation density in the vicinity of the crack-tip adversely affected the toughness. Lastly, for both orientations, crack growth velocities are faster than the data collection rate, and therefore it is conceivable that the velocities for the two orientations could be different and that this could influence the size of dynamic crack extension distances.

The role of ligament toughening has been extensively discussed in the literature for various multiphase materials and composites [51, 56, 57], but not as often in pure metals. When a crack propagates on a single basal plane unstably in a brittle material like zinc, it will encounter minimal resistance. However, the presence of multiple cracks creates ligaments of different geometries between them that force plastic deformation, ductile rupture and/or non-basal cleavage that hinder crack propagation and sometimes even completely arrest it, as seen in specimen 1-D. In the context of polycrystalline materials, this behavior is significant for enhancing intragranular toughness. In addition to these ligaments, materials that fail by brittle transgranular fracture also exhibit cleavage steps and tearing in the vicinity of the grain boundary that can be attributed to the presence of multiple cracks and the associated ligaments arising as a consequence of misorientation of the preferred fracture planes across grain boundaries. Such ligaments at grain boundaries also contribute significantly to shielding cracks and retarding their propagation [1-3].

Pre-existing twins ahead of the crack-tip can also provide resistance to crack-growth depending on their geometry. If a large fraction of the crack front comes into

contact with a coarse pre-existing twin in which the preferred fracture plane is unfavorably oriented with respect to the loading direction. (e.g. 94° or 86° rotation of the basal plane within the twin with respect to the parent in the case of Zn as shown in Figure 5.3), crack propagation through the twin becomes difficult, and in the extreme case, can arrest. However, if only a small part of the crack front interacts with a pre-existing twin, as in the case of crack propagation in orientation 1, the twin becomes a bridging ligament offering minimal resistance and ruptures by non-basal cleavage.

On the whole, this investigation into basal cleavage in single crystals has resulted in several new and interesting observations that were not documented before, and provided new insights into brittle fracture in general. This was made possible by the use *in situ* testing, a technique that has not been applied to study fracture in zinc in the past. Though dynamic crack growth and arrest are well known features of brittle fracture, the consequences of crack arrest in metals presented and discussed here are new observations. As our experiments have revealed, plastic deformation that follows as a result of crack arrest can have significant influence on crack propagation. Formation of crack ligaments that can produce toughening effects by forcing the crack to grow on multiple basal planes is a direct consequence of crack-tip plasticity, as are the differences observed in crack growth in the two different orientations studied here.

The treatment given by previous researchers to the problem of basal cleavage as a simple separation of atomic planes, and the consequent estimates of fracture toughness and fracture energy can be called into question in light of these new observations. In addition, the role of in-plane orientation on crack growth, and the interaction of growing cracks with important microstructural features like twins, must be taken into account in

these analyses. One of the most significant observations made in this study is the enormous amount of resistance provided by macroscopic crack ligaments as well as pre-existing twins that can, under certain conditions, completely contain crack propagation. This is especially relevant if one considers the fact that the fracture toughness of zinc is extremely low (~ 1 MPa$\sqrt{m}$).

In the next chapter, the role of another crystal defect (grain boundaries) in retarding crack growth is explored in detail through fracture experiments in bicrystals of controlled misorientation.

Chapter 6

Bicrystals: Experimental Results & Discussion

Eight bicrystal specimens of four twist misorientations namely, 10º,20º, 30º and 45º, were tested during the course of this study. A four character symbolic notation will be used hereafter to refer to specific samples. The first character refers to the testing machine employed: specimens tested using an Instron testing machine will begin with an "I" and those that were tested using the Deben Microtesting Stage will begin with an "M". The next two characters represent the twist angle "θ" in degrees. The final character is simply "A" or "B" with the purpose of distinguishing between duplicate specimens. Thus, a 10º bicrystal tested in the instron would be referred to as "I10A", and a 20º duplicate specimen tested in the microstesting stage would be "M20B".

Crack propagation was monitored using a traveling microscope in tests conducted on the Instron machine, while a metallurgical microscope was used for specimens tested using the microtesting stage. Lack of high resolution coupled with the high reflectivity of the sample surfaces created difficulties in observing the microstructural events ahead of a crack-tip using the traveling microscope. Only a rough idea of the location of the crack-tip was possible, but no information pertaining to twinning or slip could be obtained using this method. The use of a metallurgical microscope instead proved highly effective in monitoring and documenting important microstructural events in real time. Thus the observations made in the tests conducted using the Instron machine were not truly *in situ*, at least not to the extent desired for this study.

The specimen geometry as well as the method of testing were a variation of existing methods and have not been previously attempted on zinc single crystals or bicrystals. Hence, initial testing on single crystals was used as a way to verify the usefulness and practicality of this method. Tests on single crystals confirmed that controlled crack growth was possible by using an Instron machine at a crosshead speed of 2 mm/hr while gluing a length of ~5 mm on the top and bottom surfaces to stainless steel grips. So, the same method was applied to specimens I10A and I30A. The observations from specimens of each of the twist angles are first discussed sequentially, and subsequently, a discussion on the effect of the magnitude of the twist angle is given. All the optical micrographs showing the interaction of the main crack in the first grain with the grain boundary have the first grain on the right and the second grain on the left i.e., the direction of crack growth in all these figures is right to left.

6.1 The 10º twist misoriented bicrystals

The first bicrystal sample I10A was tested using an Instron machine. In this test, the main crack in the first grain came to a halt at the grain boundary, and as the applied displacement continued to increase beyond this point, the arms of the double cantilever began to bend, causing the crack faces in the first grain to separate to a greater extent. After testing, both the side surfaces of the specimen were examined; on one of the sides, two parallel cracks separated by ~250 μm were found in the second grain. This region is shown in Figure 6.1a, and magnified views of these two cracks are displayed in Figure 6.1b, where the material between the two cracks has preferentially undergone slip. One of these cracks connected with the crack in grain 1 indicating some degree of crack

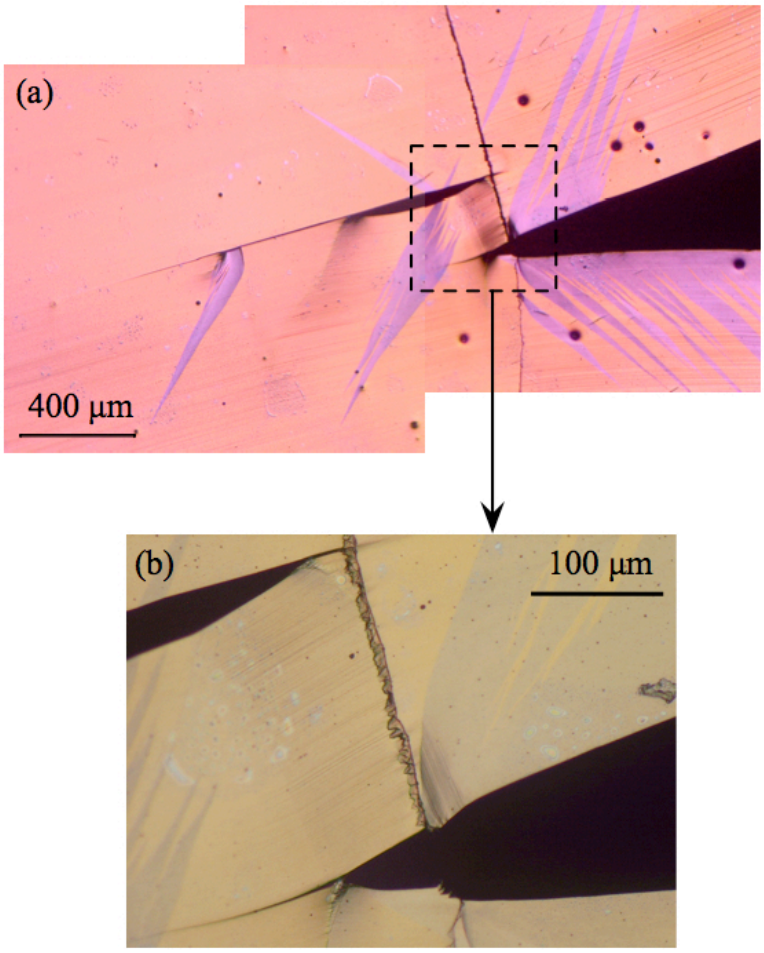

Figure 6.1. (a) Crack-grain boundary interaction in a 10º twist bicrystal (I10A) photographed using polarized light. (Grain 1 is on the right and grain 2 is shown on the left.) (b) Two parallel cracks in the second grain are seen, the lower of which has connected with the main crack in the first grain. Magnified image of the inset in (a) showing serrations near the grain boundary region.

transmission across the grain boundary on the surface. The sequence of events, however, is unclear. Additionally, the twist angle precludes knowledge of the extent of crack transmission beneath the surface. There is also considerable slip and twinning in the wake of the main crack in the first grain, and also near the cracks in the second grain to some extent.

The cracks in the second grain do not reach the end of the crystal as in the case of single crystals. In this particular case, the larger crack grew only to a length of ~1 mm.

Beyond this the applied displacement is accommodated primarily by deformation in the cantilever arms with virtually no crack extension. Some of it is also accommodated by deformation in the layer of material enclosed by the two parallel cracks in the second grain.

When the opposite side of the same specimen was examined, no cracks were seen on the surface as Figure 6.2a shows. Only twinning in the crack-wake in the first grain and significant amount of slip were evident. While twinning seems to occur in the vicinity of the crack-tip, slip is prevalent at large distances from it, as evidenced by Figure 6.2b,c. This indicates that this deformation is not primarily due to the crack-tip stress fields, but due to the plastic bending of the cantilever arms. One can also discern a kink band in the lower half of the specimen in the second grain at a ~12º angle to the grain boundary (see Figure 6.2a). The color contrast here in polarized light indicates a discontinuity in the out of plane displacement across the kink boundary.

The lack of cracks on the second surface clearly shows that the cracks observed on the first surface do not extend through the entire thickness of the specimen. This observation is especially relevant in light of the extremely low intrinsic toughness of the material and gives a clear indication of the potency of the grain boundary in resisting crack propagation; in contrast, if such a macroscopic crack were present in a single crystal, it would have grown quite readily to a through-thickness crack as our experiments on single crystals have shown (see Chapter 5). One can also use this information to conjecture that there could be cracks buried in the interior regions of the specimen that did not grow to reach the surface to permit observation.

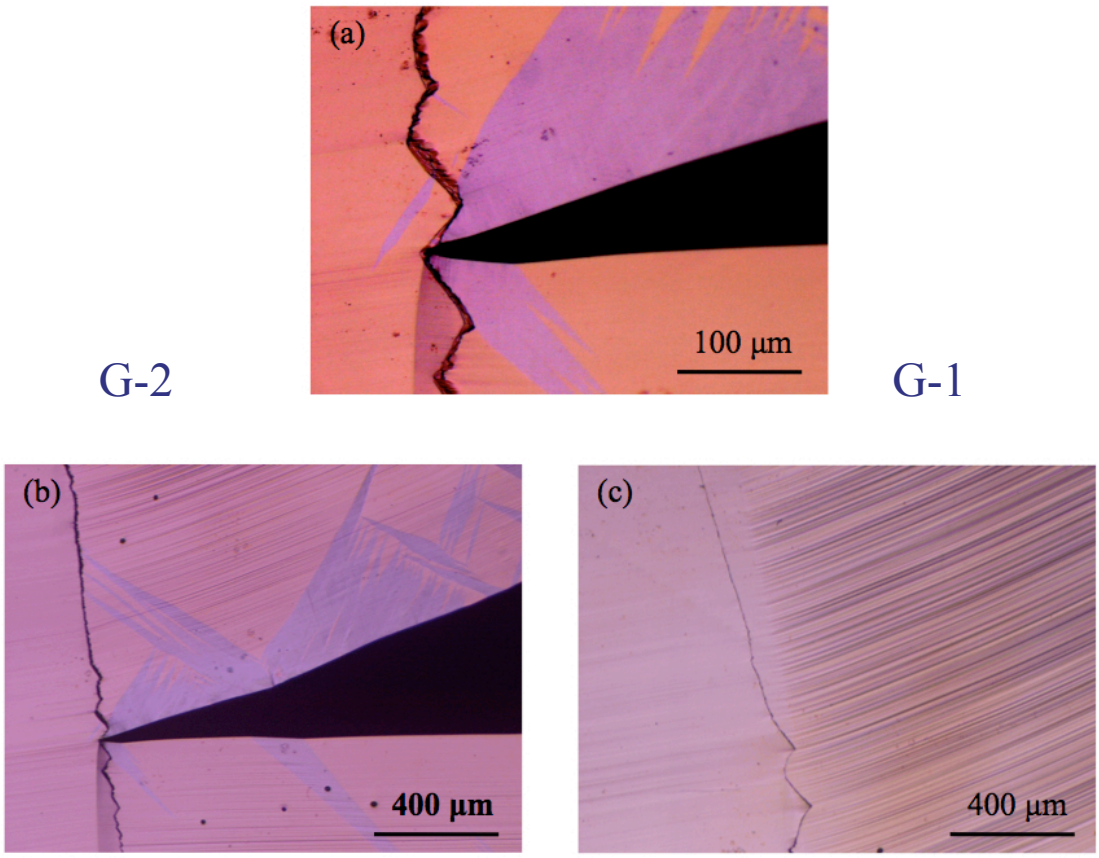

Figure 6.2. (a) Crack - grain boundary interaction in I10A on the second side to the one shown in Figure 6.1(a). No crack transmission through the grain boundary is seen here; instead, a kink band developed in the second grain. (b) and (c) Low magnification images showing plastic deformation in the first grain: twinning in the crack-wake in (b) and basal slip in (c). Grain 1 is shown on the right and grain 2 appears on the left.

Though crack propagation is discouraged by the grain boundary, the load sustained by the specimen did not change substantially once the crack began interacting with the boundary. This is perhaps due to the low critical resolved shear stress on the basal planes. As the loading axis is several millimeters away from the grain boundary, the cantilever arms are very compliant and undergo extensive bending. Consequently, there is shear between the grips and the glued regions of the specimen, causing the glue to fail at lower values of normal stress than it would have had there not been any shear. If the gripping length is increased to 8-9 mm from ~5 mm, used in the test described

above, and the rotation of the grips is constrained, then such large scale plastic bending could likely be suppressed. In addition, the constraint on rotation can prevent premature failure of the glue and hence the specimens can be deformed to a much greater extent. These features were incorporated into the grips used for subsequent testing in the microtesting stage. This stage can be placed under a metallurgical microscope where higher magnifications are possible and hence much more detailed observations of microstructural events can be made, and their sequential occurrence can be documented. For instance, in specimen I10A, the exact moment at which the crack in the first grain encountered the grain boundary could not be identified on the load-displacement curve. By using the microtesting stage, this and other important details regarding crack-grain boundary interaction can be documented.

Usually, in controlled crack propagation experiments, the crack-tip at the beginning of the test is always a good distance away from the loading axis as in the case of compact tension geometry. However, the above-described changes to the loading configuration would ensure just the opposite, bringing the geometry closer to that of an edge-cracked tension specimen. But once the crack grows to reach the boundary, the previous configuration is regained. The response of the specimens during the initial crack growth in the first grain is expected to be different as a consequence of these changes in the loading configuration, but is of little consequence during the interaction of the crack with the grain boundary. Specimen M10A was tested in this fashion and showed very similar behavior to that of specimen I10A. The load-vertical extension curves for these two specimens till a vertical extension of 1.4 mm are shown in Figure 6.3, where the similarity in the mechanical response is evident from the average load

sustained by the specimens. The higher load seen in Specimen M10A indicates that the testing fixture achieves the intended increase in the stiffness. Similarities are also evident in the microstructural features such as slip, twinning and kink bands.

There are, however, certain differences between the two 10º twist bicrystals: in specimen M10A, the crack halted 60 μm before the grain boundary and did so earlier than in I10A; there was a sharp peak observed in the load-displacement curve in M10A when the crack nearly reached the grain boundary. After applying a vertical displacement of ~2 mm (not shown in Figure 6.3), the sample was unloaded, and examination revealed no cracking in the second grain on both the side surfaces. The main crack had reached the grain boundary on the other side of the specimen. Post deformation micrographs of both the side surfaces are shown in Figure 6.4 a,b. When viewed along the direction of crack propagation, it became clear that the crack had reached the boundary through most of the thickness, except for the surface being imaged and a little distance into the thickness from this surface. It must be recognized at this juncture that the grain boundaries in our bicrystals curve gently on a macroscopic scale when viewed from the top or bottom, and that the entire crack front may not reach the boundary at the same time. In addition, internal microstructural features like twins could have pinned a small section of the crack front as observed in the case of single crystals. Upon reloading, a crack appeared in the second grain just as in the case of I10A, but only on one side of the specimen where the crack reached the grain boundary. As this side was not being imaged, the exact moment at which the crack appeared is not known. It was identified only upon examination of this surface after the test, and a micrograph illustrating this crack in the second grain is displayed in Figure 6.4a. Despite prolonged loading, the

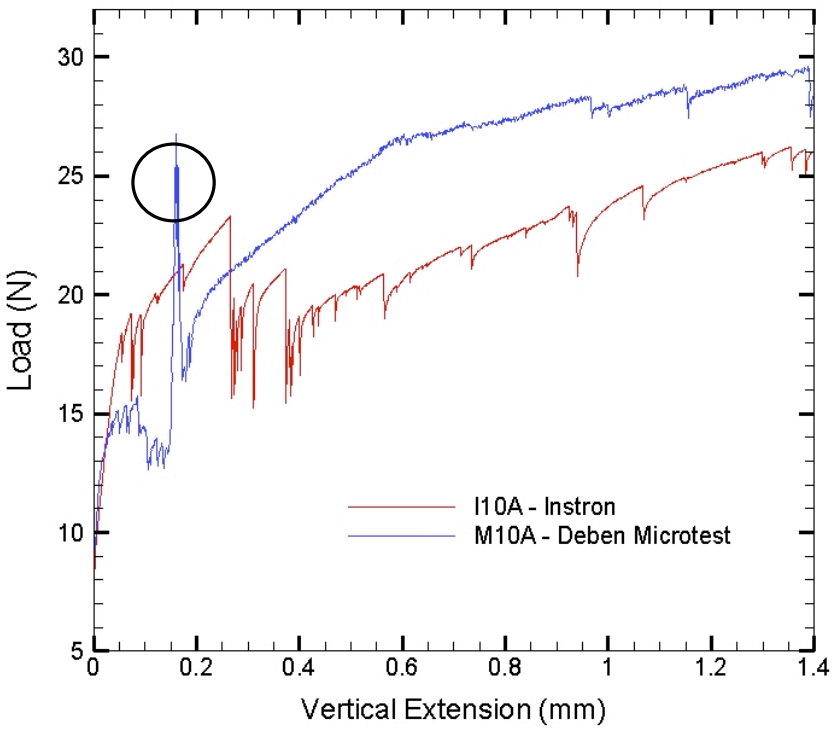

Figure 6.3. Comparison of load-vertical extension curves for 10º twist bicrystals tested using the instron and the microtesting stage. Note the sharp peak in the case of M10A that occurred when the crack reached the grain boundary. In experiments on single crystals (Chapter 5), load-drops such as these were correlated with crack extension through direct *in situ* observations. Not all load drops in these curves could be explained in a similar fashion, but one can conjecture that these may be a consequence of crack extension in the interior regions of the second grain or on the surface not being imaged. The parts of these curves beyond 1.4 mm are not shown here as little information can be gained from them.

crack never reached the boundary on the other side of the specimen and, in the second grain on this surface, cracks were absent (Figure 6.4b). The horizontal line originating from the crack-tip and terminating at the boundary is not a crack but a slip band. Observations at higher magnifications confirm this, but are not shown here, as the out-of-plane displacement between the different regions around the crack-tip sometimes make it difficult to obtain focused images due to the low depth of focus inherent in an optical microscope; further, if this were a crack, given its position with respect to the blunt crack-tip that exhibits a significant degree of crack face separation, it is unlikely that the crack faces in this segment would remain close to one another. Further evidence of such

slip bands will be presented in other bicrystals. The differences between I10A and M10A are possibly due to the difference in the loading configuration, but their behavior is largely similar as discussed above.

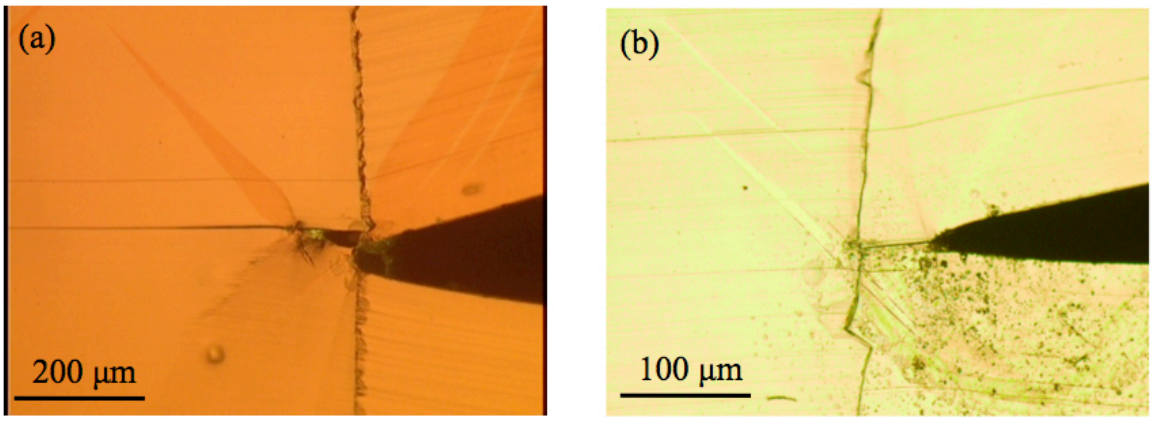

Figure 6.4. Micrographs of M10A after testing. (a) one crack is visible in the second grain (left) and twinning in the first grain (right) in the crack-wake seems to assist in accommodating the applied displacement. Note the faint kink band in the bottom half of the second grain originating from the crack-grain boundary intersection point. (b) Stagnated crack-tip ~60 μm away from the grain boundary on the second side surface. Grain 1 is on the right and grain 2 is shown on the left.

In spite of the large amount of vertical extension (~3.5 mm), the crack in the second grain did not grow beyond the point shown in Figure 6.4a and thus did not result in full fracture of the specimen. The faint kink band in Figure 6.4a occurs at a ~14º angle, very similar to that measured in specimen I10A (Figure 6.2). One can easily contrast this with single crystals where the crack can be propagated at low loads to full fracture without encountering significant resistance in the absence of twins in the crack path. The fracture toughness for this mode of failure, measured by several researchers in the past, amounts to less than 1 MPa$\sqrt{m}$, a value close to that of glass. Therefore, despite such an intrinsically low fracture toughness, bicrystals are able to resist fracture to the point that crack growth is completely contained.

An interesting feature in both the specimens is the serrated appearance of the grain boundary region after testing. There are two kinds of serrations or irregularities in the grain boundary seen in Figures 6.1 and 6.2, and the ones being referred to here are those of the smaller length scale. The large-scale serrations are pre-existing features and are not a consequence of loading. Observations of the grain boundary region prior to and after testing suggest that these features occur in greater intensity only in instances where the crack-tip reached the grain boundary. For instance, in Specimen M10A, this occurred only on one side where serrations can be seen; in contrast, on the side where the crack-tip halted a few microns before the grain boundary, if those serrations are present, they are of a considerably smaller amplitude. This is made clear in Figures 6.5 a,b. Figures 6.6 a,b show the grain boundary region in the crack path on both sides of the specimen before the test, where no noticeable serrations can be seen. The regions shown in Figures 6.5 can be located in Figure 6.6 by locating the same surface aspersions before and after the test. These are encircled in all the figures. In contrast, these features are visible on both sides in specimen I10A (see Figures 6.1 and 6.2), where the crack had reached the boundary on both the side surfaces.

Close examination showed that these features are not indicative of grain boundary separation, but possibly of grain boundary migration. Hence the applied load in both the specimens discussed so far was accommodated by plastic deformation in the form of slip, twinning and kink band formation as well as some amount of grain boundary migration, instead of crack propagation through the grain boundary. Another distinction between the two surfaces in specimen M10A is the absence of a kink band in the second grain on the side where the crack halted a few micrometers away from the boundary. The observ-

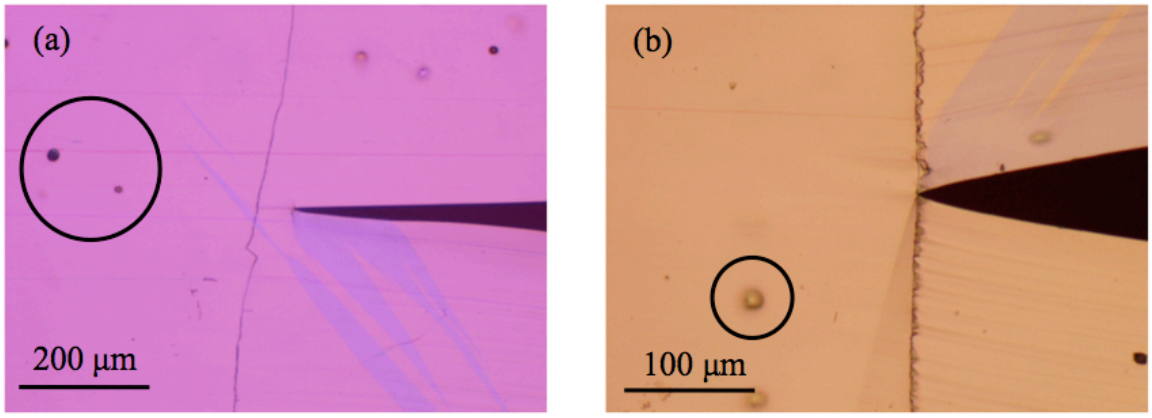

Figure 6.5. Micrographs of M10A after the first loading attempt (a) Crack-tip a slight distance before the grain boundary. (b) the same crack on the other side has reached the boundary. Notice the absence of serrations in (a) and their obvious presence in (b). Grain 1 appears on the right in both (a) and (b), while grain 2 is seen on the left. Some surface aspersions in both the figures are encircled to enable location of the same regions in Figure 6.6.

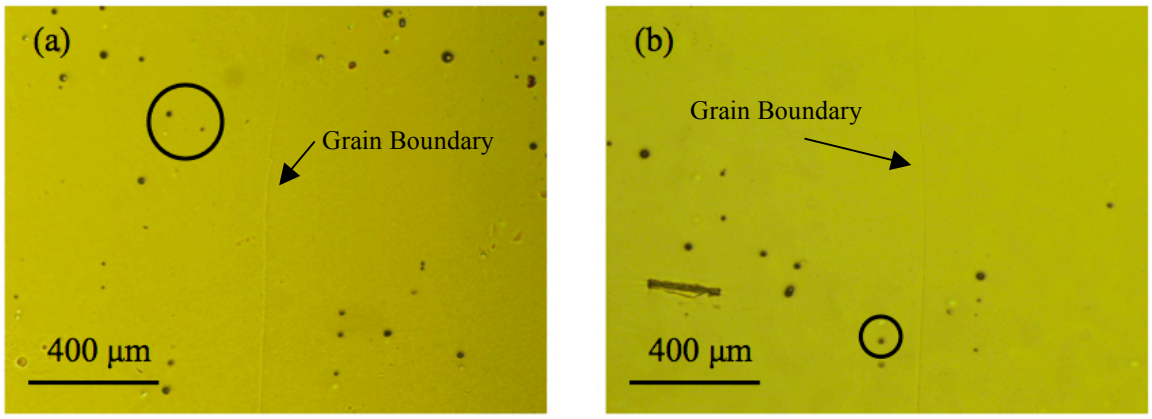

Figure 6.6. (a,b) Low magnification micrographs of the grain boundary region in spciemen M10A (same as Figure 6.5) before testing, showing no serrated features near the grain boundary. Grain 1 is shown on the right and grain 2 is to the left of the grain boundary. Note the enclosed surface aspersions in (a,b) that appear in Figure 6.5 as well.

-ations so far suggest that bending of the cantilever arms to accommodate the constraint at the grain boundary is necessary to produce kink bands in the second grain as well as the aforementioned serrations at the grain boundary. These observations will be with

different twist misorientation are compared and discussed. discussed further in section 6.6, where post-deformation microstructures of bicrystals

6.2 The 20º twist misoriented bicrystals

Two bicrstals of 20º twist misorientation, M20A and M20B, were tested using the same method used for M10A. At the beginning of the test, in both the specimens, there were two closely spaced parallel cracks originating from the notch. In such cases, as discussed at length in Chapter 5, the initial load is increased due to ligament deformation and planar crack propagation will not occur until the ligament ruptures. This happened naturally during the test in specimen M20A, but had to be accomplished by cutting off the ligament in specimen M20B manually by using a razor blade. But once the crack becomes planar, the initial ligament ceases to be of any consequence and the results can be properly interpreted.

The observations were similar to M10A in that the crack halted at the grain boundary, after which a kink band was seen near the grain boundary in the second grain as the cantilever arms deformed plastically. A peak in the load-extension curve was observed as well, and the average load following the peak was ~125 N, significantly higher than that observed in the 10º bicrystals (~30 N). The grain boundary progressively began to develop serrations in response to continued loading just as in the 10º bicrystals. From Figures 6.7a,b, the first immediately after the crack encountered the grain boundary, and the second several minutes later, it becomes clear that serrations in the grain boundary arise due to prolonged loading after the crack-tip reaches the grain boundary. In Figure 6.7b, the other features associated with crack-grain boundary

interaction such as twinning and kinking in the second grain are also seen. The kink band in this case is observed at a 24º angle to the grain boundary. Then a crack appeared on the

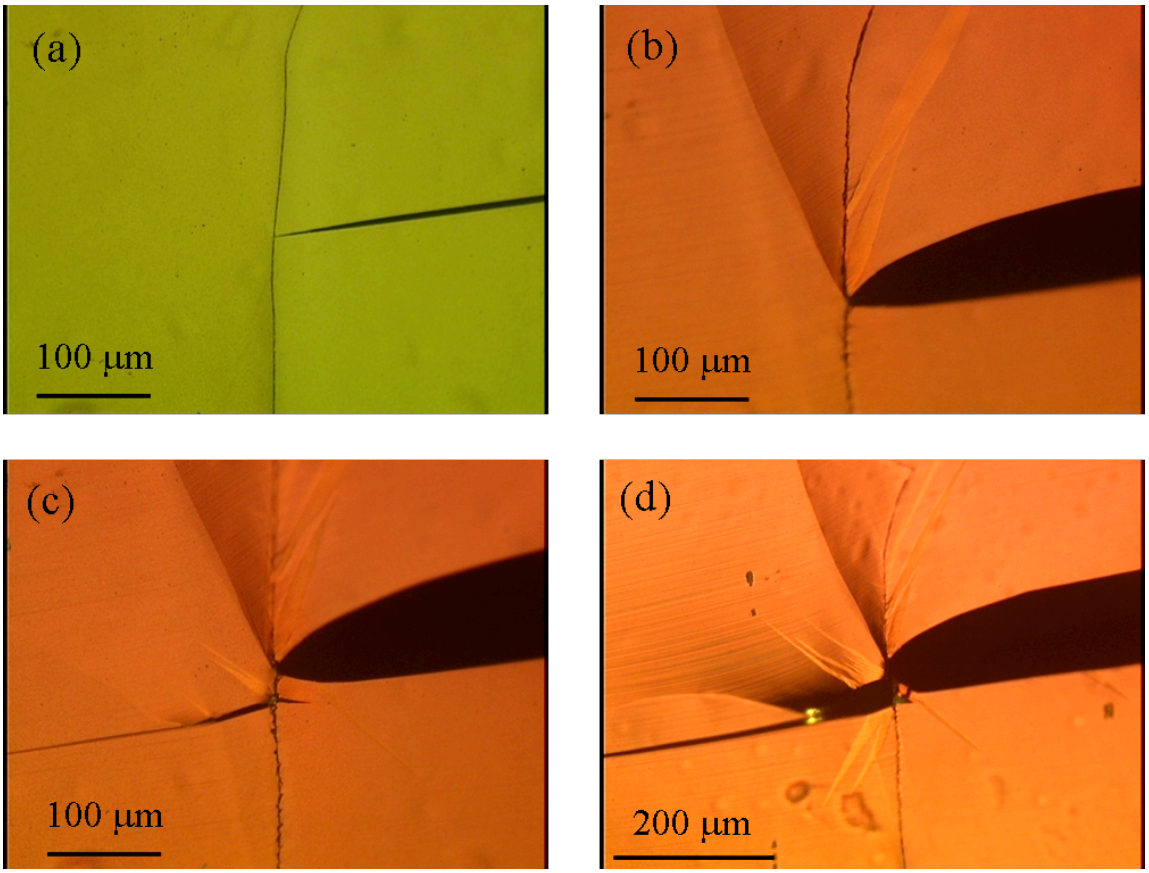

Figure 6.7. Progression of images extracted from an in situ test on a 20º bicrystal (M20A). (a) Crack arrives at the grain boundary. (b) Prolonged loading causes the crack blunting, twinning in the crack-wake and kinking in the second grain. (c) A new crack appears in the second grain while a short crack runs backwards into the first grain. Twinning can be seen in the second grain originating from the crack. (d) Further loading causes the cracks in the fist and the second grains to connect.

surface in the second grain near the grain boundary, a moment fortunately captured on video. Figure 6.7c shows a still image of a newly formed crack on the surface. At the same time, a short crack ran backwards in the first grain from the grain boundary, while narrow twins appeared in the vicinity of the crack in the second grain. Prolonged loading after this point caused the region between the cracks in the first and second grain to

deform and finally rupture near the surface as seen in Figure 6.7d. Due to the twist angle between the cracks, the depth to which this rupture occurred could not be estimated from this observation. During this period, further cracking occurred in the second grain. On the surface being imaged *in situ*, a total of three cracks, marked A, B and C were noted (see Figure 6.8), two of which (A and C) extended by a distance of 2 mm, whereas one of them (B) grew to less than 1 mm. Extensive twinning was observed in the material between the first two cracks, originating at crack A and growing toward crack C (see Figure 6.8). Twin growth in all cases consisted of the nucleation of a narrow twin band that elongates and grows wider in response to further loading. The size of the twins varied substantially. The cracks in the second grain were a few hundred micrometers apart from one another when measured on the surface. When the crosshead displacement reached 5 mm, at which point cracks began to form near the gripped region in the first grain, the test was discontinued. Upon microscopic examination, the second surface revealed two parallel cracks (we refer to these two cracks as D and E; these are discussed in the next paragraph) in the second grain, one of which connected with the main crack in the first grain. One of these cracks grew by a remarkable 6 mm length, while the other was confined to 2 mm as the other cracks seen on the first surface. Due to the large opening between the crack faces and the extensive deformation of the ligaments between the cracks, micrographs of this region were difficult to obtain and contained little useful information. However, all the features observed on the first surface were also present here, only to a much greater degree.

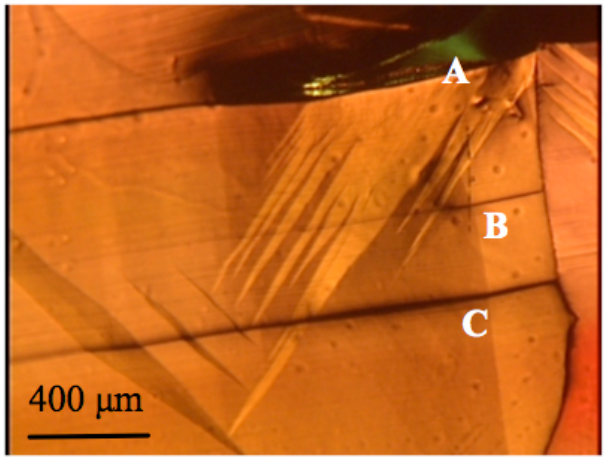

Figure 6.8. Multiple cracking in the scond grain seen at low magnification. Twins originating from the first crack in the second grain have grown in width and length.

When the grain boundary plane was viewed through the opening in the first grain, multiple diamond-shaped cracks in the second grain were observed as seen in Figure 6.9. Cracks A, B, C, D and E, which were observed on the side surfaces, are visible and marked in this Figure 6.9. In addition, we find an internal crack roughly mid-way through the thickness, termed F that showed no corresponding opening on either surface. Though these cracks seem to have grown only to a length of less than 1 mm laterally (measured along the grain boundary plane) on the plane of the grain boundary itself, they extend to greater lengths as we move away from the grain boundary. For instance, cracks B and C may give the mistaken impression of being tunnel-like cracks through the second grain, but are visible on the sides of the specimen. Though the crack front in these cases is pinned at the grain boundary, observations from the side surfaces show that the cracks reached the grain boundary (see Figure 6.8). This indicates that the pinning effect is confined to a length smaller than the maximum resolution of the microscope and that the front can extend all the way to the closer surface to be observed. Possible crack fronts of internally nucleated cracks B and F are schematically illustrated in Figure 6.10.

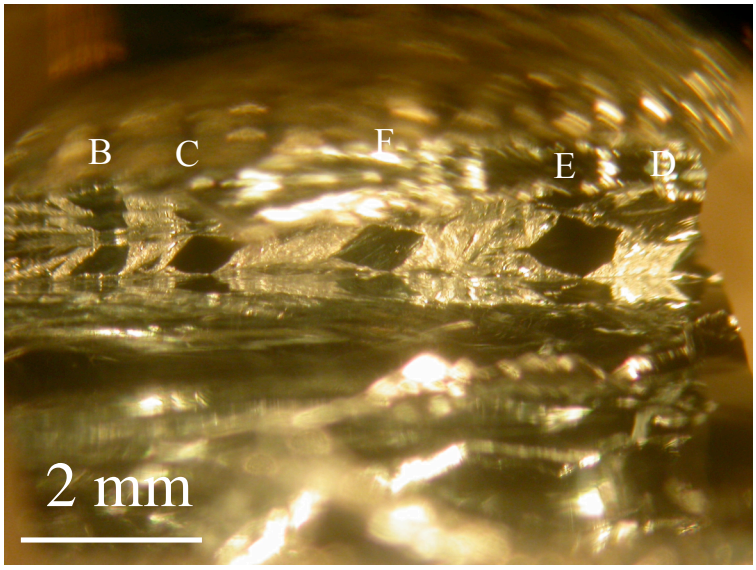

Figure 6.9. Photograph of the grain boundary plane viewed through the crack opening in the first grain. Note the diamond shaped cracks in the second grain on the basal planes.

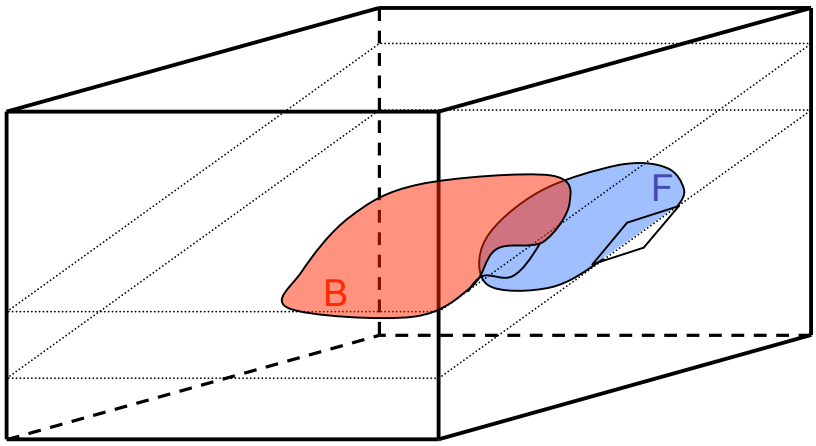

Figure 6.10. Schematic illustration of the possible crack fronts corresponding to cracks B and F.

The case of specimen M20B is quite different. There were two pre-cracks on one side of the specimen, while only one was seen on the other side. The side containing the two precracks was imaged during the initial stages of the test. Upon loading, the pre-crack visible on both sides dominated crack extension, but some growth in the other pre-crack was also observed. As a consequence, a ligament of thickness ~0.1 mm was

present between two cracks on one side of the specimen, providing some shielding to the crack-tip. Even after the longer crack had reached the boundary, the ligament was still intact and was experiencing progressive deformation as seen in Figure 6.11.

The sample was unloaded in order to examine the other side, where the crack was came to a halt a few microns from the grain boundary in much the same way as it did in the case of specimen M10A. After another attempt at loading the sample, ligament

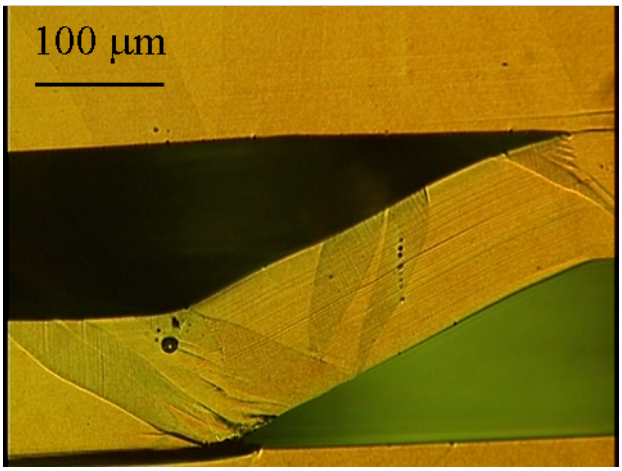

Figure 6.11. Ligament bridging two parallel basal cracks in the first grain that was later cut off by using a razor blade. Crack propagation direction is from right to left.

rupture could not be achieved, at which point a razor blade was used to gently cut off the ligament to create a macroscopically planar crack. Further loading did not result in macroscopic cracks in the second grain as observed in Specimen M20A, though the sample sustained similar load levels, reaching 170 N on one occasion, following which the glue experienced partial failure. The test was discontinued once basal cracks

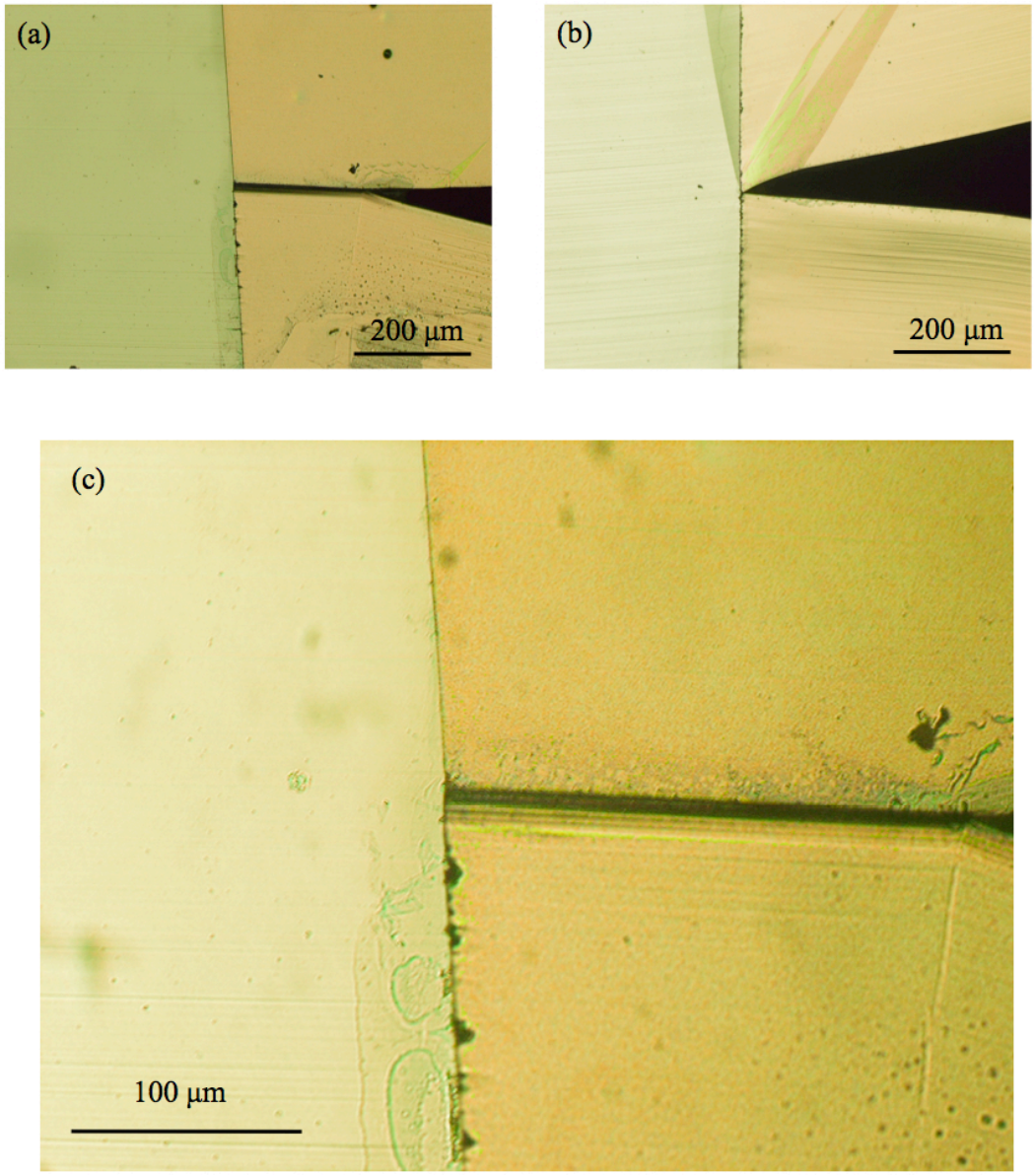

Figure 6.12. Grain boundary region after testing in M20B, a 20º twist bicrystal (a) Staganant crack-tip ~ 200 µm away from the grain boundary from which a slip band and a kink band originated. (b) Crack-tip at the grain boundary on the other side of the same specimen where a twin in the first grain and a kink band in the second grain are visible. (c) Magnified view of the slip band in (a) In all the micrographs, grain 1 is on the right and grain 2 appears on the left.

in the first grain were observed in the region near the grips. The crack-grain boundary intersection region on both side surfaces is shown in Figures 6.12a,b, where it is clear that the crack had reached the boundary and begun interacting with it on one side (Figure 6.12b). This micrograph (Figure 6.12b) bears resemblance to Figure 6.7b obtained from

Specimen M20A, but with a kink band at 12º to the grain boundary (similar to what was observed in the 10º bicrystals). On the other side (Figure 6.12a and a higher magnification image in Figure 6.12c), there is a slip band originating from the crack-tip and ending at the boundary. An interesting feature to note in Figure 6.12c is a kink band originating from the crack-tip in the bottom half of the crystal. The kink band is made visible by the abrupt change of direction of the basal slip traces in the first grain. The difference between this kink band and the other ones previously discussed is that there is no discontinuity in out of plane displacement across the kink boundary as evidenced by the lack of color contrast in the polarized light micrographs. This implies that the displacement discontinuity across this kink boundary is restricted to the plane of the side surface. In contrast to the features observed on the first surface, we see a twin originating from the crack-tip into the first grain on the other side, where the crack had reached the boundary (Figure 6.12b). Another difference between the two side surfaces is the absence of a kink band in the second grain. It is not clear if the initial ligament played a role in causing the crack to halt several micrometers before the boundary.

The load-extension curves for Specimens M20A and M20B are shown in Figure 6.13. In M20A, during crack propagation in the first grain, the load remains fairly low, comparable to that of single crystals as well as the 10º bicrystals. But once the crack reaches the grain boundary, an event easily documented during the *in situ* test, the load begins to rise sharply. There is a sudden drop following which the load remains steady with occasional load-drops, but at levels much higher than those observed in the 10º bicrystals. The load drops seen during this period presumably correspond to crack extension either in the second grain or in the first grain near the grips or both, but as none

of these events were recorded during the test, it is not possible to correlate them to any specific event. The curve for specimen M20B shown here is for the segments of the test after the crack reached the boundary, and the loops in the curve correspond to the interruptions in the test that were necessary for a full microscopic examination of the specimen. The slope of the curve compares well with that of Specimen M20A during the

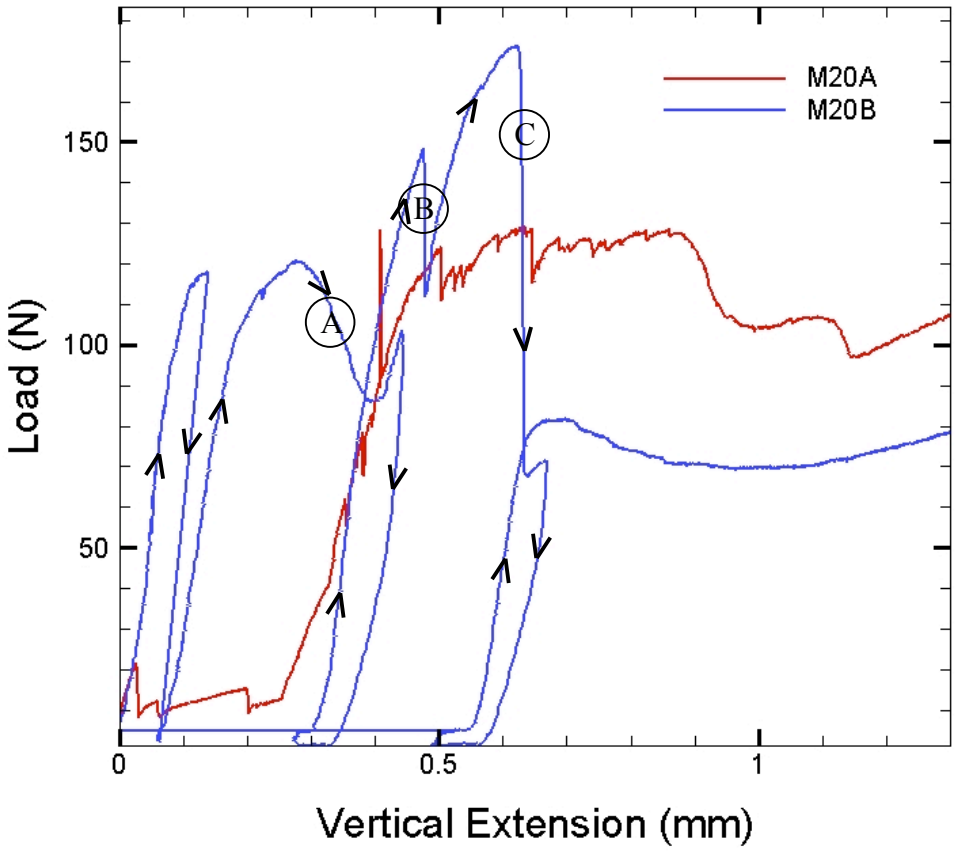

Figure 6.13. Load vs vertical extension curves for the two 20º twist bicrystals, M20A and M20B. Both specimens sustained similar loads, much higher than those encountered in the 10º bicrystals.

initial period of crack-grain boundary interaction. The periods of decline in load not caused by unloading are marked A, B and C in Figure 6.13; the first one is thought to be a consequence of crack growth in the ligament, while the other two may be due to cracking in the first grain near the grips. It is important to note here that despite the

absence of cracking in the second grain, this specimen sustained loads comparable to that of M20A; this suggests that the average remote load is controlled by resistance to plastic deformation rather than fracture.

6.3 The 30º twist misoriented bicrystals

Three bicrystals of 30º twist angles namely, I30A, I30B and M30A were tested during the course of this study, the first two of which were tested using the Instron as the nomenclature suggests. These two tests were conducted before the microtesting stage was employed and form the basis for grip and specimen design for later samples. In all the samples, there were two competing cracks originating at the notch, which posed problems as in the case of M20B. In the case of specimen I30A, there were two pre-cracks, one on each side, and were separated by a distance roughly equal to the diameter of the notch. Due to the shielding effect caused by this ligament, the cracks on either side did not grow to the grain boundary, and the test was discontinued. It was in this specimen that the significant toughening effect of ligaments was observed which was later confirmed by conducting tests in single crystals (Chapter 5).

The same specimen was used again by increasing the length of the notch to eliminate the previous cracks and to create a fresh pre-crack. As the arms of the first grain were deformed significantly during the test, they were bent back by gripping the specimen in a small vice. Since the arms near the gripped region were significantly deformed at the end of the test, these regions were removed by cutting them, effectively making the specimen shorter by ~3 mm. This process also ensures a decrease in compliance so excessive bending in the arms can be avoided. After preparation, two pre-

cracks were found at the end of the notch, one on each side as before; but upon loading, both of them grew to the grain boundary despite the ligament. However, prolonged loading did not cause ligament rupture, and both the crack tips were allowed to interact with the grain boundary throughout the test. All the hallmarks of crack-grain boundary interaction such as twinning in the first grain, kink band formation, slip and grain boundary serrations, were observed. Micrographs of the specimen after testing are displayed in Figure 6.14. But no evidence of cracks was found in the second grain despite the large amount (~3mm) of vertical extension.

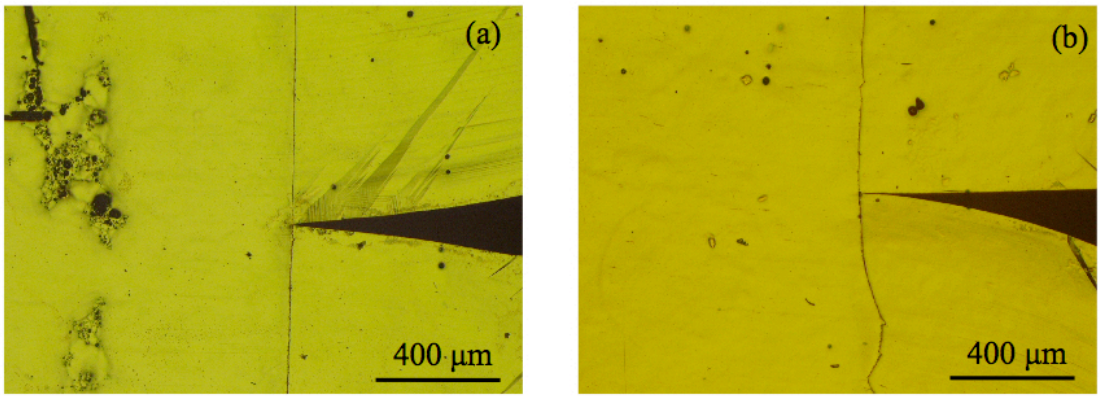

Figure 6.14. Grain boundary region after testing in I30A, a 30º twist bicrystal. The main crack in the first grain reached the grain boundary on both sides of the specimen, but no cracks in the second grain were visible on the surfaces.

The information gained from this specimen was used to make slight modifications in the grips to test the next 30º specimen, I30B. The gripping length was increased to 7.5 mm to make the arms behave in a stiffer manner so that cracking in the second grain can be favored over plastic bending of the cantilever arms. Upon loading, crack propagation occurred suddenly in grain 1 and the crack on one side surface grew long enough to meet the boundary. However, there were two cracks on the other side surface, spaced by ~ 70

μm as seen in Figure 6.15, which prevented both of them from reaching the grain boundary, much like what was seen in the other samples. So, the test was discontinued as

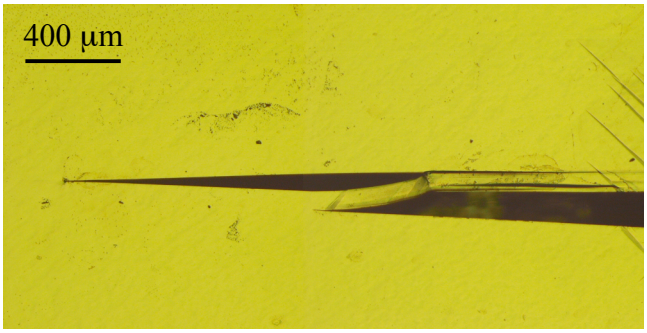

Figure 6.15. Microscopic ligament between parallel basal cracks in the first grain in I30B, a 30º twist bicrystal. Shear deformation of the bridging ligament caused the crack to arrest and not reach the grain boundary. The test was abandoned as a result.

it became clear that in the event the ligament cannot be cut manually, it is very unlikely that crack propagation would resume. In fact, the observations from these two specimens, I30A and I30B, led to experiments on single crystals specimens with macroscopic crack ligaments, already described in detail in Chapter 5, where it was found beyond doubt that ligaments can significantly enhance the toughness even in single crystals despite the low fracture toughness.

Specimen M30A was the third 30º bicrystal to be tested. The initial response of the specimen was similar to that of I30B in that a ligament extending through a third of the thickness from one side halted the crack on one side of the specimen, while allowing it grow very close to the grain boundary on the other side. The test was stopped after an extension of ~1.5 mm and a steel wire was used to cut the ligament which resulted in a single through-thickness crack. Upon reloading, the crack came very close to the grain boundary on both sides and the specimen was successfully loaded to a total of ~4.4 mm

extension that includes two loading attempts. Figures 6.16a,b show the crack-tip on both the surfaces, where it is apparent that the distance between the crack-tip and the grain boundary is smaller on one side than the other. Though the crack had not arrived at the boundary, serrations of the type seen before are evident on both side surfaces. This appears to contradict earlier observations where serrations did not appear when the crack stalled before reaching the boundary; on the other hand, it could simply be an artifact of the grain boundary curvature (with respect to the vertical) as the crack front may have reached the grain boundary in the immediate interior. Basal slip can be seen in both the grains in significant quantities. There are kink bands originating from the crack-tip on

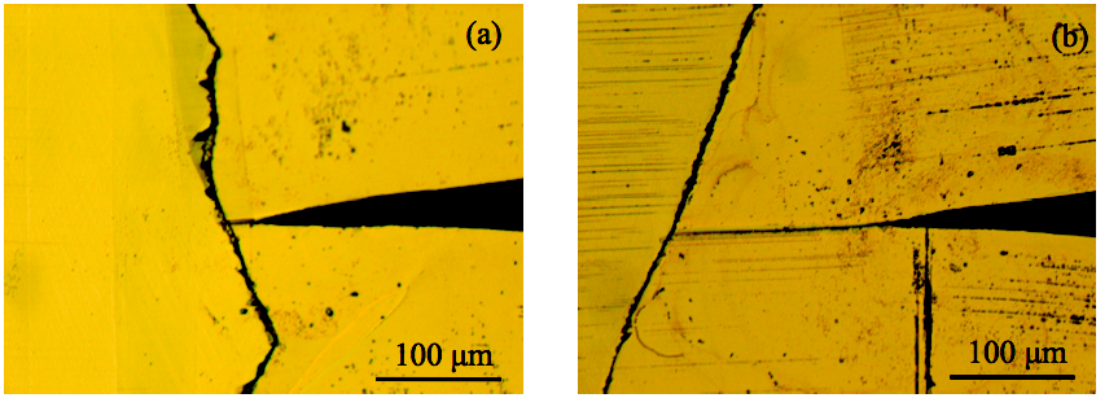

Figure 6.16. Post-test micrographs of specimen M30A. (a) Main crack in the first grain is ~20 μm away from the grain boundary, and a very faint kink band can be seen originating from the tip above the crack plane. Also, another faint kink band is observed in the second grain. (b) The crack-tip on the other side of the specimen halted more than 100 μm before the grain boundary and a corresponding kink band is evident above the crack plane. Note the clear discontinuity in the basal slip traces.

both surfaces and twins are clearly absent. A dark slip band, which could be mistaken for a crack, runs from the crack-tip to the grain boundary, similar to what was observed in specimen M20B. In contrast to what is seen in M30A, twins were observed in the first grain in specimen I30A, where the crack had evidently reached the grain boundary; but

kink bands were absent. Again, no crack transmission past the grain boundary was seen in this case, and it became apparent that 30º is large enough in terms of misorientation to prevent cracking in the second grain.

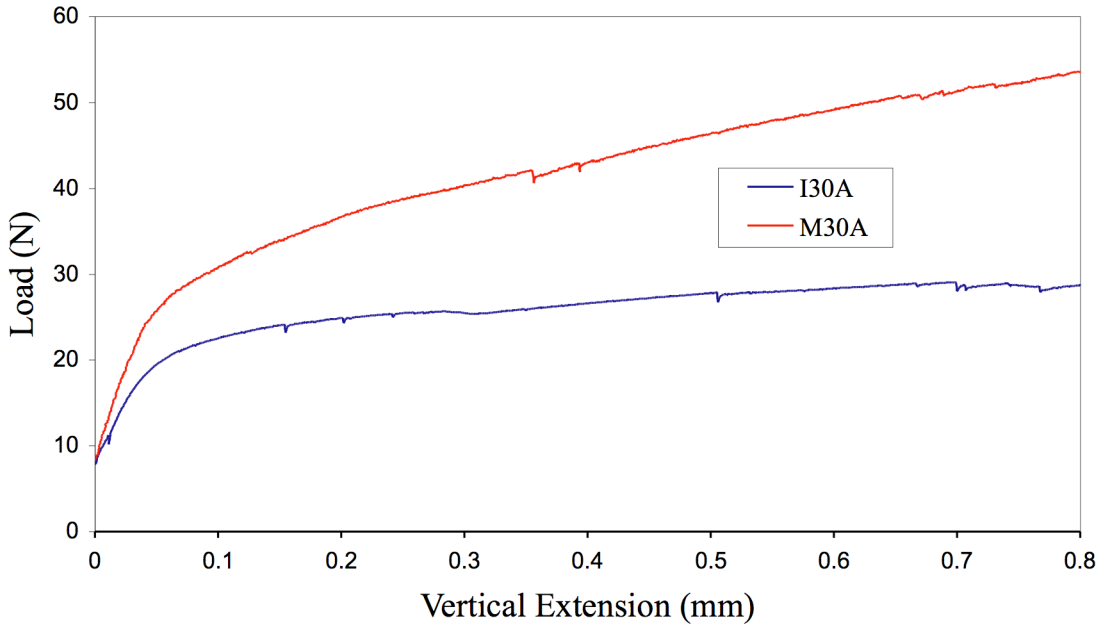

Figure 6.17. Load-vertical extension curves for two 30º twist angle specimens, I30A and M30A.

A comparison of load-extension curves for I30A and M30A are shown in Figure 6.17. The comparison is reminiscent of Figure 6.3, where M10A and I10A were compared, and shows the stiffer response of the specimen when the rotation of the cantilever arms is significantly restricted. The data plotted in the curve for M30A is after the ligament was completely removed, and therefore reflects crack-grain boundary interaction from zero vertical extension, if we recall that the crack had reached the grain boundary on one side before the specimen was loaded a second time.

Even though it appears that the ligaments could have been responsible in preventing cracking in the second grain, one must note that in all the cases, the ligaments extended only part way through the crystal from one side surface, while the crack reached the grain boundary fairly early in the test. The fact that no cracks were found in the second grain on the side where the crack reached the grain boundary clearly suggests that the twist angle is responsible for the lack of crack transmission.

6.4 The 45º twist misoriented bicrystal

One specimen of 45º twist misorientation, M45A, was tested using the microtesting stage. Fortunately, there were no ligaments preventing the crack in the first grain from propagating to the grain boundary, and the sample was loaded continuously to an extension of ~6 mm. Just as in the 30º specimens, no cracks were observed in the second grain. Micrographs of the grain boundary region after the test are displayed in Figure 6.18.

The dark region in Figure 6.18a next to the grain boundary is a kink band and not a grain boundary crack. It appears dark in the polarized light micrograph due to its high inclination with respect to the rest of the surface. There is another kink band visible in Figure 6.18a of lesser inclination a slight distance away from the main kink band. The kink band on the other surface (see Figure 6.18b) appears much like those observed in the other specimens, in both its location and appearance. The density of slip traces in the second grain indicates a much larger degree of plastic deformation than that observed in specimens with smaller twist angles. Therefore, it appears that a 45º angle with respect to the crack plane is highly favorable for basal slip. The ease of plastic deformation in the

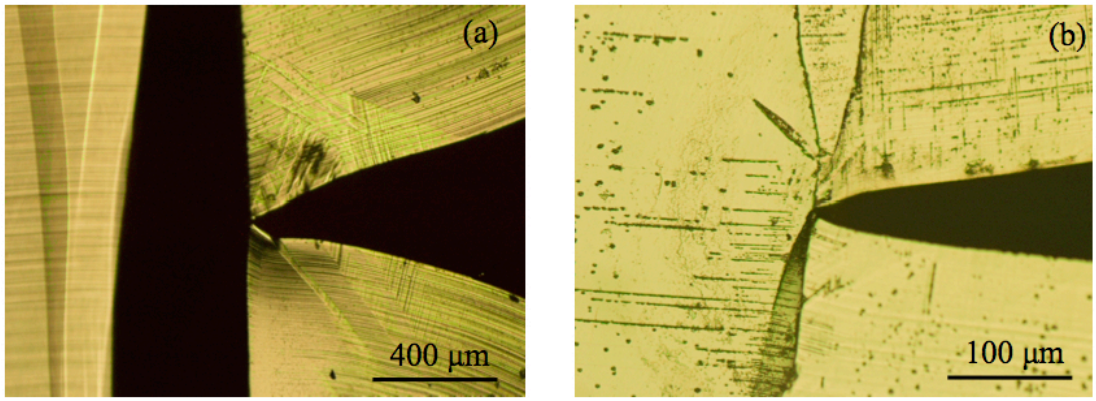

Figure 6.18. Post-test micrographs of specimen M45A. Crack-tip is in contact with the grain boundary on both sides and no cracking in the second grain was observed. (a) On the first side, a large kink band on both sides of the crack plane is visible in the second grain, which is accompanied by other less intense bands. (b) Only one kink band below the crack plane is visible in the second grain.

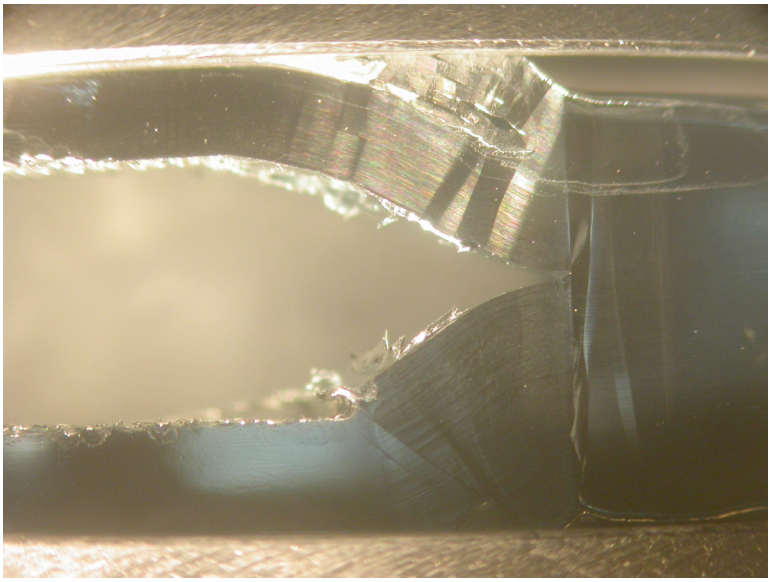

Figure 6.19. Low magnification micrograph showing the final configuration of the 45º twist bicrystal, M45A, after testing. There is extensive plastic bending of the cantilever arms in the first grain by large amounts of slip and kinking.

second grain is an important deterrent to fracture, as it would serve as a competing mechanism of accommodation.

As the test was not hampered by shear ligaments in the first grain, it is quite clear that the high twist angle is responsible for preventing fracture in the second grain. The

final configuration of the specimen is shown in Figure 6.19. The bending of the cantilever arms, extensive amount of slip in the first grain and a kink band in the second grain can be clearly seen in the photograph.

6.5 SEM observations of the grain boundary plane

During and after testing, in most cases, only surface observations have been presented and discussed. Due to the formation of large cracks and a large opening in the first grain (due to crack-pinning at the grain boundary and bending of the cantilever arms), the grain boundary plane in specimen M20A became accessible for observation, and one such view was shown and discussed earlier in section 6.2. Internal cracks and their geometry could be clearly documented as a consequence. This was not the case in the other specimens. To permit such observations, the cantilever arms were cut off using a low speed diamond saw without affecting the grain boundary region in four of the specimens, M10A, M20B, M30A and M45A. This allowed the probing of the grain boundary plane where the crack in the first grain interacts with it and the resulting observations made with the aid of a scanning electron microscope are presented below.

A view through the crack opening in the first grain in specimen M10B is shown in Figure 6.20, in which two basal cracks in the second grain can be discerned. The larger of the two is the same as that seen on the surface in Figure 6.4a. The smaller crack, magnified in 6.20b, was not visible on the surface and thus is an internal crack. From these views, it is possible to estimate the radius of the tip of the main crack at the grain boundary. The appearance of the grain boundary plane is distinctly different from that of the crack faces: the crack faces have a smooth appearance as they were produced as a

consequence of basal cleavage; the grain boundary plane, on the other hand, appears rough. The distance between the edges of the smooth surfaces should approximately equal the diameter of the crack-tip, if it were assumed to be semi-circular. From Figure 6.20, in the region being imaged, this radius is ~18 μm.

The entire specimen thickness (along the crack front) was probed in this manner for both internal cracks as well as information about the degree of blunting at the crack-tip. Figure 6.21 shows an internal region, beyond the halfway point along the thickness from the region shown in Figure 6.20. No internal cracks are visible here, but the crack-tip radius appears to be ~ 1 μm. This indicates an asymmetry in deformation of the cantilever arms, that perhaps develops as a consequence of crack formation and growth in the second grain that is biased to one side (cracks in the second grain were observed only on one side in specimen M10B). A closer examination of Figure 6.9, where a complete view of the crack front in the grain boundary plane in specimen M20A is shown, reveals a similar asymmetry.

Another interesting observation is the appearance of the grain boundary plane in Figures 6.20 and 6.21: they both display surface irregularities of an unknown nature that may be related to the serrated appearance of the grain boundaries seen on the side surfaces in most of the specimens after testing.

After cutting the cantilever arms in specimen M20B, it became clear that approximately half the length of the crack front in the first grain had not reached the boundary. The exposed grain boundary region revealed some damage in isolated locations, but no crystallographic cleavage or crack transmission through the grain boundary as in the case of M10B. The case with M30A is somewhat similar in that no

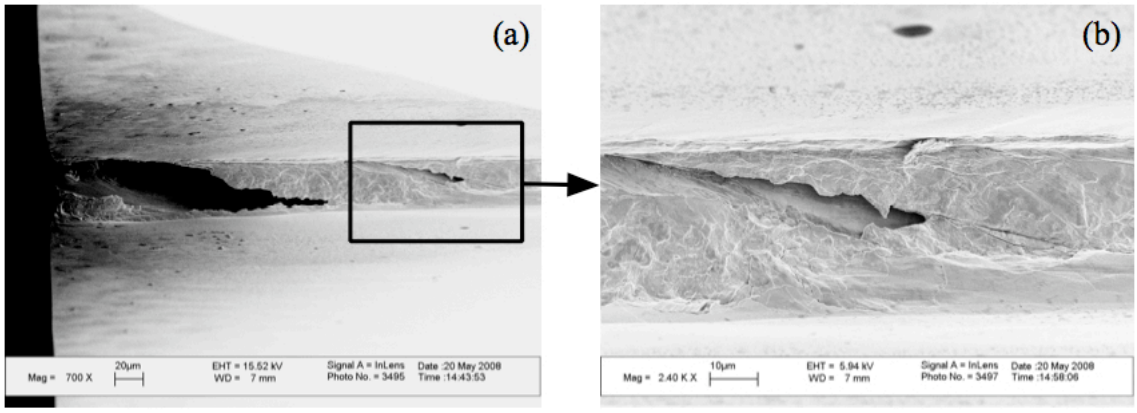

Figure 6.20. (a) Scanning electron micrograph of the grain boundary plane in specimen M10B viewed through the crack opening in the first grain. Note two parallel cleavage cracks in the second grain. (b) Magnified view of the inset in (a).

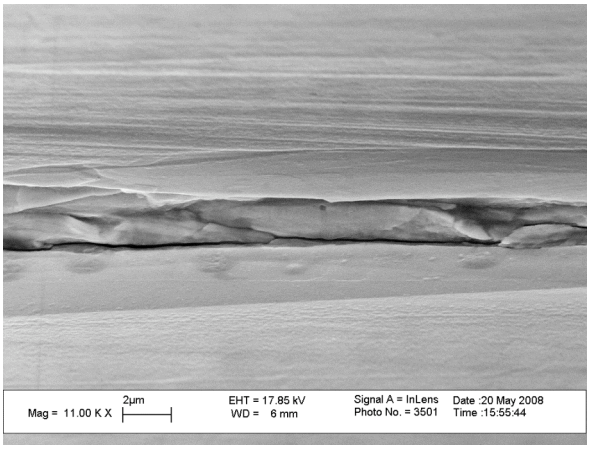

Figure 6.21. Scanning electron micrograph of the grain boundary plane in specimen M10B.

cleavage in the second grain was observed. Figures 6.22 and 6.23 show grain boundary damage in specimens M20B and M30A respectively.

In specimen M45A, a microscopic crack (~ 15 μm across) in the second grain was observed in the interior of the specimen (see Figure 6.24). The geometry appears quite similar to those seen in specimen M20A (see Figure 6.9), which were of a much larger length scale. There was no further evidence of such cracks in the rest of the specimen.

The surface irregularities observed in specimen M10B are much more prominently seen in this micrograph.

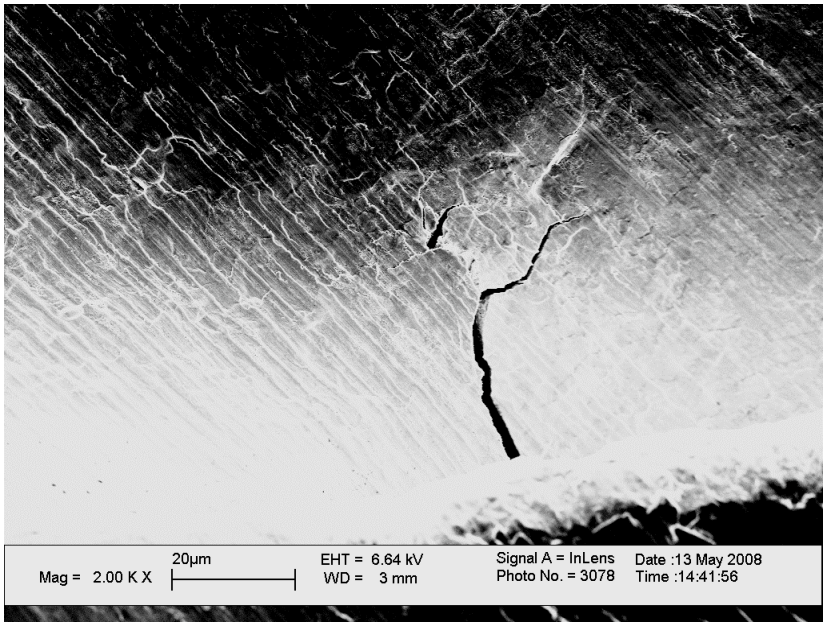

Figure 6.22. Grain boundary damage ahead of the crack-tip in the first grain in specimen M20B.

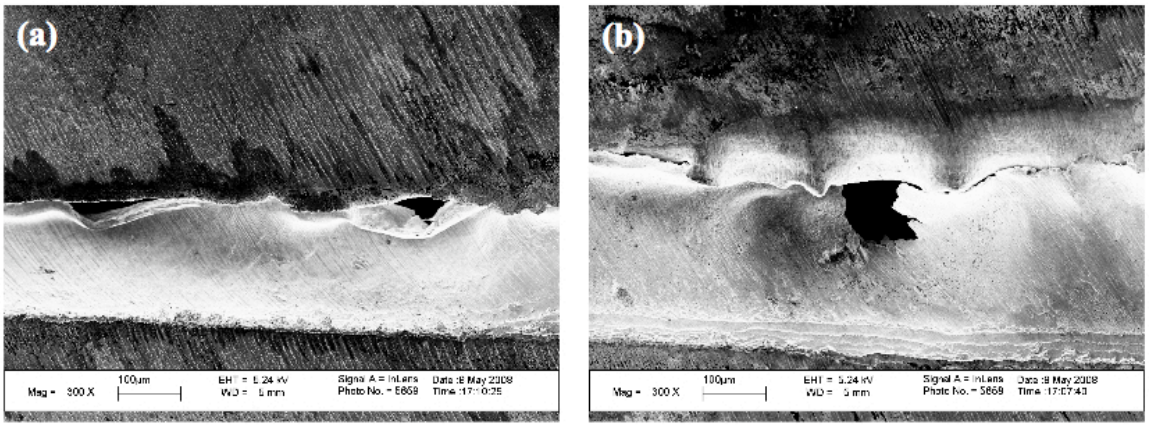

Figure 6.23. Scanning electron micrographs of the grain boundary region in specimen M30A showing damage of a non-crystallographic nature ahead of the crack-tip in the first grain in specimen M20B.

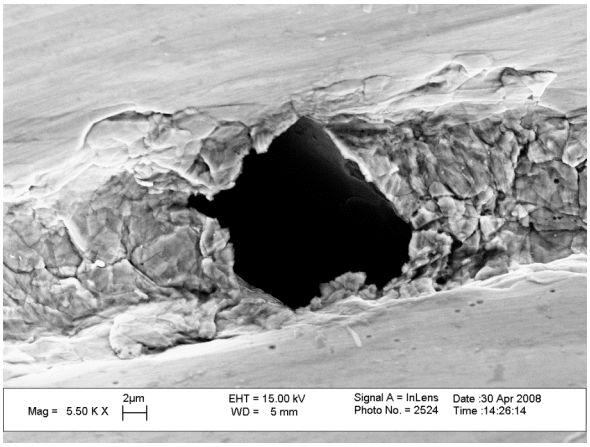

Figure 6.24. A microscopic diamond shaped crack in the second grain in M45A.

6.6 Discussion of microstructural features

6.6.1 Twinning and kink band formation

In the absence of cracking in the second grain, several possible mechanisms other than slip were documented that accommodate the imposed vertical extension namely, twinning in the crack-wake in the first grain, kink-band formation in the second grain, kink-band formation in the first grain with no kink bands in the second grain etc. Kink bands in the second grain are characterized by an out of plane displacement and a sharp discontinuity in basal slip traces, while those that occur in the first grain only have a discontinuity in the basal slip traces with no discernable out of plane displacement. In addition, the kink bands in the second grain make a 12-14º angle with the grain boundary in all the cases except in specimen M20A, where the angle was 24º. We shall return to this observation in Chapter 7.

Since kink band formation seems to involve only basal slip, the in-plane orientation of the basal plane in either grain is of little consequence, for the critical resolved shear stress for basal slip is only 0.3 MPa. However, if twinning in the crack-

wake is to accommodate the imposed vertical extension, then the in-plane orientation of the basal plane in the first grain becomes an important parameter, if we recall from Chapter 5 that twinning in the crack-wake is more likely if the crack propagation direction is <10-10>. If the crack reaches the boundary, then the evidence gathered so far suggests that twinning in the crack-wake and kink band formation in the second grain are likely the only operating mechanisms if cracking in the second grain does not occur. However, the case when the crack halts some distance away from the crack tip is different. For instance, in the 10º specimen M10A, twinning was observed in the crack-wake (Figure 6.1b); in contrast, kink bands were observed in the first grain in specimens M20B and M30A. The kink bands seen in the first grain originating from the crack-tip do not need an out-of-plane component of displacement and can produce lattice rotation, just as a twin would, and lattice rotation is an effective way of accommodating the applied vertical extension. The selection of one accommodation mechanism over the other is explained by the fact that in specimen M10A, the crack growth direction in the first grain is <10-10>, whereas M20B and M30A have the primary crack growing along a <11-20> direction. As twinning is less favored, if not impossible in this case, the imposed deformation is accommodated by the formation of a kink band.

6.6.2 Grain boundary serrations

It has been hinted earlier (section 6.1) based on low magnification optical micrographs that the serrations observed in the grain boundary region after testing are indicative of strain induced grain boundary migration. Here we explore this issue further by probing the grain boundary region with a scanning electron microscope that is capable

of much higher magnifications. The bending of the cantilever arms is produced by dislocation motion in substantial amounts towards the grain boundary; given the discontinuity in deformation at the boundary, the question arises as to how the displacement produced by such a large number of dislocations is accommodated.

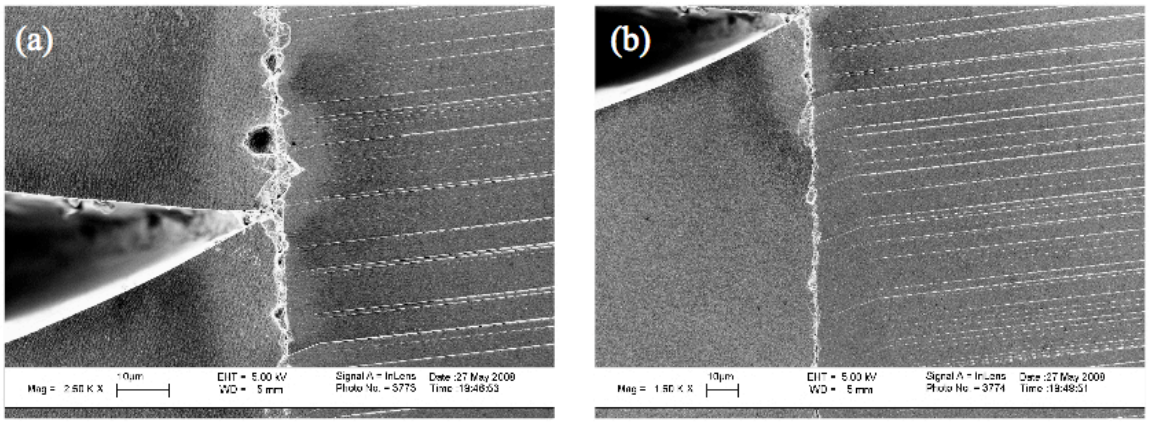

Figure 6.25. (a) Scanning electron micrograph of crack grain boundary intersection in specimen M20B. (b) Region near the grain boundary below the main crack plane showing a kink band. Grain 1 and grain 2 are on the left and right of the grain boundary respectively.

The crack-grain boundary intersection region in specimen M20B is shown in Figure 6.25a, and a region below the crack plane is displayed in Figure 6.25b, where a kink band is also visible (note that the first grain is on the left and the second is seen on the right). The serrated appearance of the grain boundary is clearly seen in these figures. Interestingly, slip traces are visible in the second grain, but not in the first, though we know from optical microscopy that they occur in similar numbers in the first grain. The reason for this discrepancy is that slip traces in the second grain are visible because of charge accumulation on the terraces produced by slip with an out of plane displacement. In the first grain, however, the effective out of plane displacement is much lower (see Chapter 5) because of the orientation.

Figure 6.26 shows images of the grain boundary at higher magnifications where grain boundary migration can be clearly seen. The accumulation of charge in the region of interest indicates vertical undulations on the surface that are perhaps caused by extensive displacement of material as a consequence of slip in both the grains. Similar features were observed in all the bicrystals and the images shown here are therefore representative of the interaction of a basal crack with a grain boundary of twist misorientation.

The flow of dislocations in the first grain to the grain boundary can be visualized quite easily. Similar motion of dislocations in grain 2 is different. Slip typically occurs by dislocation loops extending outward and reaching a free surface if available, and slip steps are produced on the surfaces as a consequence. These steps are visible in the second grain on the side surfaces as previously shown and discussed. An examination the back faces also showed similar slip traces. An optical micrograph of specimen M20A is shown in Figure 6.27, where slip traces on the back face are clearly visible. The consequence of dislocation motion on the free surfaces is obvious, but not so on the grain boundary plane, though it can be said that displacements of similar magnitudes as those observed on the free surfaces must be accommodated at the boundary as dislocation loops expand in all directions. It is possible that boundary migration and the surface undulations are a direct consequence of extensive dislocation motion.

6.7 Comparison of load-extension curves

The load vs extension curves from specimens M10A, M20A, M30A and M45A are all compared in Figure 6.28. It is worthwhile to point out here that the specimens

were not of identical dimensions in that the thickness and the height varied by about 0.5 mm. These small variations are not expected to cause significant changes in the load displacement behavior as we shall see shortly. All the specimens except for M30A had a

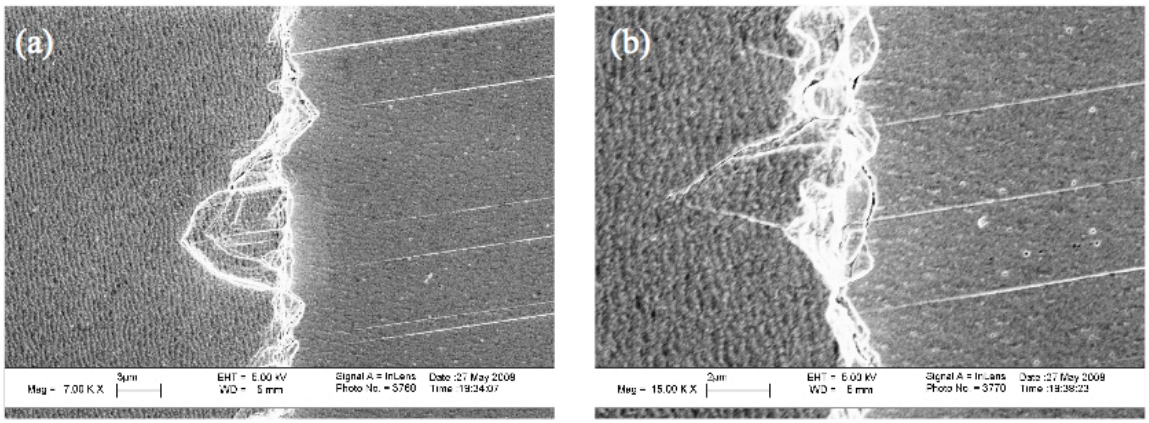

Figure 6.26. (a,b) Scanning electron micrograph of the grain boundary region in specimen M20B after testing showing grain boundary migration. Grain 1 and grain 2 are on the left and right of the grain boundary respectively.

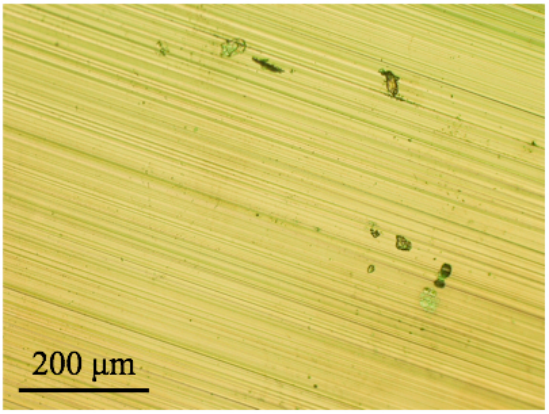

Figure 6.27. Optical micrograph of the back face in specimen M20A after testing.

single planar crack propagating to the grain boundary. The part of the curve shown for M30A here is for the second part of the test after the ligament in the first grain was cut off. The comparison made here between the different twist angles is particularly

appropriate because all the specimens were tested using the same testing machine and loading configuration. In the initial stages of crack-grain boundary interaction, as the twist angle increases, the resolved opening stress on the basal planes in the second grain

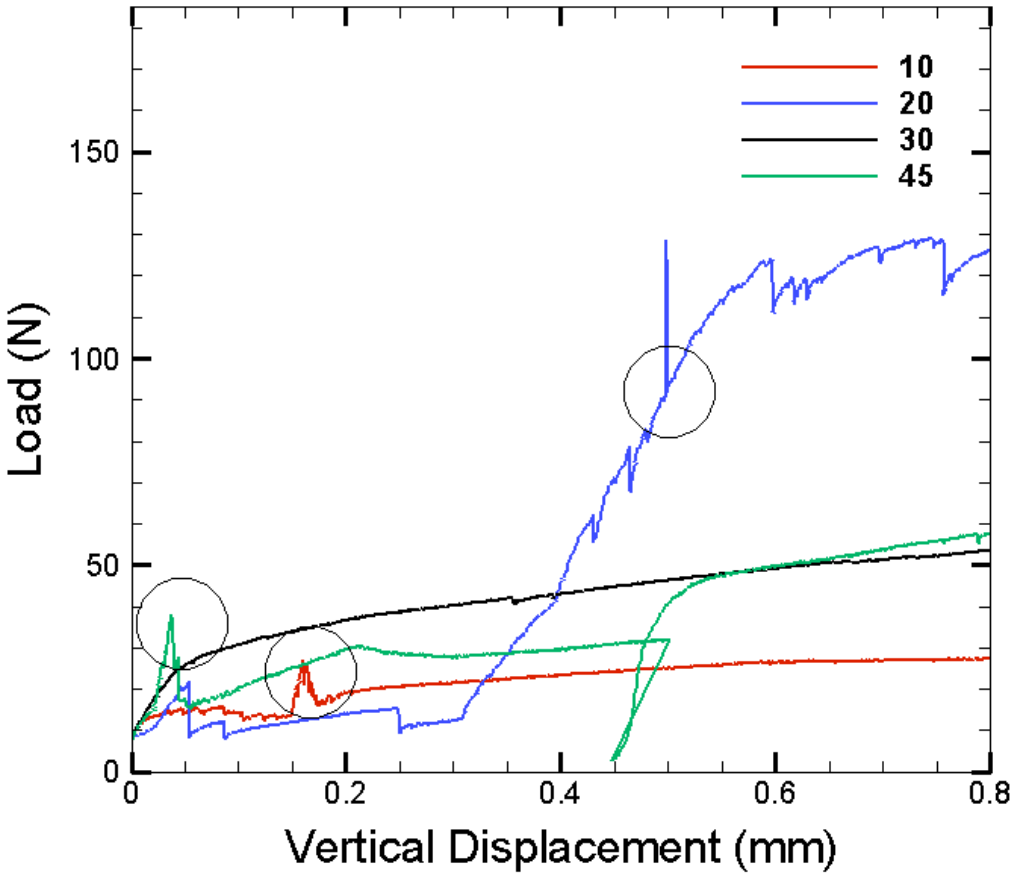

Figure 6.28. Comparison of the Load-vertical extension curves for specimens tested using the microtesting stage. Four curves, one for each case of twist angle are shown here and the data is taken from specimens M10A, M20A, M30A and M45A. A significant effect of the twist angle can be seen in the curves.

due to the crack-tip declines, thereby necessitating greater remote loads for crack initiation. If we recall that cracks in the second grain were observed for both the 10º and the 20º cases, this explanation is qualitatively consistent with the difference in the load-extension curves of the 10º and 20º specimens in Figure 6.28, where the average load for

the 20º specimen is considerable larger than that for the 10º specimen, which sustains loads very similar to those seen in single crystal specimens (see Chapter 5). Experiments on single crystals where the specimen dimensions were not identical show much smaller differences in the load (Fig 5.5). Hence, it is possible to say that the large differences in load observed in the bicrystals are not a consequence of variation in the specimen dimensions, but due to the variation in the twist angle.

Interestingly, as the twist angle increases beyond 20º, the average load sustained by the specimen declines as evidenced by the load-extension curves in Figure 6.28: in the 30º specimen, the load is considerably smaller than that for the 20º specimen, but still higher than that seen in the 10º specimen; and in the 45º specimen, the load is even lower than that in the 30º case. The cracks observed in the second grain in the 30º and the 45º specimens were of a much smaller length scale than those seen in specimens with lower twist angles. Plastic deformation, however, was quite significant, though the magnitudes of plastic deformation in all the bicrystals cannot easily be compared, as they were all not deformed to the same extent. The decline in the load must be related to the ease of plastic deformation, both near and away from the crack-tip in either grain, as there is no other possible mechanism that can accommodate the applied vertical extension. The plastic bending of the cantilever arms in the first grain cannot cause such a large degree of variation in the loads, even if the in-plane crack growth orientation were different among the different bicrystals. The load-extension curves for single crystals given in Chapter 5 show a difference of ~15 N at most between the two orientations that can be seen as two extreme cases. Small variations in sample dimensions, crack length and any other experimental considerations cannot produce such a drastic difference. There is no

evidence of microstructural differences between the bicrystals, and all of them were grown from the same batch of material in the same mold under similar conditions. Hence, by the process of elimination, it seems reasonable to conclude that the variation in the loads between the different twist angles is due to the differences in the ease of plastic deformation in the second grain, for which only the twist misorientation can be cited as a cause.

If, for reasons yet undetermined, plastic deformation becomes favored at higher twist angles, then for the same rate of vertical extension and in the absence of crack propagation in the second grain, the remote load must decline as the twist angle increases, which would explain the lower loads sustained by the 30º and 45º twist bicrystals. As basal slip traces were observed in the second grain in all the bicrystals, plastic deformation in both the grains is dominated by it in the early stages of crack-grain boundary interaction. If the critical resolved shear stress for basal slip in the second grain is reached before the critical opening stress is exceeded, then crack nucleation and propagation will not be favorable. In this case, the higher remote loads that may be required for crack initiation in the second grain become inaccessible in the loading configuration used, and the structure accommodates the applied load by simply undergoing plastic deformation, thus explaining qualitatively the absence of crack transmission across high twist angles such as 30º and 45º. Also, as the twist angle increases, the normal stress on the basal planes may decline. If the specimens are unable to reach the levels of load sustained by the 20º specimens, then crack initiation and propagation in the second grain becomes doubly unfavorable, thus strengthening the argument provided above.

The validity of this explanation obviously rests in the actual values of the resolved opening stress for basal cleavage and resolved shear stress for basal slip in the second grain, and their dependence on the twist angle, both of which are not precisely known. The role of pyramidal slip is not clear as there is no experimental evidence for it on a macroscopic scale. Given the fact that the near-tip fields and the behavior of the grain boundary region are of significant importance to crack initiation and propagation in the second grain, the above explanation, though qualitatively consistent with the experimental observations, is not sufficient. In particular, the role of pyramidal slip in the vicinity of the crack-tip on the events in the second grain must be assessed and incorporated into any analysis intended for this purpose. The complex geometric arrangement of the six pyramidal slip systems in the second grain with respect to the crack plane in the first grain makes it difficult to treat this problem in a fully analytical manner, especially given the lack of symmetry in the second grain about the loading axes. Thus a numerical analysis is warranted to explore the problem further.

6.8 Geometric and crystallographic constraints at the grain boundary

When a crack arrives at the boundary, the stress field ahead of it will cause a microcrack to nucleate along the basal plane in the second grain if the resolved normal stress is high enough. As this crack grows outward - for simplicity one can assume its front to be semi-circular as shown in Figure 6.29 - an X-shaped region is created on the grain boundary plane shown in brown. This functions as a bridge between the two cracks and the amount of material contained within will increase as the crack in the second grain grows. Clearly, this material must rupture in order for these cracks to connect, which

would require a significant amount of energy as the process cannot occur through basal cleavage, the least energy intensive failure process in zinc.

There are virtually unlimited parallel basal cleavage planes available in the second grain which suggests multiple cracking in the second grain because the opening stress ahead of the main crack tip is more or less the same anywhere along the crack front, except for the regions near the surface. But as experiments have shown in zinc as

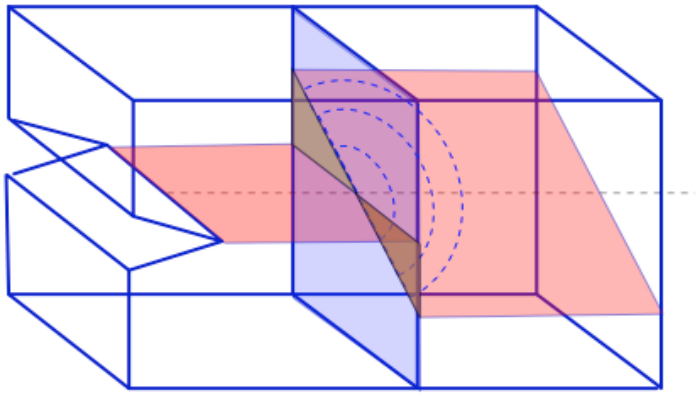

Figure 6.29. Schematic illustration of crack transmission across a grain boundary with a twist misoreintation. The red planes are those along which cracks are propagating and the blue semicircular arcs in the second grain illustrate the manner in which a crack might nucleate and propagate in the second grain. The X-shaped region on the grain boundary plane, shaded in brown, bridges the cracks in the two grains.

well as in Ti-Al [1], not all the planes experience decohesion. Given that any of these planes is a nucleation site, inhomogeneities in the microstructure that can range anywhere from micro-voids and porosity to dislocation locks, can serve as heterogeneous nucleation sites, thus adding a statistical component to fracture, an idea previously explored by Xuan et al. [18] to explain microcrack spacing in Ti-Al. If a micro-crack nucleates in a statistical fashion, then the process will immediately cause stress relaxation in the vicinity, making further cracking in this region unnecessary as an energy release mechanism. Thus one can expect a natural spacing between multiple cracks in the

second grain. Once there are multiple cracks, they are linked together by ligaments of material, the size of which clearly depends on the spacing; and these ligaments must deform and rupture in a ductile manner or by non-basal cleavage, both of which are high energy processes when compared to basal cleavage. Since the amount of energy absorbed, and thus the resistance to crack extension, are dependent on the volume of the material present in the ligament, and because the ligament size is controlled by crack spacing, crack spacing becomes an important parameter in the context of fracture resistance. Here, the experimental observations pertaining to large ligaments in single crystals are extremely relevant, as they have shown that macroscopic ligaments alone can cause basal cracks to arrest completely. In the case of a grain boundary with a twist angle, there is a grain boundary bridge associated with each micro-crack in the second grain, which is certain to add to the resistance provided by the ligaments.

Hence, in an otherwise brittle material with little inherent or intrinsic resistance to fracture, the presence of a twist angle at a grain boundary creates certain crystallographic and geometric constraints on crack propagation. This leads to the formation of grain boundary bridges and crack ligaments between multiple cracks in the second grain, which force hitherto inoperative extrinsic toughening mechanisms, in this case plastic deformation through slip and twinning as well as ductile rupture and non-basal cleavage to come to play; all of these compete with and dominate over crack propagation as the leading mechanism to accommodate the applied load, thereby leading to an increased resistance to fracture, so much so that in certain cases, crack propagation is completely contained. Interestingly, having multiple flaws or cracks spaced closely together can increase the resistance and make the structure defect tolerant to some extent, as the

applied load is shared between the cracks and loses its effectiveness in causing crack growth.

6.9 Summary

All the experimental observations clearly show that grain boundaries with a twist misorientation can significantly improve fracture resistance. Due to the presence of the grain boundary, a host of mechanisms such as kink band formation in the second grain, twinning in the crack wake, kink band formation in the first grain, grain boundary migration, multiple microcrack nucleation, crack ligament deformation etc., come into play more or less in the order of mention and interfere with crack growth. Since zinc has only one variant of basal cleavage planes per grain and no second phases and interfaces, and a more or less macroscopically planar crack has been made to grow to the grain boundary with a pure twist misorientation, it can be said with certainty that the high twist angle is the primary cause for fracture resistance. It is important to reiterate here that lack of such control over misorientation, crack geometry with respect to the grain boundary plane and the use of polycrystalline specimens in previous studies on Ti-Al [1], Al-Li [3] and Fe-Si [2], preclude the possibility of such an unambiguous conclusion. Given the complexities involved in the interaction of cracks with grain boundaries of a twist misorientation, it is worthwhile to summarize the experimental observations.

Upon reaching the grain boundary, basal cracks in the first grain come to a complete halt and cause plastic deformation in both the grains. In the first grain, this is achieved by the plastic bending of the cantilever arms through significant quantities of basal slip and twinning in the crack wake. The second grain, however, was observed to

experience strain localization fairly early during the process of crack-grain boundary interaction that produced kink bands with an out of plane displacement. These kink bands were confined to one side of the crack plane, either above or below it, with the appearance of a distorted triangle originating from the crack-tip. In all cases except one, the angle between the projections on the side surface of grain boundary and the boundary of the kink band was 12-14º; the exception was a 20º bicrystal specimen M20A, where the angle was 24º.

In certain cases, the main crack in the first grain did not reach the boundary on one of the sides. Such situations were always accompanied by a slip band originating at the stalled crack-tip and ending on the boundary. This clearly suggests a pile up of basal dislocations generated ahead of the crack-tip, which could provide shielding by reducing the driving force on the crack-tip [58]. As a consequence, the crack-tip in the first grain serves as the fulcrum for the cantilever arms, and examination of the region near the crack-tip in such cases showed kink bands of a different kind within the first grain originating from the crack-tip to accommodate the applied vertical extension. These kink bands appear to be bounded by displacement discontinuities that are mostly in-plane, as they do not show color contrast in Nomarski differential interference contrast imaging. They can be contrasted with those that occur in the second grain when the crack-tip is located at the grain boundary and clearly possess an out of plane displacement discontinuity.

It is important to note that the plastic deformation occurring after the crack in the first grain either reaches the grain boundary or comes to a halt some distance before it, is not confined to the regions near the crack-tip. The presence of basal slip traces

millimeters away from the crack-tip in both the grains indicates large-scale plastic deformation due the bending of the cantilever arms. But the lattice displacement produced due to large numbers of basal dislocations moving to the grain boundary must be accommodated there, as the dislocations are incapable of moving across the grain boundary. The expansion of dislocation loops in all directions necessary to produce the observed basal slip traces in the second grain will require a similar accommodation at the grain boundary. One may recall that in all the bicrystals, the grain boundary developed serrations that progressively increases in amplitude and intensity during loading. Upon examination at high magnification, it was concluded that these were a result of migration of small portions of the grain boundary into the first as well as the second grain in an alternating fashion. We speculate that this is a manifestation of the lattice displacement caused by dislocations that move into the grain boundary from either grain.

In bicrystals of lower twist angles (10º and 20º), some degree of crack transmission was observed in the form of macroscopic crack nucleation and propagation in the second grain upon prolonged loading long after the crack encountered the crack boundary. One of the cracks in the second grain in all these instances was observed to connect with that in the first grain at least on the surface. The spacing between cracks in the second grain cracks was of the order of hundreds of micrometers. However, in both cases, these cracks did not grow to encompass the entire length and the thickness of the specimen. Cracks that were completely confined to the interior and not observable on the side surfaces were found upon cutting the double cantilever arms to gain access to the grain boundary plane for observation. Their deformed diamond like shape when viewed

through the first grain and directly onto the grain boundary indicates crack pinning at the boundary and shear in the regions that lie between any two such parallel cracks.

Bicrystals of 30º and 45º twist misorientation did not show crack propagation in the second grain on the same scale as those of the 10º and the 20º misorientation. Upon examination of the grain boundary plane through the crack opening in the first grain, there were indications of failure at a much smaller length scale in one of the 30º specimens. Along the entire crack front in the 45º specimen, only one diamond-shaped crack, only ~15 μm wide, was observed; in contrast, the cracks observed in the lower twist angle cases were of the order of hundreds of microns or millimeters.

A strong twist angle dependence was observed in the load-displacement curves as well. The 10º bicrystals sustained the lowest loads among all the bicrystals and the 20º ones, the highest, with the 30º and 45º twist misoriented bicrystals falling in between. Though the reasons for such a behavior is not clearly understood in a quantitative fashion, one can attribute this to the effect of twist angle on (i) the resolved opening stress on the basal planes in the second grain; and (ii) the ease of plastic deformation in the second grian. The myriad other accommodation mechanisms that operate during crack-grain boundary interaction make it difficult to develop a clear picture. All of these can interfere with fracture in ways that are not easily understood. It is worthwhile to note that most of the microstructural features observed here find no mention in the literature, except for multiple cracking in the second grain. It is not clear how one can include these phenomena in a fracture mechanics framework. However, the early stages of the interaction of a crack with the grain boundary must first be understood before attempts are made to take these other phenomena into account.

So, finite element analysis that includes crystal plasticity becomes necessary to gain further insights, and to provide quantitative explanations for the experimental observations. This is the subject of the following chapter, Chapter 7, where different strategies to understand the effect of the twist angle on crack propagation across grain boundaries are presented and discussed.

Chapter 7

Bicrystals: Computational Results and Discussion

7.1 Stationary crack at the grain boundary

As a natural extension to the model presented in Chapter 4 for single crystals, bicrystals were modeled as three-dimensional solids with multiple elements along the thickness. Due to computational limitations, the thickness of the model was only 0.3 mm whereas that of the test specimens was ~8 mm. The mesh size adopted for these calculations as well as the total applied displacement (56 μm) were comparable to that used in the single crystal computations. Since the total applied displacement in the experiments was of the order of millimeters, this model can be viewed as representing only the early stages of crack-grain boundary interaction. Due to the element distortion produced as a consequence of plasticity, one cannot continue these simulations beyond this point without remeshing at intervals of 100-150 seconds. The enormous computational resources required, coupled with the difficulty of remeshing regions around the crack-tip with a non-uniform mesh, makes simulating millimeters of applied extension impractical. Also, the model does not account for crack growth and therefore, the results must be interpreted with caution, especially given the fact that crack propagation in the second grain was observed in bicrystals with low twist angles (10º and 20º) as described in Chapter 6.

7.1.1 General features of the stress and strain fields in the second grain

Bicrystals of twist angles 5º, 10º, 15º, 20º, 25º, 30º, 35º and 45º were simulated and the representative stress contours of the Mises stress and the resolved opening stress (σ'_{33}) along the basal plane in the second grain for a twist misorientation of 10º are shown in Figures 7.1a and 7.1b, respectively. Along the grain boundary, there is a region of stress concentration in the second grain, and the stress field appears irregular on the surface. Unlike in the case of single crystals, there is no mirror symmetry about the crack propagation direction and the stress and strain fields will vary along the specimen thickness.

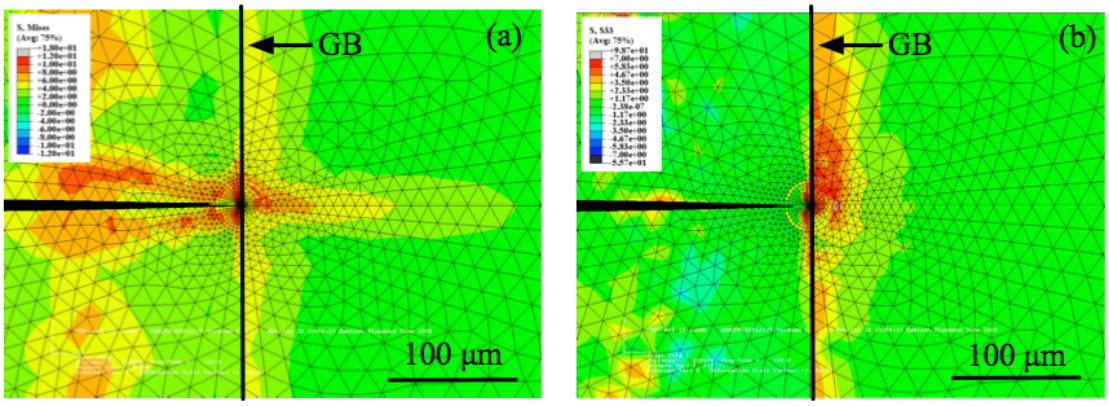

Figure 7.1. Contour plots of (a) Mises stress and (b) resolved opening stress along the basal planes for a 10º bicrystal after 56 μm vertical extension. The position of the grain boundary is marked by a vertical line.

The coordinate axes are chosen in such a way that the 1, 2 and the 3 directions are the crack propagation direction or horizontal, the thickness direction or the crack front (in grain 1) and the vertical, respectively, and the normal to the basal plane in the second grain is denoted by 3′ (and the opening stress by σ'_{33}). Figure 7.2a shows a contour plot of the resolved opening stress in a section 0.2 mm in radius in the second grain in the

vicinity of the crack-tip, where the variation of σ'_{33} on the grain boundary plane and one of the free surfaces can be seen. In Figure 7.2b, a cut-away section obtained by slicing the region in Figure 7.2a mid-way along the 1-3 plane is shown. A similar set of contour plots is displayed in Figure 7.3 for a 45º twist angle specimen. Figures 7.1-7.3 illustrate the complex nature of the stress distribution in the second grain. Upon careful examination of Figures 7.2a and 7.3a, an approximately inverted mirror symmetry about the mid-plane is observed in the stress distribution. The section shown in Figure 7.2b is therefore sufficient to gain a full appreciation of the distribution of both, the stress and strain in the second grain, and will be used hereafter as a representative section.

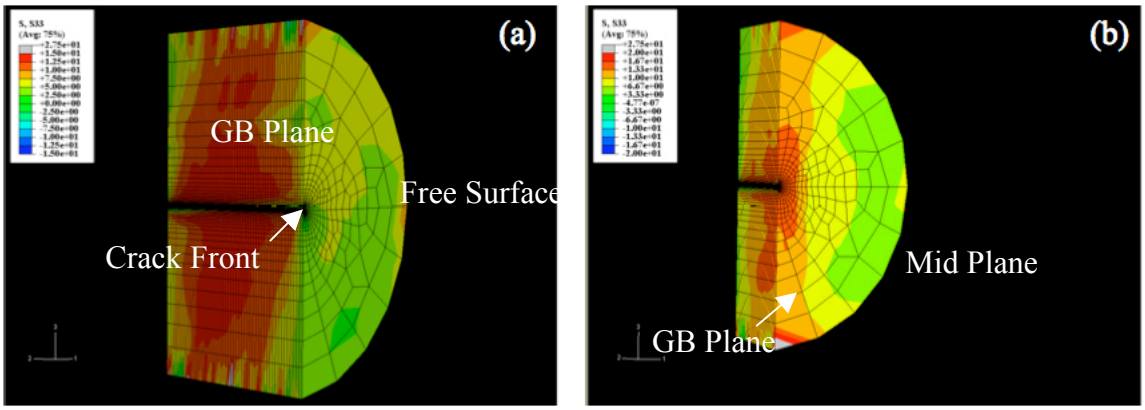

Figure 7.2. (a) Contour plot of resolved opening stress in a section in the second grain that contains the grain boundary plane. The free surface and the grain boundary plane are visible (b) A cut-away section obtained by slicing the section in (a) vertically into two equal halves. The mid-plane and the grain boundary plane are seen here. Both the plots are for the case of a 10º twist angle.

7.1.2 Variation of the resolved opening stress on the basal planes in the second grain

The variation of σ'_{33} along the horizontal on the mid-plane as well as the surface is shown in Figure 7.4 for bicrystals of twist angles 10º, 20º, 30 and 45º at the same value

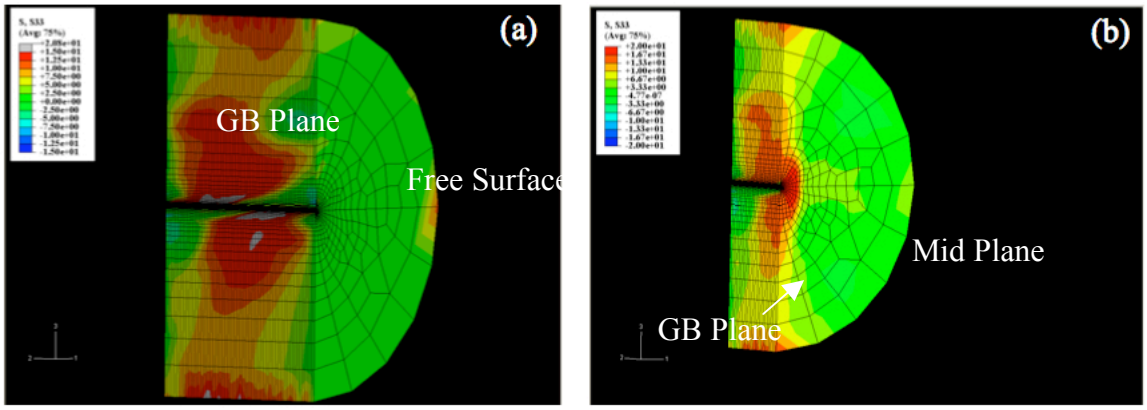

Figure 7.3. (a) Contour plot of resolved opening stress in the second grain for a 45º bicrystal. (b) Contour plot of the same on the mid-plane and the grain boundary plane.

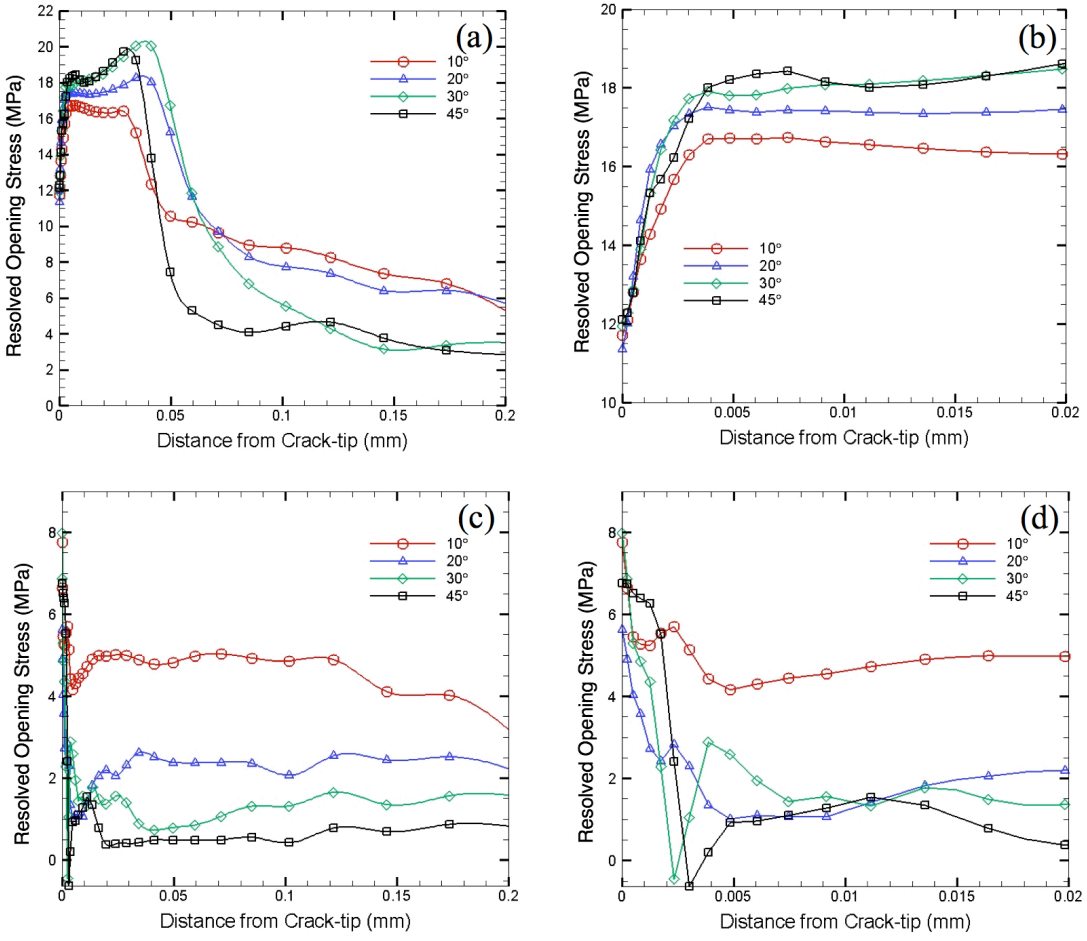

Figure 7.4. (a) Variation of the opening stress in the second grain with distance from the crack-tip on the mid-plane for four different twist angles. (b) Magnified view of the plot in (a). (c) Variation of the opening stress in the second grain with distance from the crack-tip on the free surface. (d) Magnified view of the plot in (c).

of applied displacement. All such comparisons made in this chapter are at the same value of applied displacement (56 μm). In Figure 7.4a, the variation of σ'_{33} for the mid-plane is shown, and a magnified view of the same plot near the crack-tip is shown in Figure 7.4b. Similar plots for σ'_{33} variation on the surface are displayed in Figures 7.4c,d. Intermediate twist angles such as 5º, 15º etc. are not shown as they can be inferred from the plots displayed in Figure 7.4. The variation on the surface is irregular as pointed out earlier, but the variation on the mid-plane shows regularity in that the stress increases to reach a peak (at 4 μm) as one moves away from the crack-tip and begins to decline afterwards. A similar observation was made in single crystals in Chapter 5, and is expected when finite strains are present in the vicinity of the crack-tip. Interestingly, the resolved opening stress on the basal planes is increasing marginally with increasing twist angle along the mid-plane, an observation contrary to what is generally thought to be true; but the trend observed on the surface is not quite the same.

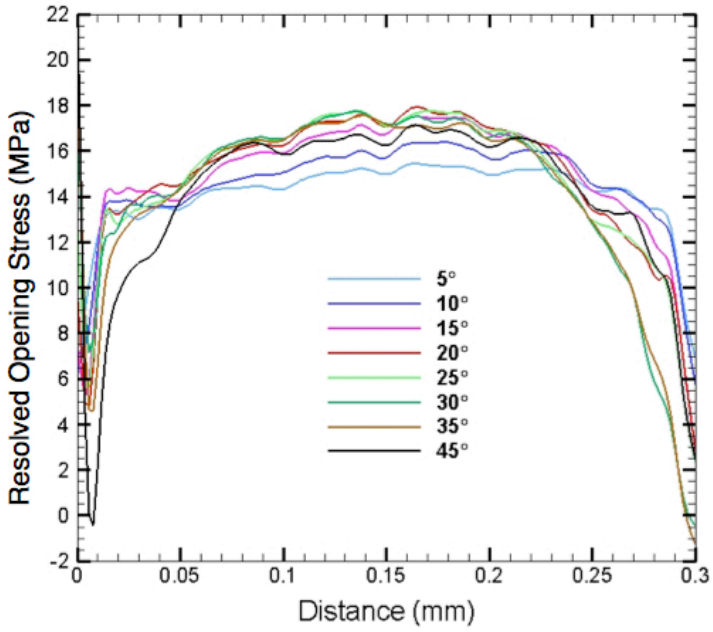

Figure 7.5. Variation of the opening stress along the thickness at a distance of 2.3 μm from the grain boundary for twist angles between 5º and 45º.

An appreciation of the through-thickness variation of the same stress component (σ'_{33}) is gained through Figure 7.5, where this is shown at a distance of 2.3 μm from the grain boundary into the second grain along the 2-axis for all the bicrystals at the same value of applied displacement. For any given twist angle, there is minimal variation in the opening stress in the region that is 0.05 mm beneath the surface from either side. The average value of the stress along the thickness in this regime is plotted against the twist angle in Figure 7.6. There is a sharp increase until 20º, following which it declines steadily. One can also notice that the missing value for 40º can be interpolated from this plot given the smooth variation of the curve.

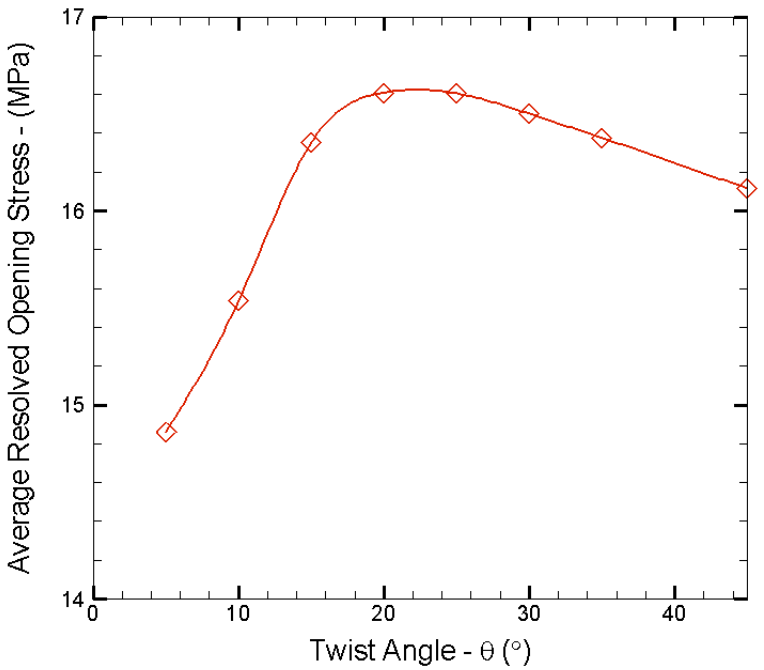

Figure 7.6. Variation of the thickness-average of resolved opening stress at a distance of 2.3 μm from the grain boundary with the twist angle.

However, in all cases, the variation of the average stress is less than 2 MPa. A similar trend exists in the angular variation of the opening stress on the mid-plane for the different twist angles, and Figure 7.7 shows such a comparison at a distance of 2.3 μm from the grain boundary into the second grain. In addition, a constant stress sector between -45º and +45º (measured from the crack plane about the 2-axis) is also evident from the plots displayed in Figure 7.7. This can be contrasted against such a sector found between -66º and +66º in single crystals. Unlike in the case of single crystals where the stress declines rapidly outside the sector, in the case of bicrystals, the stress in the second grain reduces but follows an irregular pattern outside the sector. Interestingly, the trend shown in Figure 7.6 (i.e. a maximum in the opening stress at a twist misorientation of 20°) is magnified outside the constant sector.

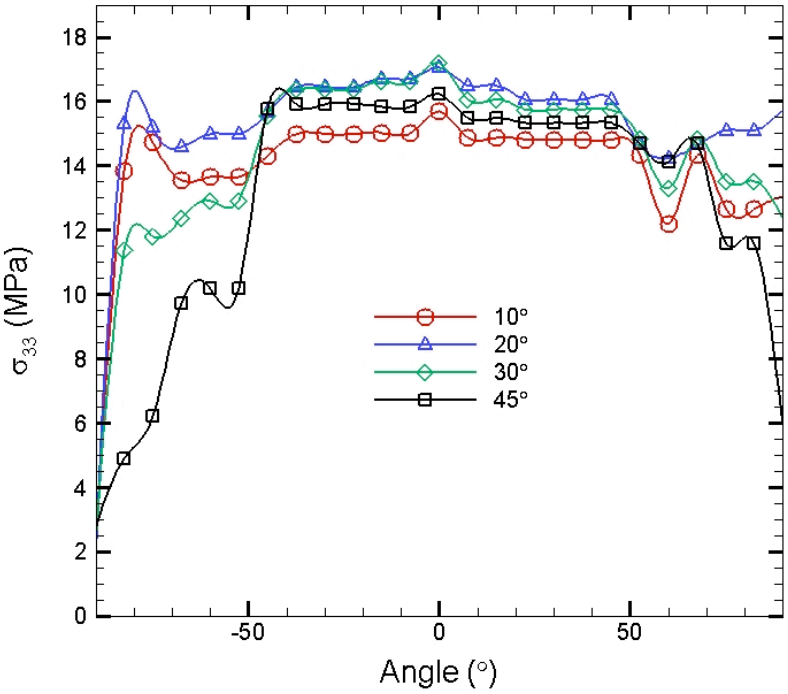

Figure 7.7. Angular variation of the resolved opening stress at a distance of 2.3 μm from the grain boundary for four different twist angles at the same value of applied displacement (56 μm)

7.1.3 Plasticity in the second grain

Contour plots of accumulated plastic strain in the second grain are shown in Figures 7.8a and 7.8b for twist angles 10º and 45º, respectively. Clearly, the size of the plastic zone as well as the magnitude of plastic strain are significantly higher in the 45º

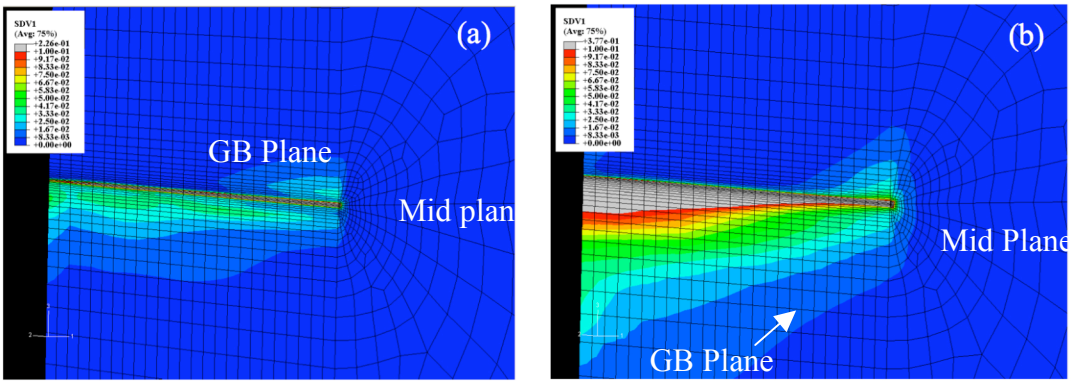

Figue 7.8. Contour plots of accumulated plastic strain on the mid section and the grain boundary plane in (a) the 10º and (b) the 45º cases.

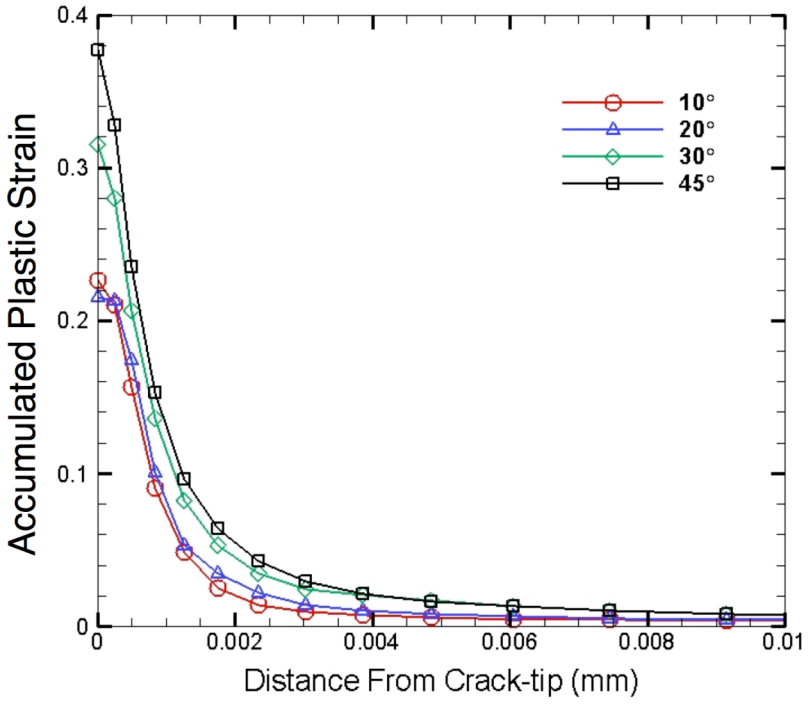

Figure 7.9. Variation of plastic strain with distance from crack-tip.

case. Figure 7.9 shows the variation of plastic strain with distance along the 1-axis from the crack tip on the mid-plane for four twist angles. The angular variation of plastic strain at a distance of 2.3 μm from the grain boundary on the mid-plane and on the specimen surface are shown in Figures 7.10a and 7.10b, respectively.

In all the plots, the common trend is the increase in the magnitude of the plastic strain and the size of the plastic zone with increasing twist angle. Another important observation to make here is that unlike in the case of stress, there is a substantial difference in the plastic strains as the twist angle changes: for instance, if Figure 7.10a is considered, the plastic strain in the case of 45º is three times that observed in the 10º case, whereas the differences in stress were not larger than ~12%.

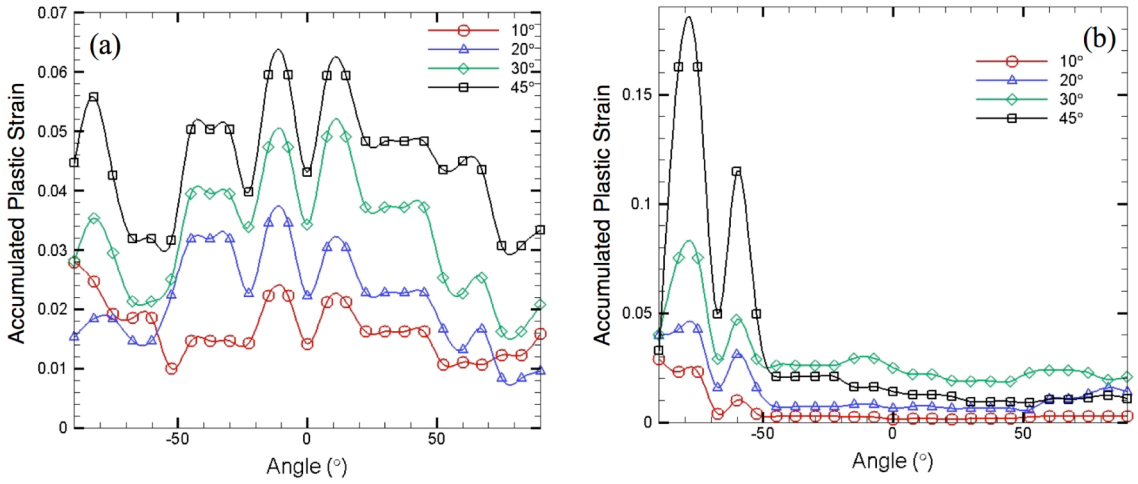

Figure 7.10. Angular variation of plastic strain at a distance of 2.3 μm from the grain boundary on (a) the mid-plane, and (b) the free surface.

Figure 7.10a shows strain localization around ±12º and constant strain sectors between ±20 and ±45 in the mid-plane for all the twist angles. On the free surface, the

strain distribution is markedly different in that there is a much greater degree of strain localization (Figure 7.10b) at 13º and 37º, which occurs only on one side of the crack plane. Strain localization of this kind has been reported earlier in analytical and numerical analyses of crack-tip stress fields incorporating crystal plasticity by Rice [33] and Forest et al. [59, 60], and in experiments by [35]. Depending on the orientation, two main types of bands are caused by the strain localization [59]: (i) slip bands along the slip plane due to single slip; and (ii) kink bands lying in a plane normal to a slip direction. Combinations of slip and kink bands are also possible, as are slip bands due to slip along multiple slip directions. While the strain localization seen on the free surface in our calculations can be interpreted as one of the above-described varieties of bands, to ascertain its type requires the accurate determination of its orientation in three dimensions. Due to the limited number of elements in the circumferential direction and the fact that the mesh does not reflect the inherent hexagonal symmetry of the crystal, this is not possible without a careful study of mesh dependence.

7.1.4 Activity of individual slip systems

In all the bicrystals, all the basal and pyramidal slip systems were found to be active in the second grain. But most of the plastic strain is shared among one basal system and two pyramidal systems symmetrically oriented about the basal plane. These three systems correspond to the ones active in the single crystals of orientation 1 (Chapter 5). The other slip systems are active in a region not larger than 0.2-0.5 μm, with plastic strain that is an order of magnitude smaller than that accommodated by the primary slip systems. Also, 0.2-0.5 μm is a small region compared to the size of the plastic zone,

which can be as large as 10 μm (see Figure 7.9). The dependence of plastic strain in individual slip systems on the twist angle does not follow a clear trend, unlike the one observed in the case of the total accumulated plastic strain. The relative magnitudes of plastic strain in the different slip systems vary in a non-monotonic fashion with the twist angle, and produce a monotonic increase in the total plastic strain.

7.1.5 Load – vertical extension curves

Load-vertical extension curves for bicrystals of 10º, 20º, 30 and 45º are shown in Figure 7.11. Unlike the large degree of variation observed in experiments among bicrystals of different twist angles (Figure 6.28), the simulations show virtually identical curves.

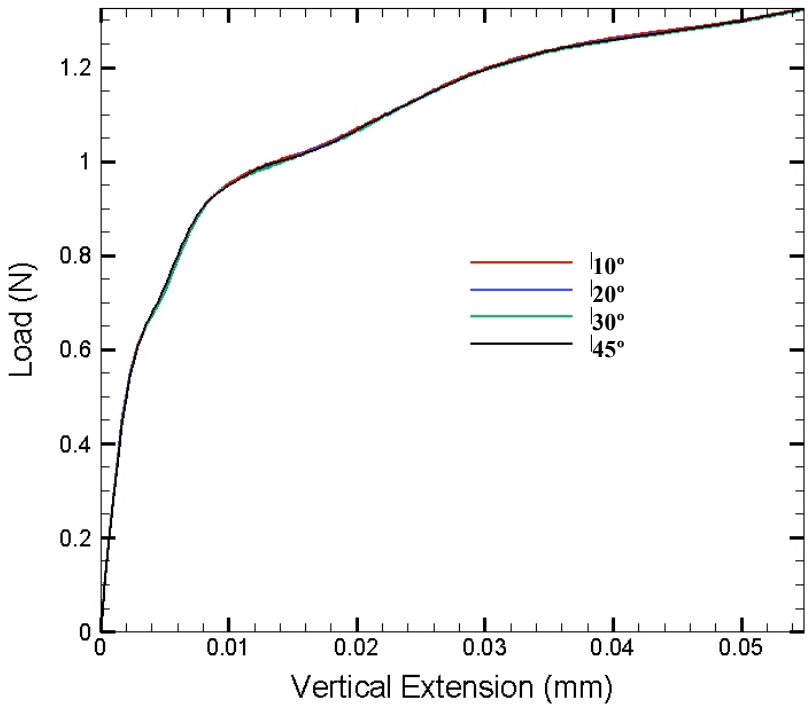

Figure 7.11. Comparison of load-extension curves for four different twist angles. The four plots are superimposed upon each other.

7.1.6 Discussion

Two trends in the variation of the opening stress and plasticity with the twist angle in the second grain are worth noting in the results presented above: (i) an increase in the average opening stress from 0-20º, and its subsequent decrease with increasing twist angle; and (ii) a monotonic increase in the total plastic strain with increasing twist angle.

The first trend would suggest that for the same applied crosshead speed, crack propagation would initiate in the 20º bicrystals at a lower load when compared to the 10º bicrystals, if a critical opening stress criterion is assumed. One may recall from Chapter 6 that the loads observed in the 20º twist bicrystals were significantly larger than those seen for the 10º twist misorientation (Figure 6.28). The trend in the variation of average normal stress shown in Figures 7.6 and 7.7 is therefore not consistent with the experimental observations regarding the twist angle dependence of crack initiation in the second grain. Here, we have tacitly assumed a critical opening stress criterion for crack initiation. Mixed mode criteria are ineffective because the shear stress supported by the basal planes is small (< 1MPa) compared to the normal stress (~5-10 MPa). So, Mode II and Mode III loading are expected only to produce basal slip without causing crack growth. It is important to note that this model does not take into account crack propagation. Since it is not known how the load might be affected as a consequence of crack growth in the second grain along multiple planes and the attendant deformation of ligaments, it is not possible to verify the authenticity of the simulations or to dismiss it as inconsistent. In fact, the difference in the maximum and minimum values of the average opening stress in Figure 7.6 is only 2 MPa, which is too small to explain the large

difference in the load observed between the 10º and the 20º bicrystals in the experiments. Thus, in reality, this trend may be inconsequential to crack growth in the second grain.

The increases in the plastic strain in the vicinity of the crack-tip and the size of the plastic zone with an increase in the twist angle seen in Figures 7.9 and 7.10, respectively, are of a greater degree than those seen in the stress. They clearly suggest that as the twist angle increases the ease of plastic deformation increases, which would compete with and suppress crack initiation at higher twist angles. This trend is consistent with the experimental observations, if one recalls the fact that crack growth on a macroscopic scale was not observed in the 30º and the 45º bicrystals, (Chapter 6). However, one must be cautious in employing this argument as a rationalization of the experimental observations, as this model can only be applied to the initial stages of crack-grain boundary interaction.

In Chapter 6, kink bands with an out of plane displacement were reported in most of the bicrystals, and the angle in most cases was 10-12º; the exception being specimen M20A with a kink band making a 24º angle with the grain boundary. It is possible that the strain localization at 13º in Figure 7.10b corresponds to most of the experimentally observed kink bands. A certain association between the experiments and the simulations can be made only upon mesh dependence studies, as the limited number of elements in the circumferential direction in the mesh employed here poses a significant difficulty in accurately locating the shear discontinuities in the simulations. The prediction of kink bands occurring only on one side of the main crack plane is also supported by experimental observations (See Chapter 6). Of all the accommodation mechanisms and crack propagation across the boundary, kink band formation in the second grain was

observed to occur first and immediately after the crack reached the grain boundary. It is, therefore, a feature that must be captured in a simulation of the early stages of crack-grain boundary interaction. Thus, with respect to kink band formation in the second grain, there appears to be an agreement between the experimental observations and the simulations as to its location. While this may be the case, it is still not clear how the kink bands in all the bicrystals occur at the same angle with respect to the grain boundary in experiments as well as computations despite the difference in orientation; for their location is determined by the orientation of the different slip systems. Since kink bands in the interior regions of the specimen cannot be observed, no such comparison is possible between the experimental and computational observations.

As one increases the applied vertical extension further than 100 μm, as seen in Chapter 6, other accommodation mechanisms come into play such as the accommodation of large scale plasticity at the grain boundary and the consequent grain boundary migration and twinning in the crack-wake. Our model does not take into account these features that may play important roles in crack propagation as well as plastic deformation. It is plausible that the effect of the twist angle on the experimental load-extension curves is a manifestation of these other phenomena, in which case the mild reverse trend in the stress and the absence of a twist angle dependence on the load-extension curves in the simulations may not invalidate the model itself. All of the above speculations can be verified only when more sophisticated models that incorporate the missing physics become available.

7.2 Modeling crack propagation across a grain boundary with twist misorientation

Here we present some preliminary attempts to model crack propagation through grain boundaries using the cohesive zone formulation in conjunction with crystal plasticity in ABAQUS. This model reflects the actual geometry of the bicrystals used in testing. However, the need to incorporate cohesive zones and the size of the model restricts the mesh size and only a coarse mesh could be used. The use of coarser elements permits the simulation of larger vertical extensions because of the lesser degree of element distortion. The total applied displacement in the case of this model was 3.5 mm, a value comparable to those used in the experiments. Figure 7.12 shows a snapshot from the simulation conducted for a 20º twist bicrystal with contours of Mises stress superimposed on the geometry. The pronounced discontinuity in deformation at the grain boundary as well as the bending of the cantilever arms, reminiscent of post deformation experimental bicrystal specimens (Figure 6.19), can be observed in Figure 7.12.

In Figure 7.13, only the second grain is shown with contours of opening stress along the basal planes with the grain boundary in view. The portions on the grain boundary plane appearing in red are regions of stress concentration, and close inspection of this plane revealed that all the cohesive zones experienced failure near the grain boundary, though the distance through which the different crack fronts propagated were different. This was true in the case of the model for the 10º twist bicrystal as well. In an attempt to compute the characteristic microcrack spacing in the second grain, the spacing between consecutive cohesive zones was ensured to be smaller than that observed in the experiments, where despite the presence of unlimited number of parallel cleavage planes,

only a small fraction was observed to experience failure. Though the nucleation and propagation of multiple cracks in the second grain is simulated by the model, the spacing

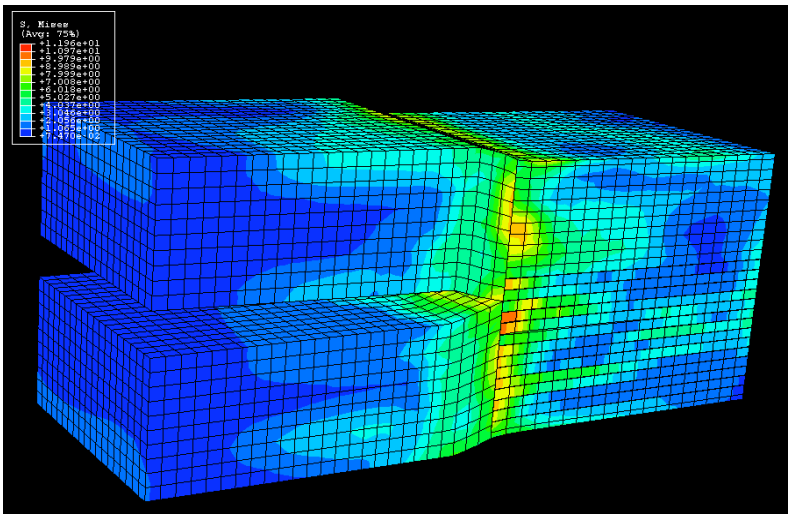

Figure 7.12. Contour plot of Mises stress for a 20º bicrystal after 2mm vertical extension.

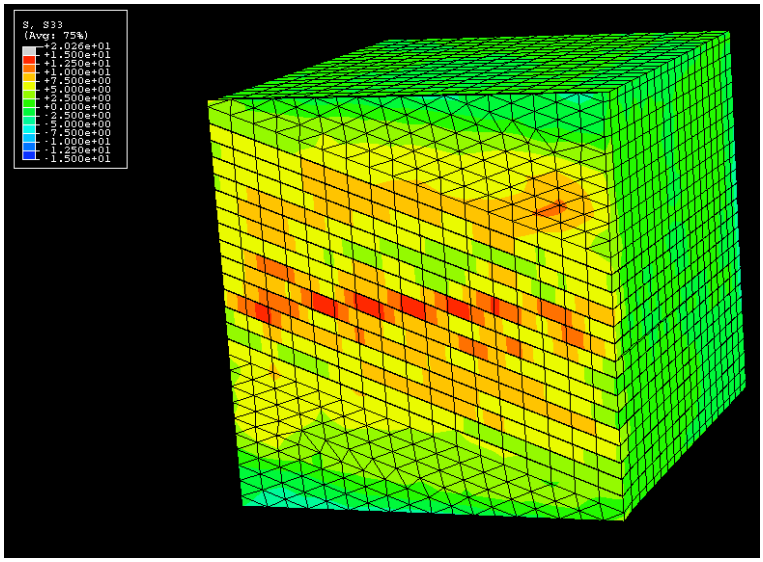

Figure 7.13. Contour plot of opening stress on the basal planes on the grain boundary plane. Note that all the cohesive elements along the grain boundary plane have experienced separation.

between the cracks is clearly not captured, and no information regarding the characteristic spacing could be obtained from this model. This is possibly due to the fact that the mesh is too coarse to capture the crack-tip stress fields with the desired accuracy.

The load-extension curves for the 10º and 20º cases obtained from simulations are compared to the experimental curves in Figure 7.14. The curves for the simulation fall between those of the experimental curves for the 10º and the 20º specimens. Except for the fact that marginally higher loads are observed in the 20º case, there is little agreement between the experiments and the simulations.

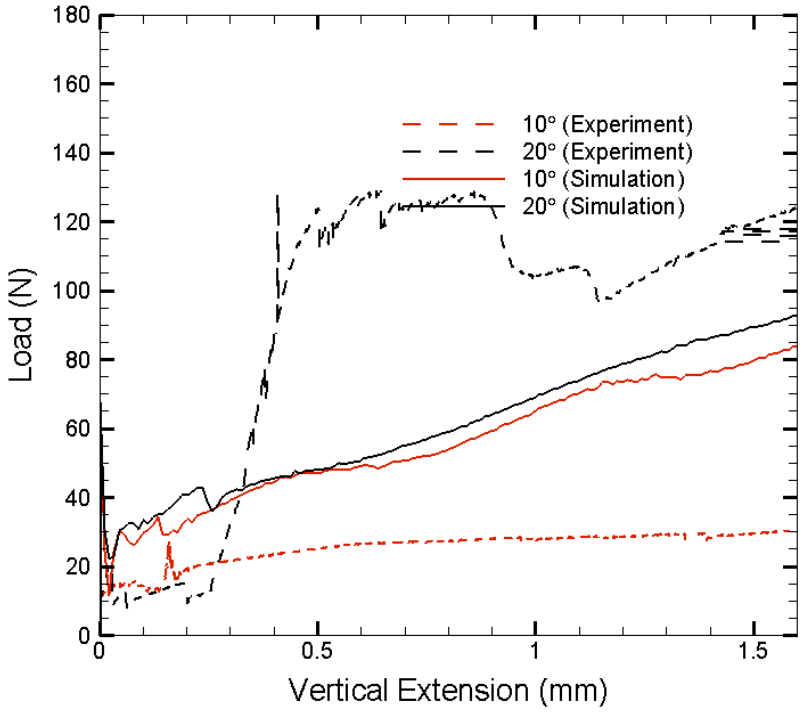

Figure 7.14. Comparison of load-extension curves between experiments and simulations.

The reasons for the failure of this model to quantitatively capture experimental observations were investigated by means of similar simulations in single crystals. Other than the drawbacks that arise from lack of mesh refinement, there appears to be an

inherent shortcoming in the cohesive zone formulation when applied in conjunction with an explicit dynamics crystal plasticity scheme. A refined mesh with triangular prism elements was employed in addition to the brick elements to investigate the effect of the type of element. In both cases, though there is agreement between experiments and computations with respect to the particular slip systems that activate in the vicinity of the crack-tip, all of it was restricted to the crack-wake, while the region ahead of the cohesive zones experienced only elastic deformation. Figure 7.15 shows basal slip in the crack-wake in one of these models.

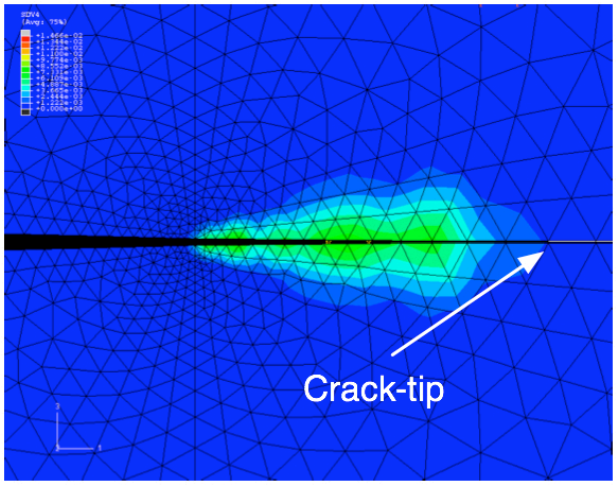

Figure 7.15. Contour plot of plastic strain in a basal slip system in the crack-wake in a single crystal crack-growth model. Note the lack of plastic deformation ahead of the crack-tip.

This discrepancy can be attributed to the lack of balance between the properties of the cohesive zones and the surrounding material. Cohesive zones experience opening before the critical resolved shear stress for any of the slip systems is reached ahead of the crack-tip. When the critical opening stress for failure of the cohesive zones was increased, there was significant plasticity ahead of the crack-tip without crack growth. Thus the balance between the parameters is critical to achieve both plasticity and crack

growth in the cohesive zone formulation being employed here; but such a balance is too fine to arrive at by trial and error, and could not be achieved here due to the significant computational times involved. It is nevertheless possible, though impractical, in the framework employed here.

This effort, despite having met with limited success, demonstrates that features such as multiple microcrack formation and the consequent deformation of ligaments can be captured. However, to do so in a quantitative fashion would require dealing with the shortcomings by resorting to more sophisticated methods. For instance, the difficulties involved in mesh generation and refinement can be significantly reduced by the use of partition of unity methods that are recently being applied to crack propagation problems. These methods, sometimes referred to as extended FEM or simply, XFEM, do not require the use of cohesive zones, as the elements themselves are capable of separating according to a prescribed constitutive relation. Not only will this relax the several constraints that the incorporation of cohesive zones would place on the mesh, but will also eliminate the need for a fine balance of the cohesive zone parameters. The computational times can be brought down by means of parallel computation. Though ABAQUS is capable of doing this, the user subroutine for crystal plasticity, written partly in FORTRAN 77, is not thread-safe and does not permit parallel computation.

Chapter 8

Conclusions

Controlled crack growth studies using a combination of *in situ* experiments and computations at the continuum level have provided new insights into (i) several micromechanisms of basal cleavage in single crystals of zinc and (ii) the effect of twist misorientation of the basal plane across a grain boundary in bicrystals on fracture resistance and associated damage-accommodation mechanisms. These are summarized below.

8.1 Crack Propagation in Single Crystals

(1) Crack propagation alternates between dynamic crack extension and periods of arrest, the former being accompanied by load-drops and the latter being associated with crack-tip blunting by plastic deformation. Following blunting, further crack growth occurs by microcrack nucleation on a parallel basal plane, with the ligament bridging the two cracks experiencing plastic deformation and eventually, fracture.

(2) Finite element analysis incorporating crystal plasticity conducted on stationary cracks in single crystals shows that the resolved opening stress on the basal planes reaches a maximum a few micrometers away from the crack-tip, following which it declines. This explains the experimental observation of microcrack nucleation on multiple basal planes

ahead of the main crack-tip, ligament formation and the consequent fracture surface topography of cleavage steps parallel and perpendicular to the crack front.

(3) Crack growth behavior, the load-displacement curves, the appearance of fracture surfaces and the activity of pyramidal slip systems were all shown to be orientation dependent through experimental observations.

(4) Finite element analysis was used to successfully explain this orientation dependence as a consequence of the differences in the geometric disposition of the slip systems with respect to the crack growth direction. The difficulty in activating pyramidal slip ahead of the crack-tip when the crack grows along a <10-10> direction as opposed to a <11-20> direction produces higher opening stresses in the former case; this reduces the toughness, causing the specimens to fracture at a lower remote load.

(5) The role of pre-existing twins and of macroscopic ligaments that bridge cracks on retarding crack growth was elucidated by *in situ* experiments. Both were observed to produce significant resistance to crack propagation, and, in some cases, completely contain fracture. While twins produce resistance through crack deflection due to lattice rotation across a twin boundary, macroscopic ligaments achieve this by shielding cracks from the remote load and promoting significant plastic deformation that can compete with crack growth. These have implications for intragranular toughening in polycrystalline materials.

8.2 Crack propagation across grain boundaries in bicrystals

(1) Significant resistance to crack growth was observed in all the bicrystals once a Mode I basal crack in the first grain reached the grain boundary. In the 10º and 20º twist misoriented bicrystals, the stress field ahead of the crack caused the nucleation of multiple cracks along basal planes in the second grain, these being separated by a few hundred micrometers. These cracks nucleate internally at (or in the vicinity of) the grain boundary and then grow out towards the surface. In bicrystals of higher twist angles such as the 30º and the 45º twist misoriented bicrystals, cracks of this nature were not readily observed; the specimens instead accommodated the applied load through significant plastic deformation in both the grains.

(2) Despite the low intrinsic fracture toughness registered during uninterrupted basal cleavage (< 1MPa √m), complete fracture of the specimen was not observed in any of the tests on the bicrystals, an observation indicative of the high degree of resistance provided by grain boundaries including a twist misorientation of the fracture plane across the boundary. Cracking in the second grain, when observed, was confined to parts of the second grain without encompassing the entire length and the thickness of the specimens.

(3) A variety of mechanisms that compete with and dominate over crack propagation across grain boundaries were documented. These included kink band formation in the second grain with an out-of-plane displacement, multiple microcrack nucleation in the second grain and the attendant deformation of crack ligaments, twinning in the crack

wake in the first grain, grain boundary migration, and kink band formation in the first grain. Except for multiple microcrack nucleation, the other mechanisms have not been previously reported.

(4) Crack growth resistance is attributed to crystallographic and geometric constraints placed by a twist misorientation on the crack path that creates bridging ligaments at the grain boundary as well as between parallel cracks in the second grain. These force several extrinsic toughening mechanisms involving extensive plastic deformation into operation that suppress crack nucleation and growth in the second grain. Due to a precise control of the crystallography as well as the single phase nature of the microstructure used in this study, the observed fracture resistance can be unambiguously attributed to the twist component of misorientation at the boundary.

(5) A strong twist angle dependence was observed in the load-displacement curves: the average load sustained by the 20º twist bicrystals was several times that observed in the 10º bicrystals; the average load for the 30º and 45º twist bicrystals was intermediate between the 20º case and the 10º case. This dependence is possibly due to the variation with the twist angle of the normal stress on the basal planes and the ease of plastic deformation in the second grain.

(6) Finite element simulations of the early stages of crack grain-boundary interaction suggest strain localization leading to kink band formation in the second grain as seen in the experiments. They also show that the ease of plastic deformation increases with

increasing twist angle, which can at least in part explain the lack of crack transmission across grain boundaries of high twist angles e.g. 30º and 45º. However, these simulations were unable to explain the effect of the twist angle on the load-displacement behavior observed in experiments.

(7) Another finite element model that incorporates the cohesive zone formulation was developed to capture mechanistic features such as multiple microcrack nucleation in the second grain and the attendant deformation of crack ligaments. Plasticity ahead of the crack-tip was suppressed in these simulations due to numerical reasons, and, as a consequence, the model was unable to quantitatively account for these phenomena. However, as a first step, the model demonstrates that the microstructural features themselves can be simulated.

In conclusion, careful experiments and computations in single crystals as well as in bicrystals demonstrate that the overall fracture resistance can be increased significantly by the presence of some common microstructural features such as twins and grain boundaries, and suggest the possibility of similar mechanisms as the ones reported and discussed here in other alloy systems with a propensity to undergo transgranular fracture.

Chapter 9

Recommendations for Future Research

The experimental observations presented here have yielded significant insights into the problem of crack propagation on the basal planes in single crystals of zinc as well as through grain boundaries in bicrystals that include a twist misorientation of the cleavage plane across them. The general methodology used to achieve these insights and the particular experimental methods utilized were successful, and can be used for future studies in other materials. Likewise, the computational models developed thus far (at the continuum level) could serve as good starting points for future investigations that can incorporate greater detail and sophistication. In this context, although our modeling efforts have succeeded in explaining the micro-mechanisms of fracture observed in single crystals, they have not yielded significant insights into those that are observed in bicrystals. The knowledge of crack spacing in the second grain, and the twist angle effect on the overall behavior is still only of a qualitative nature. The problems encountered during the course of these efforts were primarily of a numerical nature. The limitations on mesh size and geometry with the added difficulty of incorporating cohesive zones to simulate twist crack hampered progress in this investigation. While mesh refinement is possible if parallel processing is employed, the difficulty encountered in placing cohesive zones can be overcome through the use of partition of unity methods or extended FEM.

Several important and interesting mechanisms activated during the interaction of cracks with grain boundaries of twist misorientation, were documented but not all of these were investigated in detail. These mechanisms have been shown to operate in

parallel to create the observed resistance, but their relative importance and individual contributions to the overall fracture resistance remain yet to be determined. Strain localization in the second grain immediately ahead of the crack tip in the first grain is a phenomenon that needs attention from future researchers, especially due to the fact that it causes an out of plane displacement of macroscopic proportions. If one were to envision this second grain as being part of a polycrystalline aggregate, then the constraints placed upon it by the surrounding grains would doubtless work against kink band formation, thereby preventing the relaxation of stress to some extent. Kink band formation was observed to be the first among the many accommodation mechanisms that are activated, and is therefore likely to play an important role in providing crack growth resistance. We conjecture that if the second grain were constrained in the thickness direction during testing, it could increase the likelihood of crack propagation through the grain boundary, by allowing the structure to sustain greater loads that were hitherto inaccessible. Since a direct investigation of this kind is not possible in a polycrystalline specimen, one could conceivably use a bicrystal with the side faces of it constrained in the thickness direction and conduct similar fracture experiments as those described in our study.

Another accommodation mechanism of interest that is not fully understood is the manner in which the grain boundary accommodates the slip offsets produced by a large number of dislocations flowing into it. It was conjectured previously in Chapter 6 that this could produce the serrations observed on the grain boundary after prolonged loading. Clearly, the scale at which the observations were made during the course of this study will not yield further insights into this phenomenon; therefore, an investigation at the mesoscopic scale is warranted. To examine this phenomenon further, we conducted

some preliminary *in situ* straining experiments in a transmission electron microscope on polycrystalline zinc specimens where crack growth and dislocation emission from crack-tips were observed in real time. Figure 9.1 shows crack-tip dislocation activity in three different specimens. However, crack-grain boundary interaction could not be documented because of the tendency of these specimens to separate parallel to and/or along the grain boundary. The samples used in study were polycrystalline and not of a controlled orientation. As a consequence, the crack-tips visible in the micrographs were not Mode I cracks, and therefore these preliminary observations could not be integrated into our analysis in their current form. In this regard, we propose that further experiments of this nature be conducted with a better control of crystallography. Monitoring crack growth at the mesoscopic level would require a reasonably sized electron transparent region into which the cracks can be made to grow. From a bicrystal specimen, one can extract such regions using a focused ion beam and glue them onto a frame that can be loaded while making *in situ* observations in a transmission electron microscope. The interaction of dislocations emitted from a crack-tip with a grain boundary can be understood given the known crystallographic orientation of such specimens.

However, electron transparent films are extremely thin, and may allow dislocations to annihilate on the free surfaces. Furthermore, the state of stress ahead of the crack-tip is one of plane stress and consequently the observations made in the TEM may not truly represent behavior in bulk, and therefore such phenomena must be interpreted with caution. On the computational front, it is conceivable that the interaction

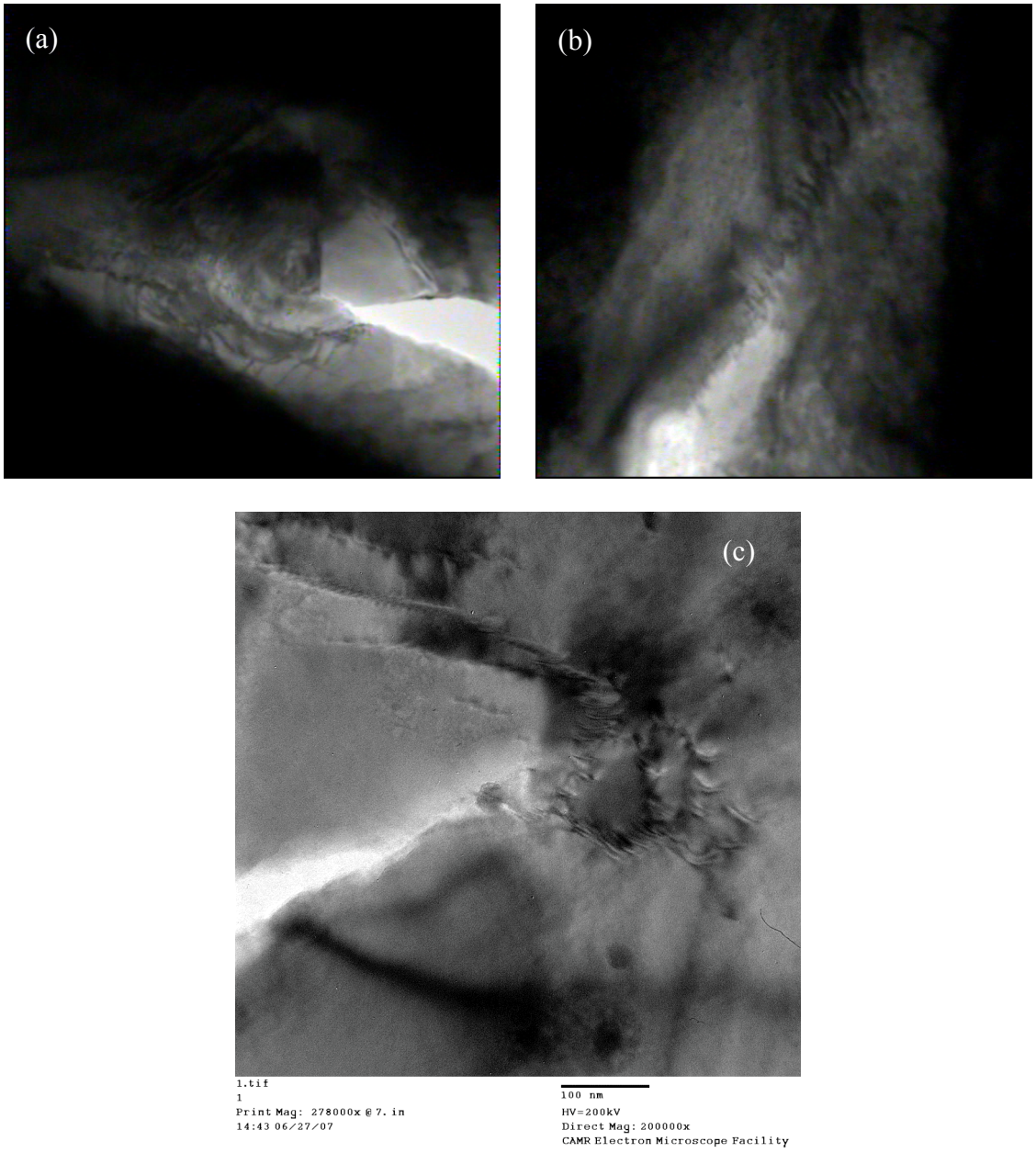

Figure 9.1. (a,b,c) Dislocation activity ahead of the crack-tip in zinc.

of dislocations emitted from crack-tips with grain boundaries and the consequential microstructural evolution on a local scale can be investigated with discrete dislocation techniques or atomistic modeling and appears to be a logical extension to this work in understanding the problem at the mesoscopic level.

Lastly, based on our experimental observations of crack transmission across the grain boundary in our bicrystals, we anticipate that specimen geometry may play a role in the resistance offered and this should be verified with thinner and thicker specimens. Specifically, though the cracks produced inside the second grain as a consequence of the main crack in the first grain were sometimes of macroscopic dimensions, their growth was restricted through the thickness of the specimens. It is conceivable that in thinner specimens these cracks would grow to reach both the free surfaces, thus increasing the chances of full failure. Thus, one can foresee the grain size of the material as being an important parameter in controlling the fracture resistance in a polycrystalline zinc specimen. A systematic study on the influence of grain size on crack growth resistance may yield several valuable insights into the effectiveness of grain boundaries as crack arresters, as would studies of this nature in other materials that exhibit a similar kind of resistance.

Chapter 10

Bibliography

1. P. Wang, N. Bhate, K.S. Chan and K.S. Kumar, *Colony boundary resistance to crack propagation in lamellar Ti–46Al.* Acta Materialia, 2003, **51**(6): p. 1573-1591.
2. A.S. Argon and Y. Qiao, *Cleavage cracking resistance of large-angle grain boundaries in Fe-3 wt Si alloy,* Philosophical Magazine A, 2002, **82**(17-18): p. 3333-3347.
3. T. Zhai, A.J. Wilkinson and J.W. Martin, *A crystallographic mechanism for fatigue crack propagation through grain boundaries,* Acta Materialia, 2000, **48**(20): p. 4917-4927.
4. G.M. Hughes, G.E. Smith, P.E.J. Flewitt and A.G. Crocker, *The brittle fracture of polycrystalline zinc.* Proceedings of the Royal Society A: Mathematical, Physical and Engineering Sciences, 2007, **463**(2085): p. 2129-2151.
5. D.I.A. Stienstra, *Stochastic micromechanical modeling of cleavage fracture in the ductile-brittle transition region,* 1990, Ph.D. Thesis, Texas A&M University, College Station, TX.
6. T.L. Anderson, D.I.A. Stienstra and R.H. Dodds Jr., *A theoretical framework for addressing fracture in the ductile-brittle transition region,* Fracture Mechanics: 24th Volume, ASTM STP 1207.
7. T.L. Anderson, *Fracture mechanics: fundamentals and applications*. 2nd ed., 1995, Boca Raton: CRC Press.

8. E.R. De Los Rios and A. Navarro, *Considerations of grain orientation and work hardening on short-fatigue-crack modelling.* Philosophical Magazine A, 1990, **61**(3): p. 435-449.

9. A. Navarro and E.R. De Los Rios, *Fatigue crack growth modelling by successive blocking of dislocations.* Proceedings of the Royal Society A: Mathematical and Physical Sciences, 1992, **437**(1900): p. 375-390.

10. Y. Qiao and A.S. Argon, *Cleavage crack-growth-resistance of grain boundaries in polycrystalline Fe–2% Si alloy: experiments and modeling,* Mechanics of Materials, 2003, **35**(1-2): p. 129-154.

11. J. Chen and Y. Qiao, *Mixed-mode cleavage front branching at a high-angle grain boundary.* Scripta Materialia, 2007, **56**(12): p. 1027-1030.

12. K.S. Chan, J. Onstott and K.S. Kumar, *The fracture resistance of a binary TiAl alloy.* Metallurgical and Materials Transactions A, 2000, **31**(1): p. 71-80.

13. Y. Gao, J.S. Stölken, M. Kumar and R.O. Ritcie, *High-cycle fatigue of nickel-base superalloy René 104 (ME3): Interaction of microstructurally small cracks with grain boundaries of known character,* Acta Materialia, 2007, **55**(9): p. 3155-3167.

14. K.S. Kumar and W.A. Curtin, *Crack interaction with microstructure,* Materials Today, 2007, **10**(9): p. 34-44.

15. J.J.M. Arata, K.S. Kumar, W.A. Curtin and A. Needleman, *Crack growth in lamellar titanium aluminide,* International Journal of Fracture, 2001, **111**(2): p. 163-189.

16. A. Needleman, *A continuum model for void nucleation by inclusion debonding.* Journal of applied mechanics, 1987, **54**(3): p. 525-531.

17. X.P. Xu and A. Needleman, *Numerical simulations of fast crack growth in brittle solids,* Journal of the Mechanics and Physics of Solids, 1994, **42**(9): p. 1397-1407.

18. W. Xuan, W.A. Curtin and A. Needleman, *Stochastic microcrack nucleation in lamellar solids.* Engineering Fracture Mechanics, 2003, **70**(14): p. 1869-1884.

19. H.A. Schmitz, *An examination of the cleavage behavior of cadmium doped zinc crystals via synchrotron x-ray topography*, 1984, Ph.D. Thesis, State University of New York at Stony Brook, NY.

20. J.J. Gilman, *Fracture of zinc-monocrystals and bicrystals.* Transactions of the Metallurgical Society of AIME, 1958, **212**: p. 783-791.

21. A.D. Sheikh-Ali, *On the influence of intragranular slip on grain boundary sliding in bicrystals.* Scripta Metallurgica et Materiala, 1995. **33**(5): p. 795-801.

22. T. Watanabe, S.I. Kimura and S. Karashima, *The effect of a grain boundary structural transformation on sliding in< 1010>-tilt zinc bicrystals.* Philosophical Magazine A, 1984, **49**(6): p. 845-864.

23. E. Schmid, *Neuere untersichungen an metallkristallen,* Proceedings of the 1st International Congress on Applied Mechanics, Delft, 1924: p. 342-353.

24. A.E. Deruyttere and G.B. Greenough, *The criterion for the cleavage fracture of zinc single crystals,* Journal of the Institute of Metals, 1956, **84**: p. 337–345.

25. E.J. Stofel, *Plastic flow and fracture of zinc single crystals*, 1962, Ph.D. Thesis, California Institute of Technology, Pasadena, CA.

26. J.J. Gilman, *Direct measurement of the surface energy of crystal,* Journal of Applied Physics, 1960, **31**(12): p. 2208-2218.

27. A.H. Maitland and G.A. Chadwick, *The cleavage surface energy of zinc,* Philosophical Magazine, 1969, **19**(160): p. 645-651.

28. A.R.C. Westwood and M.H. Kamdar, *Concerning liquid metal embrittlement, particularly of zinc monocrystals by mercury,* Philosophical Magazine, 1963, **8**(89): p. 787-804.

29. S.J. Burns, *Dislocation motion accompanying cleavage in zinc,* Acta Metallurgica, 1970. **18**(9): p. 969-980.

30. J.C. Bilello, D. Dew-Hughes, and A.T. Pucino, *The surface energy of zinc,* Journal of Applied Physics, 1983, **54**: p. 1821-1826.

31. C. Messmer, D. Dew-hughes and J.C. Bilello, *Effect of prior deformation on the cleavage of zinc single crystals,* Philosophical Magazine Part B, 1983, **47**(5): p. 635-656.

32. D. Hull, P. Beardmore and A.P. Valintine, *Crack propagation in single crystals of tungsten,.* Philosophical Magazine, 1965, **12**(119): p. 1021-1041.

33. J.R. Rice, *Tensile crack tip fields in elastic--ideally plastic crystals,* Mechanics of Materials, 1987, **6**(4): p. 317-335.

34. A.M. Cuitino and M. Ortiz, *Computational modelling of single crystals,* Modelling and Simulation in Materials Science and Engineering, 1992, **1**: p. 225–263.

35. T.W. Shield and K.S. Kim, *Experimental measurement of the near tip strain field in an iron-silicon single crystal,* Journal of the Mechanics and Physics of Solids, 1994, **42**(5): p. 845-873.

36. W.C. Crone and T.W. Shield, *An experimental study of the effect of hardening on plastic deformation at notch tips in metallic single crystals,* Journal of the Mechanics and Physics of Solids, 2003, **51**(8): p. 1623-1647.

37. J.W. Kysar and C.L. Briant, *Crack tip deformation fields in ductile single crystals*, Acta Materialia, 2002, **50**(9): p. 2367-2380.

38. A. Staroselsky and L. Anand, *A constitutive model for hcp materials deforming by slip and twinning application to magnesium alloy AZ31B,* International Journal of Plasticity, 2003, **19**(10): p. 1843-1864.

39. R. Parisot, S. Forest, A. Pineau, F. Grillon, X. Demonet and J.M. Mataigne, *Deformation and damage mechanisms of zinc coatings on hot-dip galvanized steel sheets: Part I. Deformation modes,* Metallurgical and Materials Transactions A, 2004, **35**(3): p. 797-811.

40. V. Gupta, *Tensile crack-tip fields in elastic--ideally plastic hexagonal crystals and layered materials,* Acta Metallurgica et Materialia, 1993, **41**(11): p. 3223-3236.

41. M.D. Hunt, J.A. Spittle and R.W. Smith, *An acid saw for the strain-free cutting of single crystals,* Journal of Scientific Instruments, 1967, **44**(3): p. 230-231.

42. G. Petzow, *Metallographic etching : metallographic and ceramographic methods for revealing microstructure*, 1978, Metals Park, Ohio: American Society for Metals.

43. C.A. Cinnamon and A.B. Martin, *Growth Conditions for Single and Optically Mosaic Crystals of Zinc,* Journal of Applied Physics, 1940, **11**: p. 487-490.

44. L. Anand and M. Kothari, *A computational procedure for rate-independent crystal plasticity,* Journal of the Mechanics and Physics of Solids, 1996, **44**(4): p. 525-558.

45. G.I. Taylor, *Analysis of plastic strain in a cubic crystal,* Stephen Timoshenko Anniversary Volume, Macmillan, New York, 1938: p. 218-224.

46. E.P.T. Tyndall, *Note on the probable values of the elastic constants of the zinc crystal,* Physical Review, 1935, **47**(5): p. 398-399.

47. D.S. Dugdale, *Yielding of steel sheets containing slits,* Journal of the Mechanics and Physics of Solids, 1960, **8**(2): p. 100-104.

48. G.I. Barenblatt, *The mathematical theory of equilibrium cracks in brittle fracture.* Advances in Applied Mechanics, 1962, **7**(2): p. 55-129.

49. A. Needleman, *An analysis of decohesion along an imperfect interface.* International Journal of Fracture, 1990. **42**(1): p. 21-40.

50. R. Parisot, S. Forest, A. Pineau, F. Grillon, X. Demonet and J.M. Mataigne, *Deformation and damage mechanisms of zinc coatings on hot-dip galvanized steel sheets: Part II. Damage modes,* Metallurgical and Materials Transactions A, 2004, **35**(3): p. 813-823.

51. M.F. Ashby, F.J. Blunt and M. Bannister, *Flow characteristics of highly constrained metal wires,* Acta Metallurgica, 1989, **37**(7): p. 1847-1857.

52. B.D. Flinn, M. Ruhle and A.G. Evans, *Toughening in composites of Al_2O_3 reinforced with aluminum,* Acta Metallurgica, 1989, **37**(11): p. 3001-3006.

53. K.J. Shang and R.O. Ritchie, *Crack bridging by uncracked ligaments during fatigue-crack growth in SiC-reinforced aluminum-alloy composites,* Metallurgical Transactions A, 1989, **20**(5): p. 897-908.

54. T. Iung and A. Pineau, *Dynamic crack propagation and crack arrest investigated with A new specimen geometry: Part II: Experimental study on a low-alloy ferritic steel,* Fatigue and Fracture of Engineering Materials and Structures, 1996, **19**(11): p. 1369-1381.

55. R.M. McMeeking and D.M. Parks, *On criteria for J-dominance of crack-tip fields In large-scale yielding,* Elastic-Plastic Fracture-STP 668, 1979.

56. K. Chan, *Micromechanics of shear ligament toughening,* Metallurgical and Materials Transactions A, 1991, **22**(9): p. 2021-2029.

57. P. Mataga, *Deformation of crack-bridging ductile reinforcements in toughened brittle materials,* Acta Metallurgica, 1989, **37**(12): p. 3349-3359.

58. H.H.M. Cleveringa, E. Van der Giessen and A. Needleman, *A discrete dislocation analysis of mode I crack growth,* Journal of the Mechanics and Physics of Solids, 2000, **48**(6-7): p. 1133-1157.

59. S. Forest and G. Cailletaud, *Strain localization in single crystals: bifurcation analysis, effects of boundaries and interfaces,* European Journal of Mechanics. A: Solids, 1995, **14**(5): p. 747-771.

60. S. Forest, P. Boubidi and R. Sievert, *Strain localization patterns at a crack tip in generalized single crystal plasticity.* Scripta Materialia, 2001, **44**(6): p. 953-958.